Hybrid point-of-care devices for visual detection of biomarkers and drugs

---

Ph.D. Program

Science and Technologies of Chemistry and Materials

Curriculum: Drug Discovery & Nanobiotechnologies

XXXV Cycle

University of Genoa

Faculty of Chemistry

Department of Chemistry and Industrial Chemistry

And

Istituto Italiano di Tecnologia

Coordinator
Prof. Renata Riva

Tutors
Dr. Pier Paolo Pompa
Prof. Annalisa Relini

PhD student
Tania Pomili

TABLE OF CONTENTS

ABSTRACT 5

CHAPTER 1 7

Introduction 7

1.1 The importance of preventive care screening and POCT 7

1.2 µPADs 8

1.2.1 Multiplexing analysis 10

1.3 Lateral flow assay 10

1.3.1 Nucleic acid-based LFA 13

1.4 Nanomaterials for sensing application 14

1.4.1 AuNPs-based POCT 17

1.4.2 Nanodiagnostics 18

1.4.3 Biofluids for nanodiagnostics 18

1.4.4 The potential of saliva as a diagnostic fluid 20

1.4.5 Nanoparticles-based POCT for contamination control 22

1.5 Thesis motivation and layout 23

CHAPTER 2 25

Colorimetric nanoplasmonics to spot hyperglicemia from saliva 25

2.1 An overview of diabetes 25

2.2 Glucose sensing for diabetes monitoring 25

2.2.1 µPADs for glucose sensing 26

2.2.2 Saliva as a biological matrix for glucose monitoring 26

2.2.3 Glucose sensing strategies based on AuNPs 27

2.3 Our strategy: colorimetric nanoplasmonics for glucose sensing 31

2.3.1 Reshaping process 31

2.4 Results and discussions 33

2.4.1 Synthesis of multibranched AuNPs 33

2.4.2 Optimization of MGNPs morphology 35

2.4.3 Optimization of the reshaping process 36

2.4.4 Application in saliva 38

2.4.5 Development of a home-testing device prototype 41

2.4.6 Assay validation on real diabetic saliva samples 44

2.5 Materials and methods 45

2.5.1 Chemicals 45

2.5.2 Instrumentation 46

2.5.3 Synthesis of 15 nm AuNPs 46
2.5.4 Characterization of 15 nm AuNPs 46
2.5.5 Synthesis of MGNPs 46
2.5.6 Characterization of MGNPs 47
2.5.7 Optimization of the platform in water 47
Experiments with different pH 47
Experiments with different halogens 47
Experiments of hydrogen peroxide detection 47
Optimized conditions 48
2.5.8 Optimization of the platform in saliva 48
Saliva collection and handling 48
Reshaping in saliva 48
TEM micrographs of the reshaping in saliva 48
2.5.9 Glucose dipstick assay prototype 49
Substrate preparation 49
Glucose assay protocol 49
Assay reliability and validation 49
Assay reproducibly and limit of detection 50
2.6 Conclusions 50
CHAPTER 3 52
Paper-based multiplexed colorimetric device for the simultaneous detection of salivary biomarkers 52
3.1 An overview of POCT 52
3.1.1 Paper-based POCT 53
3.1.2 Microfluidic paper-based POCT 53
3.1.3 CO_2 laser cutting fabrication technique 54
3.2 Multiplexed analysis 54
3.3 Colorimetric paper-based POCT 55
3.4 Our strategy: a multiplexed paper-based device for colorimetric detection of salivary biomarkers 57
3.4.1 Target biomarkers and their metabolic role 57
3.4.2 Detection strategy: reshaping process 58
3.5 Results and discussions 59
3.5.1 Device configuration and working mechanism 59
3.5.2 Assay optimization 63

3.5.3 Analytical performance 66
3.5.4 Multiplexing assay 68
3.5.5 Interference study 69
3.5.6 Development of a device prototype 70
3.6 Materials and methods 71
3.6.1 Chemicals 71
3.6.2 Instrumentation 71
3.6.3 Synthesis of 15 nm AuNPs 71
3.6.4 Characterization of 15 nm AuNPs 71
3.6.5 Synthesis of MGNPs 72
3.6.6 Characterization of MGNPs 72
3.6.7 Design and fabrication of the analytical device 72
3.6.8 Reshaping process 72
3.6.9 Assay procedure 73
3.6.10 Data collection and analysis 73
3.6.11 Saliva samples preparation 73
3.7 Conclusions 74
CHAPTER 4 75
A lateral flow device for point-of-care detection of doxorubicin 75
4.1 An overview of chemotherapy 75
4.2 The importance of drug monitoring in chemotherapy 75
4.3 Healthcare workers’ exposure to chemotherapeutic drugs 76
4.4 Doxorubicin: therapeutic and side effects 76
4.4.1 Doxorubicin: detection strategies 77
4.5 Our strategy: a POC device for on-site detection of doxorubicin contamination 78
4.6 Results and discussions 79
4.6.1 Device design and detection mechanism 79
4.6.2 Optimization of the capture probe 80
4.6.3 Optimization of the flow 84
4.6.4 Analytical performance of the LF device 86
4.7 Materials and methods 90
4.7.1 Chemicals 90
4.7.2 Instrumentation 90
4.7.3 Lateral flow device assembly and electrostatic immobilization of the capture probe 91
4.7.4 Assay procedure and data processing 91

4.7.5 Assay in a real urine sample 92
4.8 Conclusions 92
CHAPTER 5 94
An innovative lateral flow device for methotrexate detection 94
5.1 An overview of methotrexate 94
5.2 Methotrexate detection strategies 95
5.3 Our strategy: a POC device for on-site detection of methotrexate contamination 96
5.4 Preliminary results and discussions 96
5.4.1 Device design and detection mechanism 96
5.4.2 Synthesis of the label molecules 98
5.4.3 Optimization of the conjugate solution 99
5.4.4 Optimization of the capture probe 101
5.4.5 Optimization of the assay performance 103
5.4.6 Analytical performance 104
5.5 Materials and methods 105
5.5.1 Chemicals 105
5.5.2 Instrumentation 106
5.5.3 Synthesis of 35 nm AuNPs 106
5.5.4 Characterization of 35 nm AuNPs 106
5.5.5 Lateral flow device assembly 106
5.5.6 Assay procedure 107
5.6 Conclusions 107
CONCLUSIONS AND OUTLOOKS 109
BIBLIOGRAPHY 113
LIST OF ACRONYMS 125
LIST OF FIGURES 128
LIST OF TABLES 134
Phd PORTFOLIO 134
ACKNOWLEDGEMENTS 136

ABSTRACT

Early diagnostics is a crucial part of clinical practice offering a rapid and convenient way to investigate and quantify the presence of key biomarkers related to specific pathologies and increasing the chance of successful treatments. In this regard, point-of-care testing (POCT) shows several advantages enabling simple and rapid analyses, allowing for real-time results, and permitting home testing. Metallic nanoparticles (NPs), like gold NPs (AuNPs), can be beneficially integrated into POC devices thanks to their tunable plasmonic properties which provide a naked-eye read-out. Moreover, the high sensitivity of NPs enables the detection of biomarkers in non-invasive fluids where the concentrations are typically low. These biofluids, like saliva and urine, are functionally equivalent to serum in reflecting the physiological state of the body, whilst they are easier to handle, collect, and store.

In this thesis, I first reported the design and development of a colorimetric strategy based on the morphological change of multibranched plasmonic AuNPs, aimed at detecting glucose in saliva. The sensing approach relied on a target-induced reshaping process which involves the oxidation of the NP tips and the transformation into a spherical shape, characterized by a naked-eye detectable blue-to-pink color change. The platform proved to be beneficial in the early and non-invasive diagnosis of hyperglycemia. The successful technological transfer on a solid substrate paved the way for the realization of a dipstick prototype for home testing. Then, the strategy was adapted to other biomarkers, leading to the development of a multiplexing test for the simultaneous detection of three salivary analytes (cholesterol, glucose, and lactate). This multiplexing assay enabled to save reagents, costs, and time, whilst increasing the overall clinical value of the test. Exploiting the microfluidics applied on a paper sheet, I realized a monolithic and fully integrated POC device, through a low-cost and fast CO_2 laser cutter. The platform showed excellent selectivity and multiplexing ability, with negligible interferences.

The second part of my thesis was focused on the development of POC devices for the detection of anticancer drug contaminations in water solutions and urine samples. Antiblastic agents have revealed high toxicity for the exposed healthcare workers who prepare and administer these drugs in occupational environments. Hence, continuous monitoring is highly required, and POCT shows tremendous potential in this context. With this aim, I realized a lateral-flow (LF) device for the assessment of doxorubicin contamination, using the fluorescent properties of the drug for naked-eye detection. The pharmacological recognition of the DNA probe was exploited to overcome the lack of anti-doxorubicin antibodies. The highly sensitive strategy was successfully adapted to a real urine sample, without resorting to complex pretreatment procedures. Then, I developed a competitive LF device for the detection of methotrexate (MTX). AuNPs were employed as the label molecules and the pharmacological competition of folic acid and MTX for the capture enzyme was exploited as the recognition mechanism, instead of costly antibodies. Despite the sensitivity

requires further improvements, the strategy showed fast and reliable results, demonstrating a high potential for workers’ safety control.

CHAPTER 1

INTRODUCTION

1.1 The importance of preventive care screening and POCT

Early diagnosis is a valuable strategy for detecting morbidity state and progression at the premature stages; for instance, it is a desirable goal for the healthcare system. Timely and appropriate monitoring of tumors[1], brain disorders[2], and pathological diseases like diabetes[3] allows for improving the chance of successful treatment, avoiding long-term medical care and complications, and saving money. Point-of-care testing (POCT) holds high potential in this scenario, representing a valid alternative to conventional laboratory techniques (fig.1).

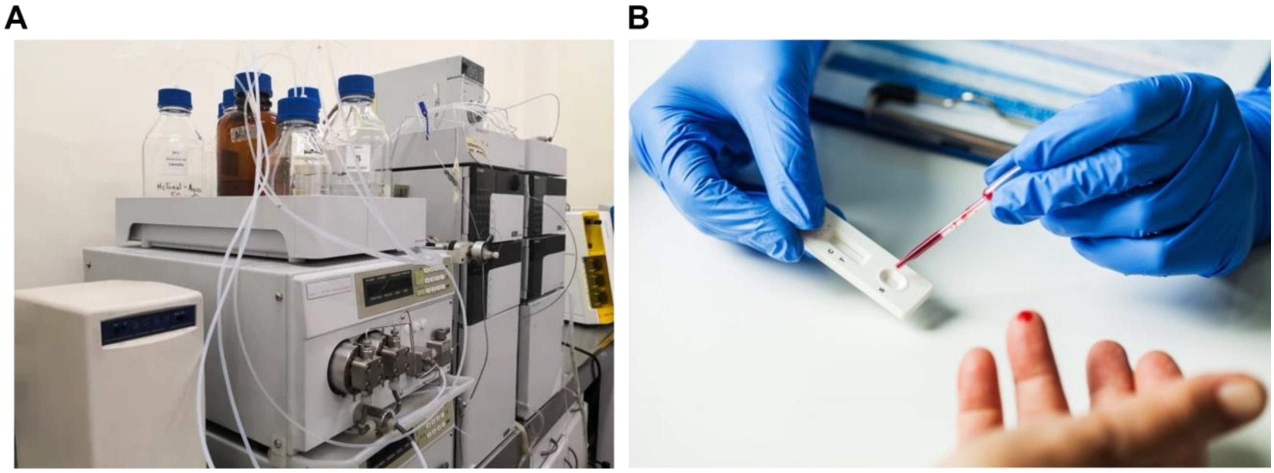

Figure 1. Central laboratory testing (A) is based on instrumental techniques which enable accurate and sensitive analyses but require trained personnel and a long turnaround time; POC devices (B) can be performed by the patient at home, without complicated instrumentation, and provide rapid test results.

Central laboratory techniques, indeed, enable specialized testing with a high-throughput robotic automatization and instrument assay step integration, ensuring high sensitivity and accuracy, particularly when the analysis requires complex methodology. However, they are not suitable when the turnaround time is critical like for the blood gases and electrolytes, or the specimen is not stable during transport for example in the case of extremes of temperature and physical forces[4]. POC devices, on the contrary, provide fast analysis and accurate diagnostics near the patients and ensure robustness, selectivity, and sensitivity in the response. In addition, POC assays can be performed by the patient himself since they do not require trained personnel and specialized equipment and they are beneficial when a rapid turnaround time of test results for clinical decisions is needed[5]. Due to the advantage of being self-administered, POC tests make patients more and more responsible for their condition and increase their compliance.

Home tests enable to reduce the frequency of hospital visits and they offer huge advantages when patients' physical and mental faculties are compromised[6]. The glucose meter, the pregnancy test, and the COVID-19 antigen test are some of the most widely employed POC devices, which have demonstrated enormous advantages for the users, offering continuous monitoring and immediate test results, enabling rapid clinical decisions.

The integration of microfluidics in POC devices is a valid solution for addressing the issues of portability and detection speed. Microfluidics systems, indeed, are small and portable devices that enable precise control and manipulation of the fluid flow, constrained to a very small size (sub-millimeter). Microfluidic platforms combine sample pretreatment, separation, mixing, and detection, enabling to perform the analysis entirely within the small device, avoiding human interference. Hence, microfluidic systems combined with POCTs are among the most appealing portable devices for early diagnosis[7].

Dolomite Microfluidic, in this context, is one of the leading providers of custom microfluidic devices. It develops microfluidic chips, connectors, pumping solutions, and other tools which have been exploited, for example, in the development of finely controlled viscoelastic particle encapsulation, useful in biomedical engineering and materials science[8]. These microfluidics devices produce monodisperse droplets with precise control of flow rate and pressure, virtually eliminating the preparation errors related to the ingredients and size of the droplet and resulting in 0% wastage. They have been also used for the realization of flow rate sensors, providing fast and accurate measurements with high sensitivity. However, these expensive and sophisticated microfluidic components, are not suitable for the disposable and low-cost requirements of POC devices.

Microfluidic platforms have been made from a wide variety of materials (e.g., silicon, glass, polydimethylsiloxane (PDMS), and other polymers). However, due to its simplicity, abundance, biocompatibility, and low cost, paper is widely employed for the realization of microfluidic paper-based devices (µPADs). In paper-based devices, indeed, flow is generated through the capillary forces of wetted cellulose fibers that create capillarity in the material, without requiring external pumps or power supplies, increasing the portability and reducing the costs.

1.2 µPADs

Paper is relatively simple to be manipulated for the creation of hydrophobic boundaries where the flow of the sample can be confined and directed[9]. An important issue related to the fabrication of patterns in µPADs is the imprecise nature of most of the available fabrication methods. Indeed, it is often difficult to produce patterns with dimension smaller than 1 mm. Patterning paper with high resolution enables to fabricate smaller devices with higher channel density which could process smaller volumes of sample in shorter amount of time, making µPADs highly attractive for POC diagnosis. There are several fabrication methods to design patterns in µPADs, including photolithography in which a light-sensitive chemical is deposited on the paper substrate in a specific design and exposed to ultraviolet (UV)-light sources, or oxygen plasma[10]; plotting, which employs a computer-integrated X, Y-plotter for the creation of a microfluidic PDMS pattern onto paper[11]; wax printing which makes use of a solid ink printer to realize the hydrophobic boundaries with wax that is further heated to melt[12]; inkjet printing in which pattern is creating dropping ink droplets on the substrate; and other available techniques like plasma etching, knife-based cutting and flexographic printing[13]. The reported techniques offer huge advantages in the creation of the microfluidic pattern, however, they all suffer from some limitations due, for example, to the high costs of photoresists, the low resolution of the plotting, the additional melting, and ink formulation steps[14]. On the contrary carbon dioxide (CO_2) laser cutting can be a promising alternative allowing for the very rapid creation of hydrophobic boundaries in a single process and with high resolution. CO_2 laser cutting is a simple fabrication technique that involves the design of the desired pattern through computer drawing software and the further transfer of the design to the laser cutting machine where the heat produced by the laser will burn the paper substrate, creating the hydrophobic pattern. This technique provides excellent fabrication reproducibility, rapidity (7-20 seconds for the device), scalability to bulk production, and low costs since it only requires a sheet of paper. For the optimization of the experimental conditions, applied current and cutting rates must be finely tuned since they play a crucial role in creating the pattern[15]. A schematic illustration of the operation principle of the CO_2 laser cutting method and the flow of a red ink confined inside the hydrophobic boundaries is illustrated in fig.2.

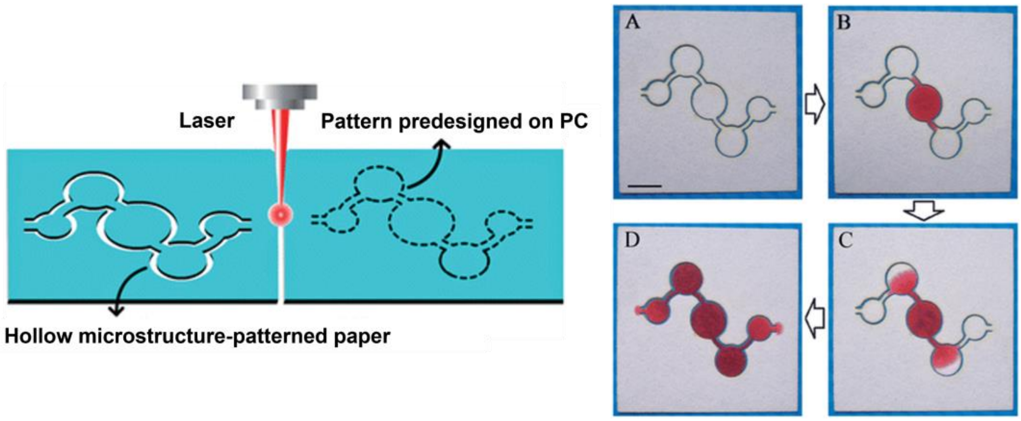
Laser
Pattern predesigned on PC
Hollow microstructure-patterned paper
A
B
D
C

Figure 2. Operation principle of a CO_2 laser cutting technique and flow of red ink inside the hydrophobic boundaries[15].

1.2.1 Multiplexing analysis

The ability of microfluidics to direct flow in a controlled manner combined with the versatility of the CO_2 laser cutter technique in creating complex patterns allows to fabricate μPADs with multiplexing ability, enabling the detection of multiple targets simultaneously. Unlike traditional paper-based POC devices, specifically designed for a single target, multiplexed microfluidic POC assays present the unique capability to split a single, low-volume sample into separate parts of the device, enabling to analyze different markers in parallel. For instance, each reaction can be optimized independently, avoiding issues related to the cross-reactivity between assays. Performing multiplexed analyses with a very small sample volume enables saving reagents, time, and costs, showing huge benefits in less-industrialized countries and as a valid alternative to expensive advanced techniques already used in clinical settings. Furthermore, the identification of different parallel biomarkers, or specific combinations of them, remarkably improves the clinical value of the test, facilitating clinical management[16]. Fig.3 illustrates an interesting example of μPADs for the multiple colorimetric detections of glucose, uric acid, lactate, and choline which are clinically important biomarkers in regulating metabolic processes and, hence, the simultaneous detection provides important information for early diagnosis of pathological conditions[17].

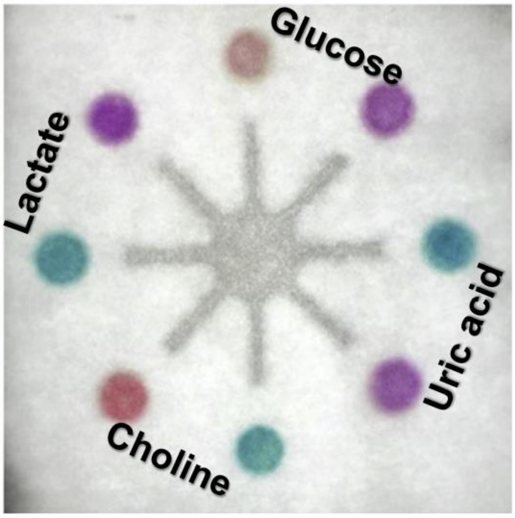

Figure 3. Photograph of the μPADs for the multiplexed detection of biomolecules[17].

1.3 Lateral flow assay

The most extensively used form of paper-based POC is the lateral flow assay (LFA). LF devices have all the reagents pre-stored in the strip and they integrate the flow of the sample that passes through the separate zones loaded with different reagents[18]. The first LFA appeared in the 1970s[19] and for its simplicity and low cost, it has been largely employed in several fields such as diagnostics[20], environmental monitoring[21], and food contaminants[22]. In LFAs, the sample is deposited onto the lateral-flow test strip and the qualitative/or semi-quantitative outcome is revealed by the appearance of a line. A schematic illustration of the main components of an LF device is depicted in fig.4.

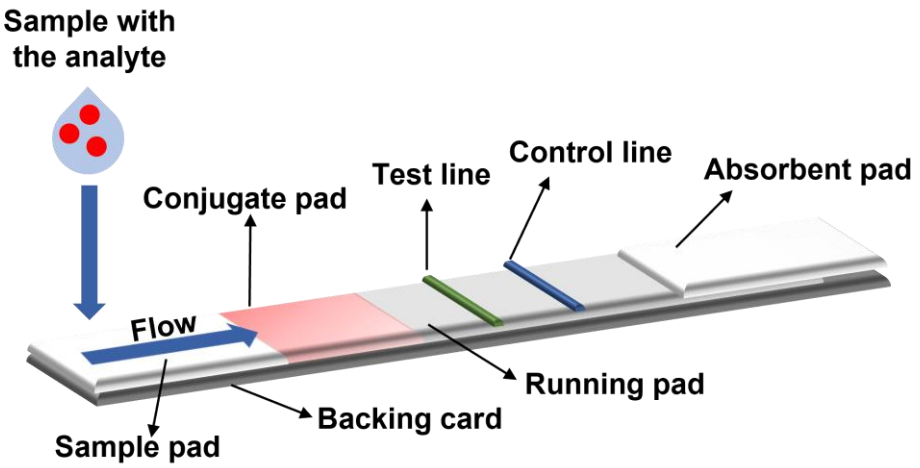

Figure 4. Schematic illustration of the main components of an LF device.

Entering more in detail, an LF device is mainly composed of four different pads that are laminated on a backing card and partially overlapped. The sample pad is at the beginning of the lateral-flow test strip, and it is used to load the sample. It is conventionally made of cellulose fibers or woven meshes and it must ensure an even flow, retaining a minimal amount of sample. A conjugate pad, generally made of glass fibers, is functionalized with the so-called "detection bioreceptor" conjugated with labels, which are mostly represented by nanoparticles (NPs). This pad should preserve the dried conjugate NPs for detection, enabling the release when the sample passes. The running pad is the part where the detection signal is generated. It can be chosen based on the capillary flow time which is the index of the sample running. The most used substrate is nitrocellulose. The last pad is the absorbent pad, which ensures that all the components reach the end of the strip. For instance, it must have a high wicking capacity and, generally, it is composed of a blend of cotton and grass fibers. The running pad binds the "capture bioreceptors" that form the control and test lines (t-line). The sample, after the deposition, starts flowing through the strip thanks to the capillary force. It first encounters the sample pad, preloaded with buffers, detergents, and blocking agents which corrects sample composition, ensuring the appropriate pH, viscosity, and ionic strength that are required for optimal detection. Next, the sample reaches the conjugate pad where the first analyte-bioreceptor interaction occurs. Then, it flows through the running pad passing across the test and control lines. The assay ends when the sample reaches the absorbent pad.

There are two main types of LFAs which are illustrated in fig.5.

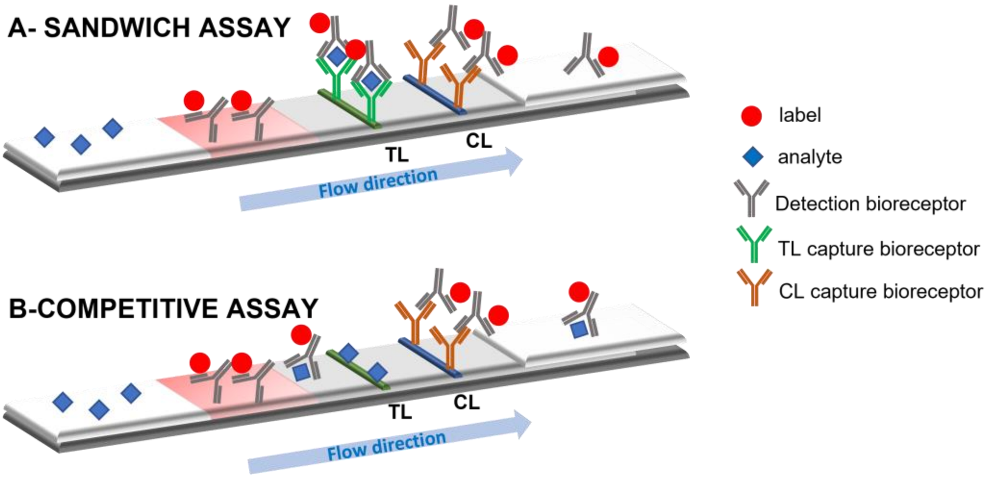

Figure 5. Comparison of the two main types of LFAs.

The conventional sandwich assay (fig.5A) is the most used strategy for the detection of mid and big-size target molecules. The t-line capture bioreceptor traps the analyte bonded with the detection bioreceptor creating a sandwich. The two bioreceptors must bind a different portion of the analyte. The signal achieved is proportional to the amount of targets in the sample. On the other hand, competitive assay (fig.5B) relies on competition between the analyte and capture bioreceptor for the same detection bioreceptor (alternatively, the competition is between the analyte and a labeled molecule in the conjugate pad for the same test line capture bioreceptor). Hence, by increasing the amount of the target, the achieved signal becomes less intense since the binding of the label to the t-line is hampered. This strategy is commonly employed for small analytes that cannot be recognized by more than one bioreceptor simultaneously.

In both cases, the control line is made by a capture bioreceptor that selectively binds the labeled bioreceptor, ensuring the correct operation of the LFA[23].

The flow rate largely affects the biorecognition time since it regulates the dissolution and mixing of immunoreagents and the efficiency of the immunoreactions. Different assays need different reaction time depending on their specific binding kinetics. Capillary flow rate can be modulated by using hallow channels, designing 2D paper networks, using dissolvable sugars and bridges, or taping the surface of lateral flow test substrates [24].

Regarding the detection, the optical readout is the most extensively used since it enables a naked-eye signal which provides huge benefits for qualitative applications, not requiring external readers. A popular label is latex which can be loaded with a variety of probes from colored or fluorescent dyes to magnetic particles. However, gold NPs (AuNPs) are the most extensively used due to their high extinction coefficients and thus intense colors[25].

The choice of the bioreceptor is the most important step in the development of an LFA. The sample passes through the t-line in a matter of seconds, hence, a weak binding between the target and the bioreceptor leads to a blurred signal, which decreases as the concentration of the target reduces. Among the bioreceptors, antibodies are the most widely used thanks to their highly specific binding to analytes, ensuring fast association kinetics. Most of the commercial antibodies are generally characterized by ELISA or western blot, which require long incubation steps, making them unsuitable for the development of an LFA. Furthermore, antibodies may not be available and are sometimes difficult to obtain with the required specificity or affinity for the antigen. Moreover, they suffer from high manufacturing costs and limited stability. This has led to the introduction of alternative bioreceptors such as different proteins and nucleic acids[26].

1.3.1 Nucleic acid-based LFA

In recent years, there is an emerging interest in nucleic acid-based LFAs (NALFAs). Nucleic acids present several advantages over antibodies such as the ability to recognize any type of target analyte, longer stability and shelf lives, a wider range of modifications through chemical synthesis, higher batch-to-batch reproducibility, and a lower cost. A further advantage of NALFAs over antibodies-based LFAs is the possibility to recognize specific deoxyribonucleic acid (DNA) or ribonucleic acid (RNA) sequences. The realization of a NALFA implies that DNA molecules are immobilized on the nitrocellulose running pad. Most of the reported immobilization methods rely on a covalent bonding between biotin-modified DNA molecules and streptavidin, which requires a previous step of incubation for the formation of the complex and a further purification procedure for removing the excess of streptavidin, complicating the overall preparation, and increasing the cost of the LFA[27]. In this context, the direct immobilization of the captured DNA, without resorting to UV-crosslinkers or heating devices that could damage DNA molecules[28], is strongly desired. As illustrated in fig.6, Park et al. reported an alternative strategy of salt-mediated immobilization of nucleic acids onto nitrocellulose membrane based on a pre-treatment of DNA with potassium chloride (KCl). KCl should neutralize the negatively charged capture DNA and reduce the intermolecular electrostatic repulsion of the molecule with the membrane (which has a general negative electric charge), increasing the immobilization efficiency[29].

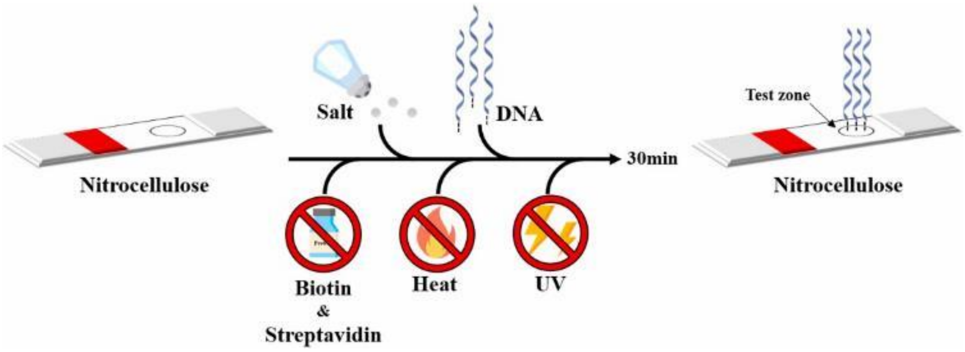

Figure 6. Schematic illustration of salt-mediated immobilization of nucleic acids onto nitrocellulose membrane[29].

Despite the great efforts that have been made in the development of NALFAs, the reported techniques are designed with aptamers (short sequence of artificial DNA or RNA) or single-strand DNAs as sensing probes and they are commonly used for hybridization-based platforms, where the detection is performed by the complementary recognition of two nucleotide strands[30,31].

1.4 Nanomaterials for sensing application

Concerning the generation of the detection signal both in µPAD and LF devices, NPs hold enormous potential in the development of highly sensitive and instrument-free POC systems[32].

NPs belong to the family of nanomaterials which are defined as particulate materials with at least one dimension in the range of 1-100 nm (see fig.7).

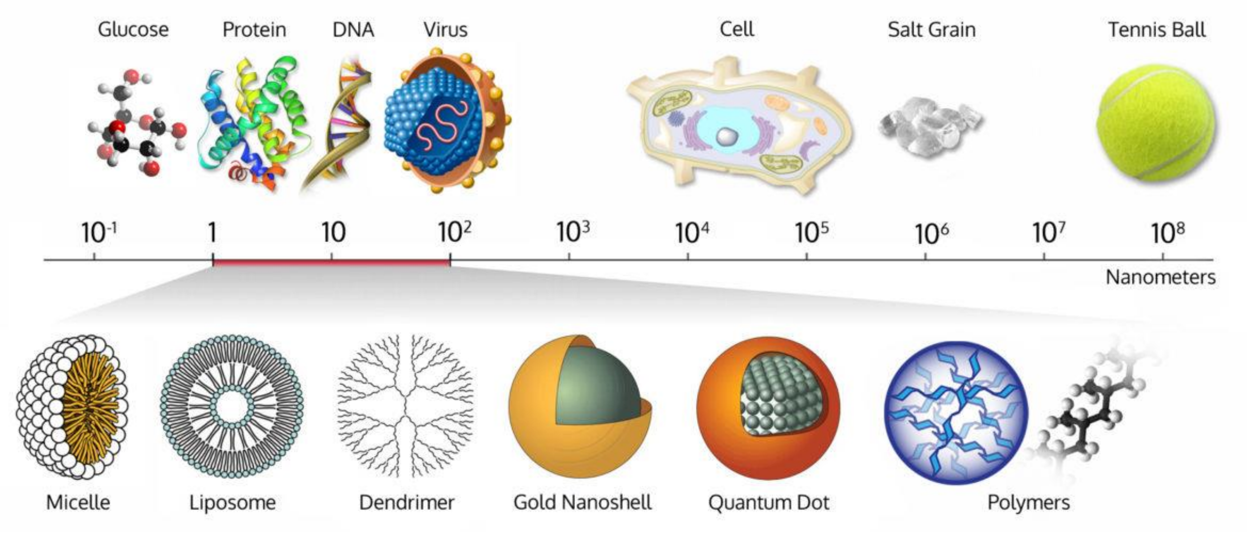

Figure 7. Nanomaterials size.

Nanochemistry deals with the manipulation of chemical processes for synthesizing nanomaterials with unique physical and chemical properties. Due to their size, indeed, nanomaterials are characterized by new properties which escape either the general laws of bulk materials or the quantum mechanics of atoms and molecules. These interesting properties are mainly due to two size-dependent effects: surface effects and quantum confinement effects. Lowering nanomaterial size leads to a remarkable increase in its surface and, consequently, the surface atoms enormously rise compared to the bulk material. Since surface atoms have a lower coordination number, they are less stable than the interior atoms and thus they present increased reactivity, leading to a high surface energy of the nanomaterial. This property can be exploitable to facilitate nanomaterial functionalization or improve catalytic activity[33].

The quantum confinement effect refers to the fact that in nanomaterials the band gap is increased, and the energy levels are discrete unlike the bulk materials characterized by continuum states. For instance, electrons are confined and can move only at definite levels[33].

These two properties lead to unexpected events when nanomaterials interact with light. Nanomaterials, mainly those composed of noble metals such as gold (Au) or silver (Ag), are characterized by remarkable plasmonic properties. Indeed, they exhibit a strong localized surface plasmon resonance (LSPR) which arises when the conduction-band electrons start coherently oscillating with the external frequency of incident light photons. The LSPR absorption peak is typically localized in visible or near-infrared (NIR) spectra for Au or Ag nanomaterials and it is strongly related to their morphology. As illustrated in fig.8, AuNPs with different shapes and sizes present unique optical properties that could be exploited in various applications such as imaging and photothermal therapy[34].

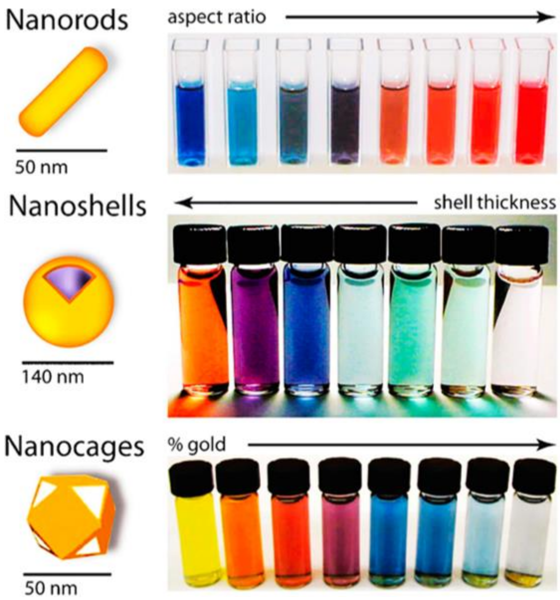

Figure 8. Size and shape-associated colors of three different Au nanomaterials.

The colorimetric biosensing achieved with plasmonic nanomaterials has been reaching great interest since it enables the transformation of the signal into a naked-eye color read-out, without requiring sophisticated instrumentations whilst gaining in cost and simplicity. These absorption and scattering properties can be tuned by controlling particle size, shape, inter-particle distance, and the environment surrounding. Several sensing strategies have been developed aiming to manipulate NPs optical features and they could be divided into aggregation and non-aggregation strategies (see fig.9). The first approach is based on the NPs aggregation and plasmonic coupling, while the second includes the growth or etching of metal NPs[35].

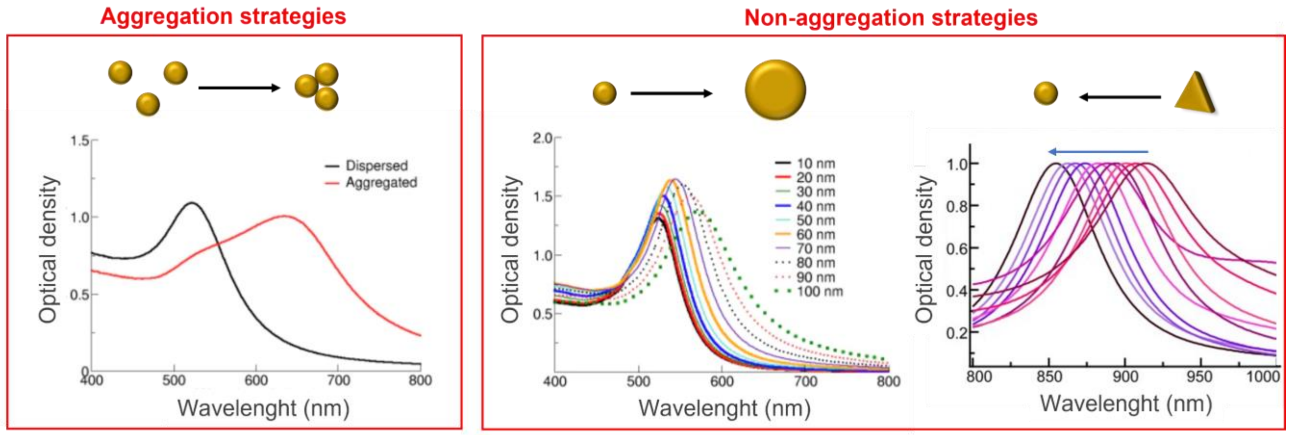

Figure 9. Plasmonic colorimetric detection strategies.

Among these strategies, non-aggregation approaches have attracted increasing interest in the development of plasmonic colorimetric sensors because of their high sensitivity and multi-color changes. Furthermore, they present several advantages over aggregation strategies. First, the NPs used are generally label-free, so it does not require complex procedures for incorporating the recognition reagents on the NPs surface. Second, the auto-aggregation of NPs is avoided and, hence, false positive results and high background signals are excluded. Finally, non-aggregation-based sensors can be made into practical test strips just immobilizing NPs on the desired substrate, improving the detection ability and reproducibility[36]. Etching approaches are generally preferred when the analyses are performed in complex media since proteins of the biological media can be absorbed onto the NPs surface and can influence their growth, acting as shape-directing agents[37]. Etching strategies refer to the oxidation by etchant oxidizes of the atoms constituting the NPs which are converted into water-soluble ions, leading to changes in the aspect ratio (ratio between the width and the height), shape, and LSPR. In this regard, Au nanorods (AuNRs) have been widely employed for etching-based colorimetric sensors thanks to their plasmonic properties dependent on their aspect ratio. The etching of a nanorod and the consequent shortening of the longitudinal dimension, where atoms present a smaller density of passivating ligands and higher surface energy/reactivity, leads to remarkable plasmonic variations and distinct color changes[38].

Methods of oxidative etching are divided into four groups: complex-promoted etching, based on the formation of a complex between metal atoms and compounds like thiourea and cyanide; intermediate-mediated etching mediated by the production of oxidants from the original compounds that are added to the medium; inhibitor-mediated etching in which reagents inhibit NPs etching competing with the oxidants or covering active sites of the NP; and direct etching[39]. The last approach occurs thanks to species that have higher redox potential compared to Au^{+1}/Au^{0} and facilitate the etching of the NP. An interesting colorimetric sensor based on this approach has been developed by Liu et al. and it relies on the color change in presence of glucose in complex media as a result of AuNRs etching by H_2O_2[38]. The direct approach is highly sensitive and suitable for in situ detection since it does not require complicated optical instrumentation. However, it needs strict temperature and pH control, and it suffers from a decrease in the signal intensity which naturally occurs because the NP becomes smaller after the oxidation[39].

1.4.1 AuNPs-based POCT

NPs offers the possibility to realize portable, easy-to-use, and inexpensive sensor due to the miniaturization of the components. The large surface-to-volume ratio enables to maximize the binding with the target, allowing for the detection of trace concentrations of analytes, using a minimal amount of sample volume. Moreover, as mentioned before, the integration of NPs in POC devices offers several advantages in the generation of a naked-eye signal thanks to the unique properties of nanomaterials. Plasmonic nanoparticles, AuNPs particularly, are largely preferred over common colorimetric dyes as tools for the realization of naked-eye POCT since the molar extinction is usually up to five orders of magnitude higher than the brightest molecular chromogens, inducing a visible color at low nM and even pM concentrations[40] and they are characterized by remarkable and tunable plasmonic properties[41].

A microfluidic µPAD for the detection of Hg (II) as an environmental pollutant in the air, water, and fish, has been developed exploiting AuNPs aggregation-based approach (see fig.14). Specifically, NPs have been functionalized with N'-bis(2-hydroxyethyl) dithiooxamide which has created a strong Au-S bond with the NPs by a soft-soft acid-base interaction. When Hg has added, a cross-linking mechanism with the metal has occurred, leading to changes in the surface plasmon band of AuNPs and a visible color shift from red to blue. The proposed µPAD has been tested for the detection of mercury ions in real samples achieving a limit of detection (LoD) of 3 ppb[42].

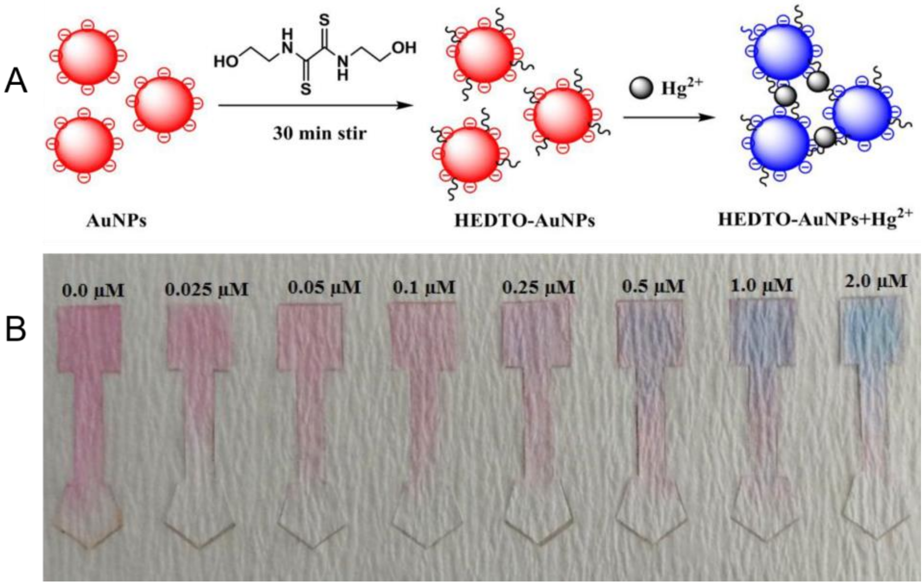

Figure 10. A) Schematic illustration of the aggregation-based mechanism for the detection of mercury; B) Photograph of the proposed µPADs tested with increasing Hg (II) concentrations [42].

It is worth mentioning that the most commonly used labels in LF devices (LFD) are AuNPs thanks to their ability to generate a direct signal, their easy functionalization and low toxicity, and their high affinity toward biomolecules[43]. A striking example is represented by the LFD for SARS-CoV-2, which is considered a timely complementary approach for molecular assays. The strip is composed of immobilized SARS-CoV-2 nucleocapsid protein in the test zone and a conjugate made of anti-human immunoglobulin G (IgG) with 30 nm colloidal AuNPs. A sample containing IgG antibody of SARS-CoV-2, firstly complexes with the conjugate and then, flowing through the membrane and passing across the test zone, binds SARS-CoV-2 nucleocapsid protein, showing a red signal as a result of AuNPs captured in the test line[44].

Furthermore, the widespread diffusion of smartphones and the recent development of smartphone applications for image reading enables the automated evaluation of the developed color, allowing also for quantitative analyses[45].

1.4.2 Nanodiagnostics

The remarkable plasmonic features, the striking catalytic properties, and the high surface-to-volume ratio which improve the surface reactivity to functionalization and enhance the loading with receptors have made NPs attractive tools for nanodiagnostics applications[46].

Nanodiagnostics is the application of nanotechnology in molecular diagnosis and relies on the detection of disease biomarkers, pre-cancerous cells, viruses, relevant proteins, and antibodies or other prognostic molecules which indicate a disease, enabling the early detection of pathological conditions. Nowadays, several efforts have been made to apply nanodiagnostics in the field of cancer therapy; however, it has been further extended to other conditions such as diabetes, and infectious and cardiovascular diseases[47]. Nanomaterials have attracted increasing interest for imaging applications where inorganic NPs like quantum dots and AuNPs are largely exploited due to their plasmonic properties, in magnetic resonance imaging using the intrinsic superparamagnetism of iron oxide NPs[48], and in the realization of POC devices.

1.4.3 Biofluids for nanodiagnostics

The large surface area and the peculiar physicochemical properties of NPs enable nanodiagnostics to detect biomarkers in different biofluids. A biomarker is an analyte contained in a biological matrix that gives information about the patient’s health state. Indeed, a biomarker may provide a diagnosis or assess the severity of the disease[49]. There is no doubt that blood represents the most investigated biomarkers source and the most employed biofluid for nanodiagnostics. However, saliva, urine, tears, sweat, and interstitial fluids are emerging as novel and promising matrices. Indeed, they contain a multitude of constituents (including proteins and metabolites) that reflects biological functions[50]. For example, glucose is one of the most relevant and extensively measured biomarkers since it is a predictor of diabetes mellitus, a widespread metabolic disease characterized by elevated levels of blood glucose. The self-monitoring of glucose is performed through an electrochemical measurement which requires an invasive sampling (venipuncture/finger-prick), causing discomfort for frequent monitoring. However, as is shown in fig.11, glucose is present in other biofluids which, on the contrary, are alternative and non-invasive sources. These fluids present several advantages since they do not require needle sampling, avoiding discomfort and anxiety, the assay can be performed by the patients at home with no need for trained personnel, and the risks associated with bloodborne pathogens are strongly reduced[51].

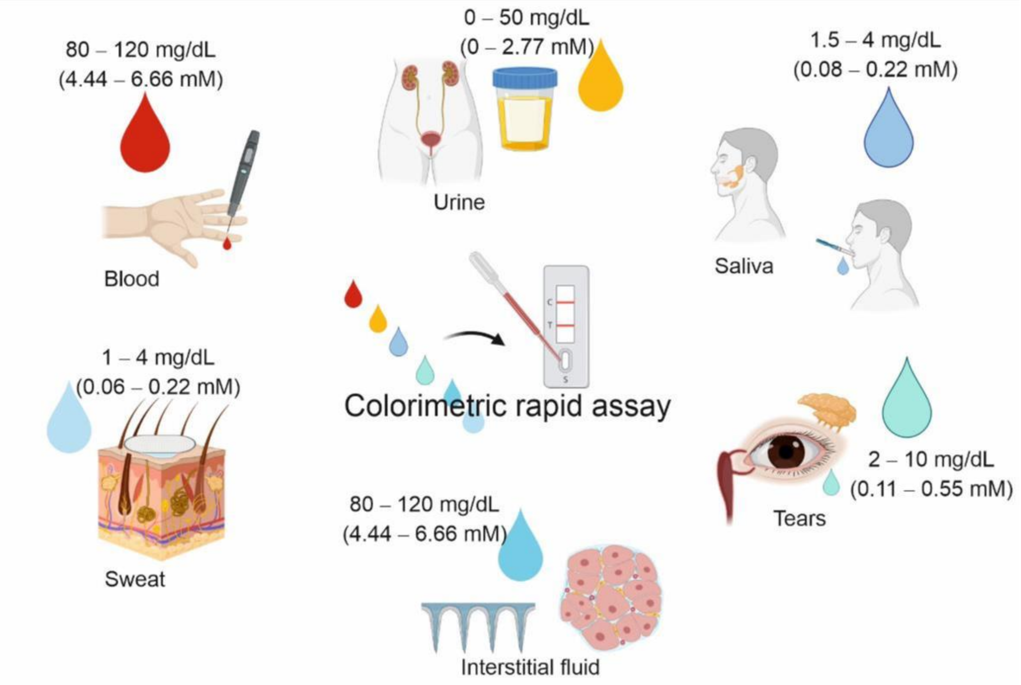
80 – 120 mg/dL
(4.44 – 6.66 mM)
Blood
0 – 50 mg/dL
(0 – 2.77 mM)
Urine
1.5 – 4 mg/dL
(0.08 – 0.22 mM)
Saliva
C
T
S
Colorimetric rapid assay
1 – 4 mg/dL
(0.06 – 0.22 mM)
Sweat
2 – 10 mg/dL
(0.11 – 0.55 mM)
Tears
80 – 120 mg/dL
(4.44 – 6.66 mM)
Interstitial fluid

Figure 11. Different glucose bioresources and related physiological concentrations[51].

Some of the non-invasive fluids such as urine and saliva present the further advantage of being simple to collect and the volume that can be obtained is significantly higher than blood. However, as it is shown in fig.11, the concentration of glucose and other prognostic biomarkers is, in some cases, almost two orders of magnitude lower than in blood, requiring innovative methods for the detection. In this regard, NPs offer several advantages for highly sensitive and naked-eye detection of biomarkers in non-invasive fluids[35].

For example, Au nanobipyramids etching strategy has been developed for the detection of glucose in urine. The mechanism illustrated in fig.12, is based on the oxidation of glucose mediated by glucose oxidase (GOx) which generates hydrogen peroxide (H_2O_2) that can oxidize iodide atoms creating potent etching agents. Etchants start to corrode Au atoms in the sharp edges of the bypyramids leading to a wide spectral shift[52].

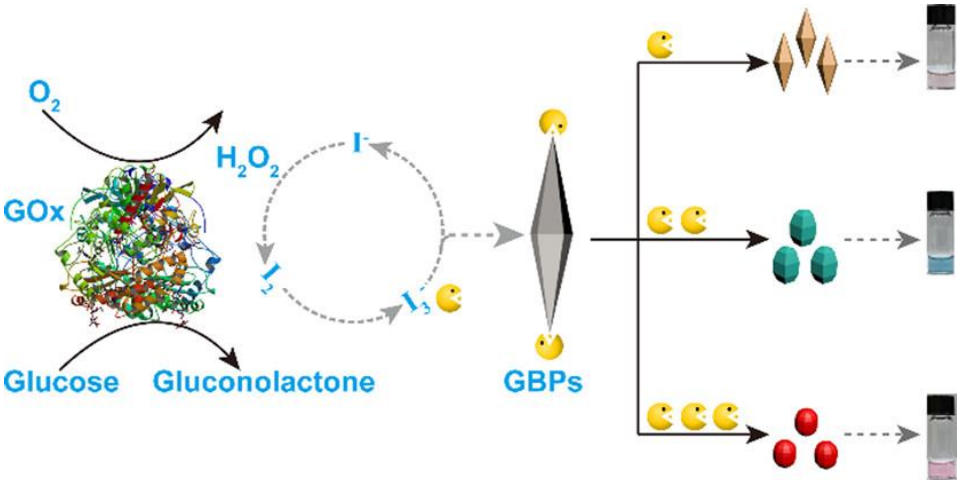

Figure 12. Schematic illustration of the etching mechanism involved in the detection of glucose in urine[52].

1.4.4 The potential of saliva as a diagnostic fluid

Among non-invasive fluids, saliva is emerging as a promising and prognostic diagnostic fluid (fig.13). It is composed of water (98%), mucopolysaccharides and glycoproteins, electrolytes, white blood cells, epithelial cells, and enzymes. It is mainly secreted by parotid and submandibular glands and its daily production ranges from 0.5 to 1.5 liters[53]. It is non-invasively collected and it is readily available both stimulated and non-stimulated; however, in many cases, only in non-stimulated samples the concentration of biomarkers is strictly correlated with the hematic concentrations[54]. Mechanical stimulation, indeed, increases the salivary flow rate and decreases the glucose level. It was found that the glucose content in unstimulated saliva is the most correlated with the blood level[55]. Furthermore, saliva is colorless, and this is a great advantage for the development of colorimetric tests.

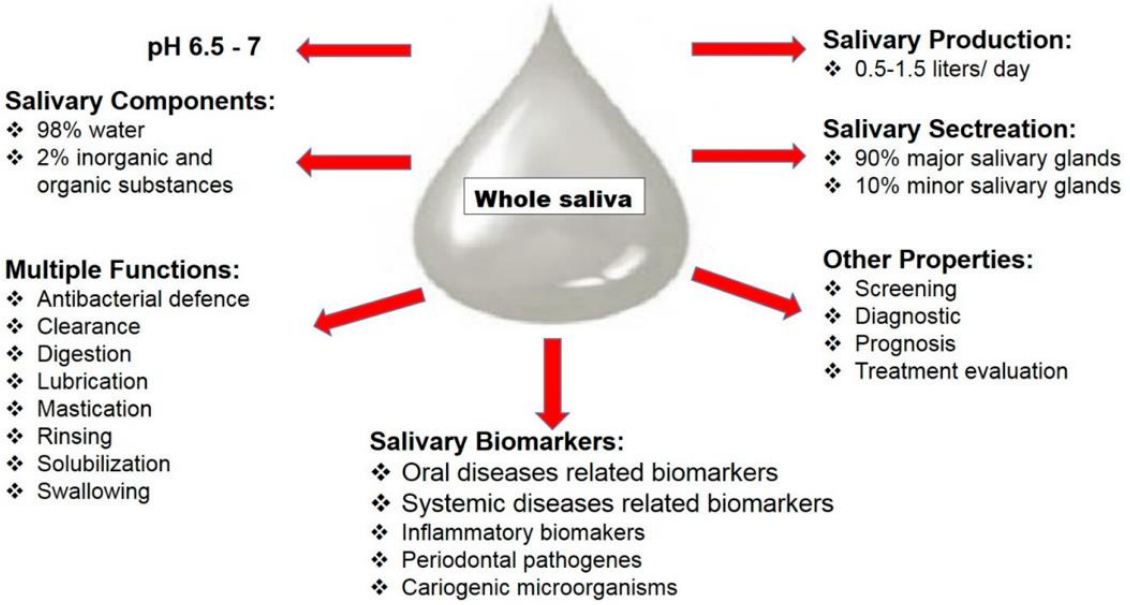
pH 6.5 - 7
Salivary Components:
98% water
2% inorganic and organic substances
Multiple Functions:
Antibacterial defence
Clearance
Digestion
Lubrication
Mastication
Rinsing
Solubilization
Swallowing
Whole saliva
Salivary Production:
0.5-1.5 liters/ day
Salivary Sectreation:
90% major salivary glands
10% minor salivary glands
Other Properties:
Screening
Diagnostic
Prognosis
Treatment evaluation
Salivary Biomarkers:
Oral diseases related biomarkers
Systemic diseases related biomarkers
Inflammatory biomakers
Periodontal pathogenes
Cariogenic microorganisms

Figure 13. Saliva compositions and properties[56].

Saliva is composed of several inorganic compounds such as Na^+, K^+, Ca^{2+}, NH_3, and phosphate; organic compounds like uric acid, glucose, cholesterol, and lactate; proteins and polypeptide compounds like α-amylase, albumin, and mucin; hormones like estrogens cortisol, and progesterone[57]. Saliva is largely employed as a biofluid for the screening of oral diseases where inflammatory biomarkers like interleukins, tumor necrosis factor, and lysozymes can be detected. However, it has been also investigated in cancer therapy, myocardial infarction, and diabetes screening[56,58].

A target-mediated growth of AuNPs functionalized with aptamers has been developed by Soh et al. for the detection of salivary 17β-estradiol for clinical screening using the naked-eye. A schematic illustration of the working mechanism is illustrated in fig.14. Aptamer strands on the NPs surface, selectively bind the target analyte, hence, they can be desorbed as a function of estradiol concentration. Increasing the concentration of the hormone, fewer aptamers will cover the spherical AuNPs and, when the synthesis reagents are added to the solution, AuNP grows into a bigger, spherical shape. On the contrary, with a lower concentration of the target and a higher aptamers amount on the NPs surface, AuNP growth is directed into a branched shape, leading to a visible blue-color change[59].

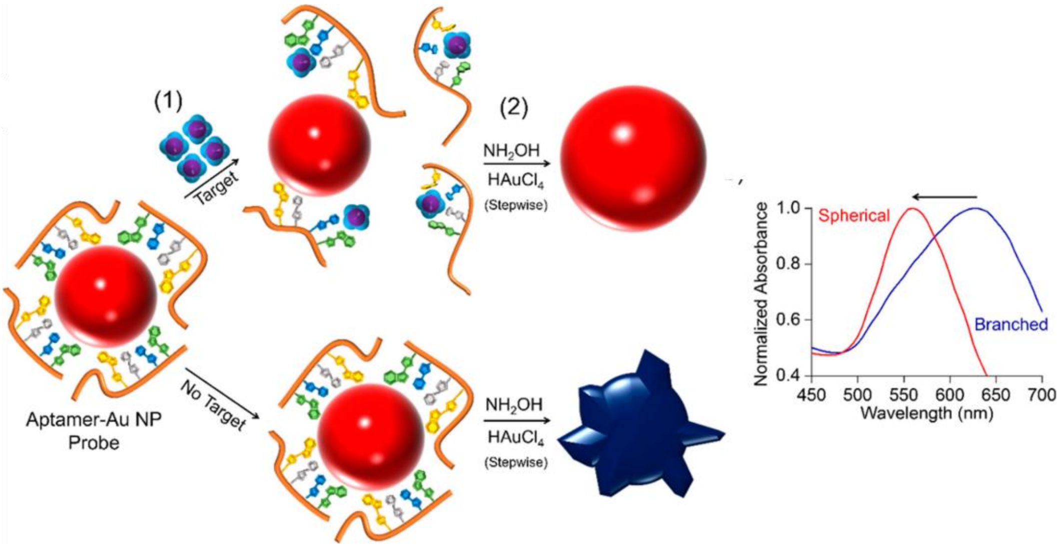

Figure 14. Schematic illustration of salivary 17β-estradiol detection[59].

1.4.5 Nanoparticles-based POCT for contamination control

Anticancer drugs are among the most extensively used agents in the treatment of tumors; however, they present many side effects such as bone marrow suppression, nausea, and hair loss due to the lack of selectivity between tumor and healthy cells. For instance, there is an increasing need for analytical methods to determine these drugs aiming to improve the clinical success of the therapy and reduce the side effects on patients. Moreover, the exposure of healthcare workers in the occupational environments where the drug is administered is emerging as a serious concern. Indeed, trace amounts of cytotoxic drugs have been found in the urine samples of professionals and several studies have demonstrated that occupational exposure is associated with potential cancer risk; hence, sensitive and selective methods for the detection of environmental contamination as well as the presence of the drug in urine samples are highly required[60]. Analyses of cytotoxic agents on contaminated surfaces are commonly performed by collecting the sample through standard protocols such as the wipe sampling approach followed by reference analytical techniques like voltammetry, high-performance liquid chromatography (HPLC), and spectroscopic methods[61]. These laboratory-based techniques present a very low limit of detection and high accuracy, however, the development of POC devices offers several advantages such as rapidity, low cost, and on-site detection which represents a technological advancement for routinely monitoring worker’s safety.

In this context, an LFD for the detection of 5-fluorouracil has been developed by Smith et al.[62]. The illustration of the device performance is provided in fig.15. After wiping contaminated surfaces, the drug is extracted with a proper buffer and applied to the LFD. The principle of operation is a competition between the target and 5-fluorouracil-bovine serum albumin immobilized in the test line. If the drug is present in the sample, it binds the conjugate made of AuNPs and 5-fluorouracil antibody, leaving fewer antibody binding sites for the capture probe in the test line, resulting in a dimmer signal. The proposed device provides a visual read-out of drug contamination in less than 15 minutes and achieves a sensitivity down to 0.25 ng/cm^2 with a simple and handy tool, proving to be comparable and even superior to other laboratory-based techniques in monitoring environmental drug contamination.

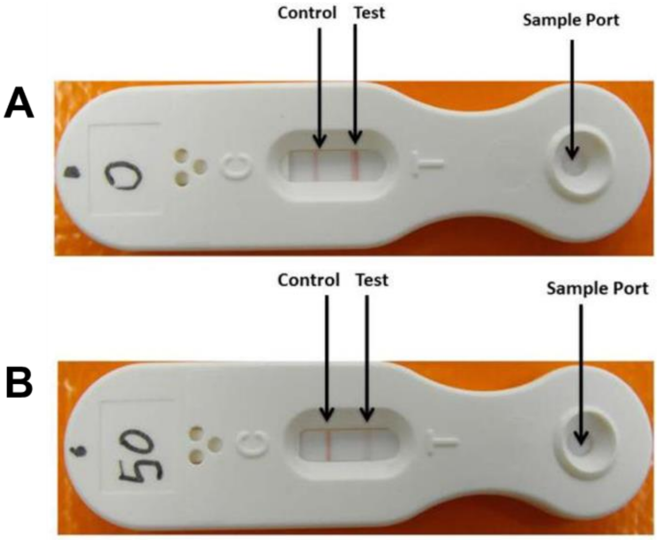

Figure 15. Images of the LFD developed for 5-fluorouracil detection tested without the drug (A) and with 50 ng/cm^2 (B)[62].

1.5 Thesis motivation and layout

As above described, POCT has become of utmost importance in the field of diagnostics, especially for the early detection of prognostic biomarkers and for the on-site monitoring of toxic drug contamination. Although in the field of diagnostics, microfluidic devices and electrochemical sensors are already largely employed, there is an increasing need to lower their costs, develop user-friendly tools, and reduce the physical discomfort associated with invasive sampling. Likewise, there is an urgent demand to routinely monitor environmental contamination in healthcare workers' occupational places, in order to reduce toxic exposure and cancer risk. This work aims to develop tools and methodologies, based on sensitive and plasmonic AuNPs, for the detection of anticancer drugs and salivary biomarkers. In particular, the focus is on the realization of NPs-based paper devices, in the configuration of µPADs and LFDs, which enable a fast and naked-eye read-out. The proposed POC sensors contribute to the early diagnosis of pathologies and the monitoring of antiblastic contamination through user friendly and timely procedures. Using non-invasive fluids improves the patient compliance, increasing the chance of successful treatment. The novelty of the developed µPADs lies in the universality of the approach, making them versatile and easily adaptable to different targets. Likewise, the proposed LFDs for anticancer drugs detection introduce innovative strategies to address the lack of specific recognition antibodies for the target molecules.

Chapter 2 describes the development of a colorimetric strategy based on the target-induced morphological change of plasmonic AuNPs for the detection of salivary glucose. To this purpose, I present the synthesis of multibranched AuNPs, through a seed-mediated approach and the optimization of the chemical process responsible for the color change in the case of the pathological target concentration. In addition, this chapter shows the performance of the assay in the salivary medium and the further technological transfer on a solid support for the realization of a dipstick prototype.

Chapter 3 is a natural evolution of chapter 2, in which I present the development of a monolithic and fully integrated µPADs to simultaneously detect three salivary biomarkers, namely glucose, cholesterol, and lactate. The design of a microfluidic pattern on a paper sheet enables to split the sample into three independent branches where the sensing strategy, based on the previously described AuNPs reshaping, is optimized for each assay. This chapter ends with the realization of a mask for the paper-based device, aiming to develop a home-testing POC sensor.

Chapter 4 describes the design of a novel LFD for the assessment of surface and urine contamination by doxorubicin. The proposed system uses the intrinsic fluorescence of the molecule for naked-eye detection and a novel recognition mechanism based on the pharmacological intercalation of the doxorubicin in the double-strand DNA (dsDNA), used as the capture probe. By exploiting this interaction, the selectivity of the process is boosted, and it enables to enormously reduce the costs of the antibodies and to overcome the lack of availability. As discussed above, several challenges need to be faced when designing a successful NALFA without resorting to covalent bonds or complex procedures. Herein, this chapter describes a promising strategy to solve this issue.

Chapter 5, in conclusion, refers to ongoing work, that aims to develop an LFD for the detection of MTX. The sensing strategy replaces costly antibodies with the pharmacological target of the drug, namely dihydrofolate reductase (DHFR), exploiting the competitive binding of MTX and its biological analog (folic acid) for the same enzyme. The signal read-out is provided by 35nm AuNPs, whose synthesis and characterization are described in this chapter. Although further experiments must be performed to lower the sensitivity, the proposed method is innovative and the achieved visual LoD is encouraging.

CHAPTER 2

COLORIMETRIC NANOPLASMONICS TO SPOT HYPERGLICEMIA FROM SALIVA

2.1 An overview of diabetes

Diabetes is a chronic disease caused by uncontrolled blood glucose levels due to pancreatic insulin dysregulation or its ineffective use by the body. Diabetes can damage organs like the heart, blood vessels, and eyes, increases the risk of strokes, foot ulcers, and retinopathy, and leads to more probability of therapy failure during the treatment of severe diseases like COVID-19. Following global statistics, in 2019, diabetes was the direct cause of 1.5% million deaths and the number is still growing. Diabetes can be distinguished into Type 1, characterized by insulin dependence, Type 2, resulting from the body's ineffective use of insulin, and Gestational diabetes which occurs during pregnancy[63]. Due to the variety of collateral effects and the risk of long-term complications, diabetes must be continuously monitored, and patient self-management is essential. Apart from the wide range of preventive recommendations, diabetes care includes an active role of the patient starting from the diet, education, and glycemic control[64].

2.2 Glucose sensing for diabetes monitoring

Patient self-monitoring of blood glucose is generally performed with a commercial device (Fig.16A) based on an amperometric electrochemical principle in which the glucose dehydrogenase (GDH) or glucose oxidase (GOx) layer on the working electrode converts glucose, producing an electron flow proportional to the number of glucose molecules present in the blood. One of the possible reactions can be:

$$\boldsymbol{Glucose + GOx - FAD^{+} \rightarrow Gluconolactone + GOx + FADH_2}$$

$$\boldsymbol{GOx - FADH_2 + O_2 \rightarrow GOx - FAD + H_2O_2}$$

$$\boldsymbol{H_2O_2 \rightarrow 2H^{+} + O_2 + 2e}$$

where FAD is the redox cofactor-flavin adenine dinucleotide that acts as electron acceptor.

These portable glucose biosensors have achieved enormous success in the market since they provide rapidity in the test result and high accuracy. However, they require a small drop of capillary blood to be fingerpicked with a needle and applied on the electrochemical test strip[65]. For instance, they present several inconveniences mostly related to the invasive sampling process which involves physical discomfort, especially for patients necessitating frequent measurement. A further issue concerns the possibility of bloodborne viral pathogens transmission which can occur when glucose monitoring equipment is shared, leading to inadvertent exposure to an infected person's blood[66].

Glucose biosensors based on these reactions are reagent-less since the mechanism relies on the direct transfer between the enzyme and the electrode. A step forward in these strategies has been the development of implantable, needle-type devices for continuous in-vivo monitoring (CGM) of blood glucose (Fig.16B). Currently available CGM sensors measure glucose levels with minimally invasive sampling, in particular exploiting the interstitial fluids (ISF) or by the application of electromagnetic radiations through the skin to blood vessels. The measurement is performed every 1-10 minutes, providing the patient with real-time results. However, CGM must comply with specific requirements like biocompatibility, calibration, long-term stability, and miniaturization[67].

Other available non-invasive techniques that have currently entered clinical use are near-infrared transcutaneous spectroscopy[68], breath acetone measurements[69], and other optical and electrical/electrochemical sensing techniques[70,71].

2.2.1 µPADs for glucose sensing

Simple visual µPADs are now emerging as valid alternatives to electrochemical sensors. A promising example of a paper-based analytical device made of GOx-loaded pluronic-based nanocarrier functionalized with an artificial peroxidase has been recently developed and tested in human serum samples (diluted 10 times). The one-pot enzymatic cascade reaction leads to the oxidation of a chromogenic substrate (2,2′-azino-bis(3-ethylbenzothiazoline-6-sulfonate). The color change obtained on the pad in the presence of increasing glucose concentrations can be appreciable by the naked-eye and it is further measured with a smartphone app (fig.16C). The prepared PAD enables quantitative measurements of human serum glucose ranging from normal levels to those typical for diabetics demonstrating a performance comparable to the commercial sensors[72].

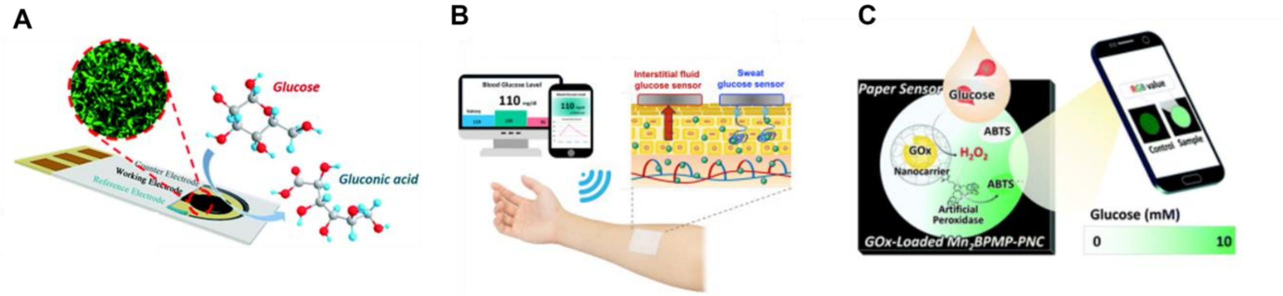
A
Glucose
Gluconic acid
Counter Electrode
Working Electrode
Reference Electrode
B
Blood Glucose Level
110 mg/dl
110
Interstitial fluid glucose sensor
Sweat glucose sensor
C
Paper Sensor
Glucose
ABTS
GOx
H_2O_2
Nanocarrier
ABTS
Artificial Peroxidase
GOx-Loaded Mn_2BPMP-PNC
RGB value
Control
Sample
Glucose (mM)
0
10

Figure 16. Glucose sensing strategies: A) Electrochemical sensor; B) Continuous blood glucose monitoring in interstitial fluid; C) µPAD[72].

2.2.2 Saliva as a biological matrix for glucose monitoring

A further possibility to overcome the invasiveness of the sampling approach is the use of saliva as a biological source. Saliva maintains the homeostasis of the oral cavity and, hence, serves as a source of biomarkers for early diagnosis of pathological conditions. It is non-invasively collected and its daily production ranges from 0.5 to 1.5 L. Blood glucose, specifically, passes across the salivary gland epithelium in a concentration-dependent manner; hence, it was found a statistically significant correlation between salivary and blood glucose levels. The salivary glucose level in healthy subjects is < 2 mg/dL, in controlled diabetic patients it reaches 4.26 mg/dL, while the mean concentration in an uncontrolled diabetic group is 11.3 mg/dL[73]. Some promising examples of highly sensitive and rapid salivary glucose sensors have been recently reported[74]. In particular, de Castro et al. developed a µPAD integrated into a silicone mouthguard wearable sensor for salivary glucose monitoring. The µPAD reached a LoD down to 27µmol/L, demonstrating results comparable to spectrophotometric measurements and paving the way for non-invasive and instrument-free self-monitoring of the diabetic condition[56].

As previously mentioned, salivary glucose is several times lower than blood glucose levels (ca. 100 mg/dL), therefore, it is necessary to significantly increase assay sensitivity, developing alternative glucose detection strategies.

2.2.3 Glucose sensing strategies based on AuNPs

In this regard, NPs offer enormous potential as a new generation of highly sensitive detectors both for their enhanced surface which maximizes the binding with the target and for their plasmonic properties. NPs, indeed, in particular noble metal NPs, are characterized by unique size, shape, and aggregation-dependent plasmonic properties that make them suitable candidates for the realization of naked-eye detection assays[34,75–78]. AuNPs, in this framework, have been largely employed as signal transducers for optical readouts in glucose biosensors[79–85]. A promising strategy based on the biocatalytic shape-altering of Au nanostars via Ag deposition has been proposed by Phiri et al. and the schematic illustration of the sensing mechanism is illustrated in fig.17. H_2O_2, produced by the oxidation of glucose, reduces Ag ions which deposit on the AuNP surface, previously functionalized with GOx, resulting in a shape alteration. The extent of the change in Au nanostar morphology is proportional to the concentration of glucose and it results in a spherical morphology characterized by different plasmonic properties. The fabricated glucose biosensor presents a very rapid kinetic and provides naked-eye detection, which allows for the technology transfer to other POC devices. The assay has been successfully applied on serum diluted 1000 times proving to be a promising candidate for clinical diagnosis, research, and development applications[86].

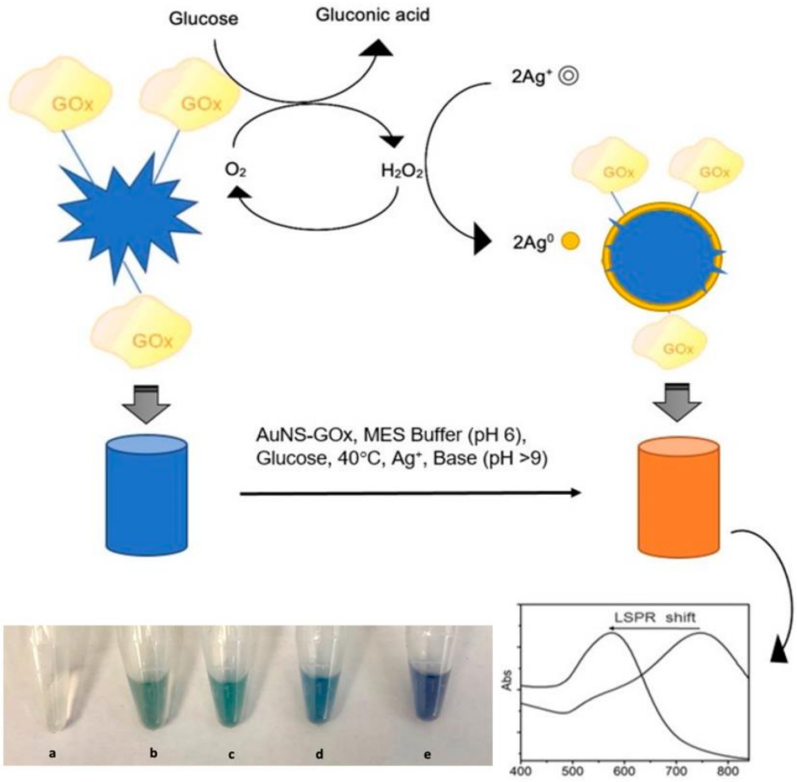
Glucose
Gluconic acid
GOx
O2
H2O2
2Ag+
2Ag0
AuNS-GOx, MES Buffer (pH 6),
Glucose, 40°C, Ag+, Base (pH >9)
a
b
c
d
e
LSPR shift
Abs
400
500
600
700
800

Figure 17. Scheme of the action mechanism of the glucose biosensor based on Au nanostars shape alteration; the insert picture shows the colorimetric response to different concentrations of glucose in diluted serum a) blank serum, b) Au nanostars in serum, c) 0 mmol/L glucose, d) 0.001 mmol/L glucose, e) 0.002 mmol/L glucose[86].

AuNPs have been largely exploited in sensing applications based on the aggregation strategy which induces a visible color change with a very fast response and high sensitivity[87]. However, the aggregation approach often requires NPs functionalization to specifically recognize the target. Furthermore, another issue concerns the formation of the biomolecular corona which occurs when the NPs enter in contact with biological fluids, leading the biomolecules to be attached on NPs surface and forming a corona (fig.18). The biomolecules create a near-monolayer called the hard corona, which is not irreversible, and a soft corona on top of it, characterized by a weak binding[88].

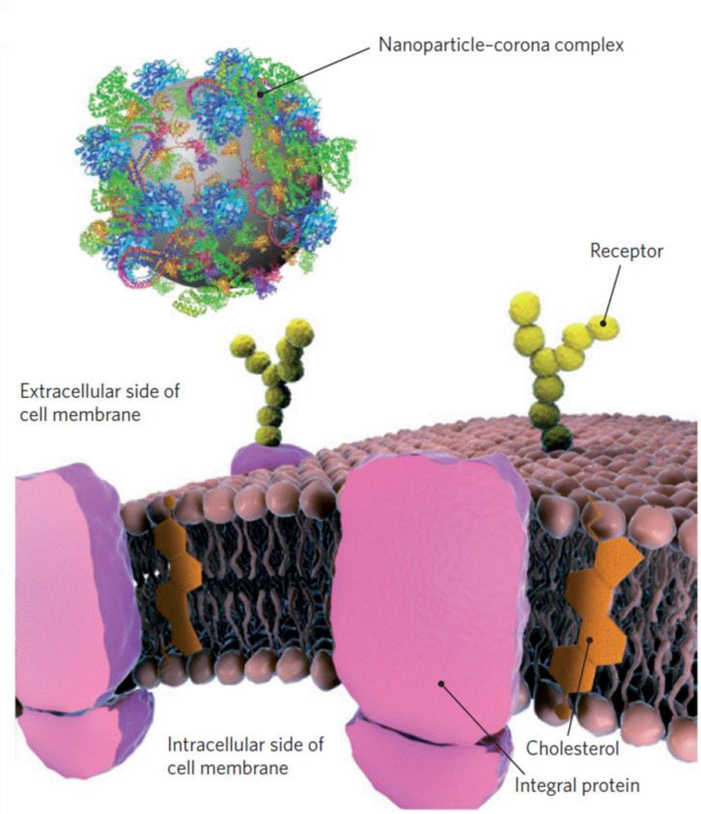
Nanoparticle-corona complex
Receptor
Extracellular side of cell membrane
Intracellular side of cell membrane
Cholesterol
Integral protein

Figure 18. NPs-corona complex in biological systems[88].

This NPs-biological interaction enables several important applications including drug delivery by NPs; however, the shelf of biomolecules on the surface strongly interferes with NPs properties. Indeed, biomolecules can potentially mask binding sites and functionalization and promote uncontrolled aggregation[89].

Another promising colorimetric sensing approach is the growth strategy which induces great variation in the LSPR in response to a size increase, as demonstrated by Rodríguez-Lorenzo et al.. The proposed approach relies on the formation of a silver coating around Au nanosensors due to the presence of GOx. This enzyme, in presence of glucose, produces H_20_2, which, in turn, reduces silver ions on the AuNPs surface, leading to NPs growth and an LSPR blueshift[90]. Although the growth strategy enables achieving very high sensitivity, in presence of proteins in the biological environment this approach can be directed and tuned, leading to anisotropic NPs morphologies. Proteins, indeed, can act like “surface active agents”, mimicking common surfactants like CTAB, promoting the reduction of metal salts and their further controlled deposition on the clusters for the realization of different morphologies like rods, prims, spheres, and hexagons. Bovine serum albumin (BSA) or lysozyme, for example, can form prisms and spheres, respectively, starting from Ag clusters (fig.19)[91].

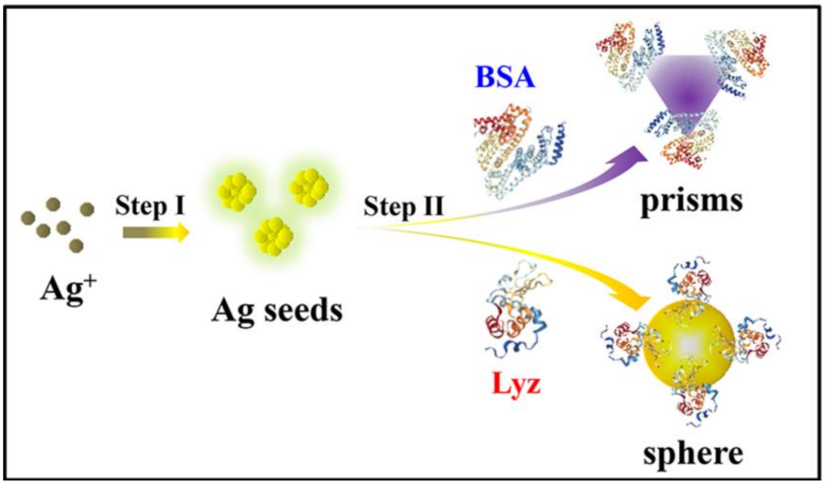

Figure 19. Controlled growth of Ag nanoclusters using BSA and lysozyme[91].

To overcome the uncontrolled growth of NPs in complex media, the etching approach has emerged as an alternative and promising strategy. AuNRs etching has been widely used for the realization of multicolorimetric POCT due to the presence of two plasmonic bands: the transverse and longitudinal mode bands, that correspond to electron oscillations perpendicular and parallel to the rod length direction and which are susceptible to variations in the aspect ratio, leading to significant spectral shift[36]. AuNRs etching has been efficiently exploited by Liu et al. for the detection of glucose in the blood. GOx catalyzes glucose oxidation, forming H_2O_2, which can transform into the free radical form, due to the presence of Fe^{2+} ions via Fenton and Fenton-like reactions[36]. These active radical species, like $^{\cdot}OH$, can efficiently oxidize AuNRs causing a blue shift of the LSPR which is proportional to the glucose concentration (see fig.20A). The presence of $^{\cdot}OH$ promotes a decrease in the aspect ratio from 4 to 2.1 (fig.20B), enabling a clear visible color change, exploitable for the realization of a POC platform for glucose testing[38].

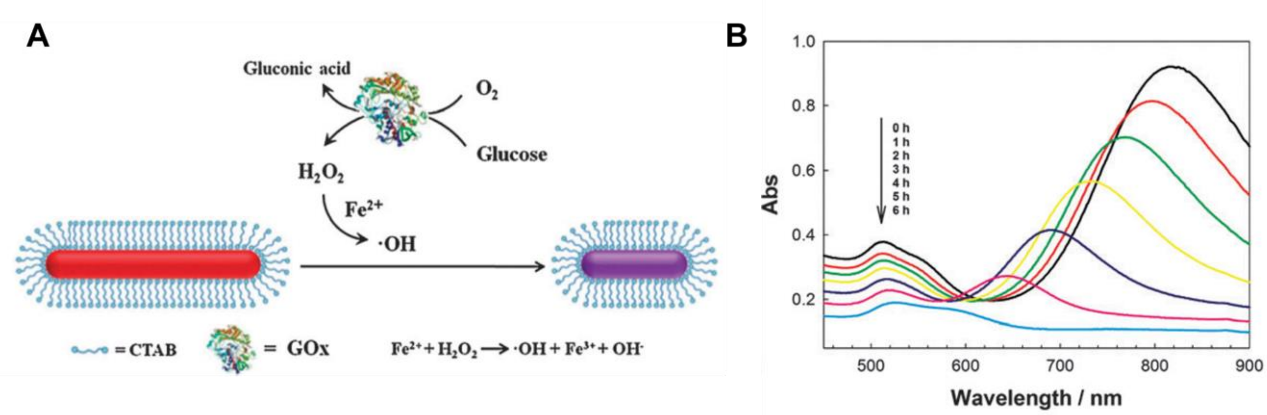

Figure 20. A) Reaction mechanism of the plasmonic glucose sensor; B) the UV-vis spectra change of AuNRs in the oxidation etching process[38].

An issue related to the etching approach is the optical density (OD) loss which naturally occurs as a consequence of NP dissolution. Indeed, as can be seen from the UV-vis spectra change of the AuNRs etching process (fig.20B), the blue shift upon the addition of 10 mM $\cdot OH$ is also accompanied by an absorbance decrease of about 0.8. This phenomenon is a clear disadvantage in the realization of a POC platform since the final read-out signal will be hardly appreciable by the naked-eye.

2.3 Our strategy: colorimetric nanoplasmonics for glucose sensing

Aiming to overcome the drawbacks of the existing techniques and realize a highly sensitive and naked-eye POC device for rapid salivary glucose detection, we develop a novel strategy that relies on AuNPs, GOx, and bromide ions (Br^-). The colorimetric approach involves a chemically induced reshaping of multibranched AuNPs (MGNPs), characterized by several tips and a vivid blue color, which gradually change into a spherical shape, in presence of the target, producing a blue-to-pink color change without OD loss[92].

2.3.1 Reshaping process

Our proposed colorimetric strategy is illustrated in fig.21. Specifically, the GOx enzyme oxidizes glucose forming H_20_2. Then, in presence of a large excess of bromide ions (Br^-), several potent etchants namely HBrO, Br_2, and Br_3 can be formed in a cascade reaction. When halide ions are exposed to different oxidants, like H_20_2, they become potent etchants, which can reduce Au^+/Au more efficiently than the oxidant[93–96]. Indeed, at certain conditions, H_20_2 can itself oxidize NPs; however, it requires a very long time (hours), and the process has low efficiency. On the contrary, these etchants can largely boost the oxidation process through multiple pathways, enabling a fast color change in a few minutes. These species promote the oxidation of MGNP surface atoms starting from the tips which represent the more sensitive units, characterized by the lowest energy plasmon mode[97]. The etching of the tips induces a morphological change into a spherical shape, characterized by a blue-shifted plasmon band, which corresponds to a pink color. Interestingly, contrary to what happens during etching, the reshaping process is characterized by a series of gold oxidation/reduction, mainly due to Br_2, which promotes the rearrangement of gold atoms from the surface convexity to the concavity, characterized by lower surface potential, leading to a more thermodynamically stable shape[98].

The novelty of our approach lies in its successful application in saliva where the mechanism seems even more stable than in water, due to the formation of the protein corona made of salivary proteins and metabolites(fig.21). Proteins like mucin, which are widely present in saliva, reduce the available surface of the NP by steric hindrance, avoiding unwanted interactions. Thiols like glutathione and cysteine, instead, act as surface ligands. This biomolecular coating protects and stabilizes MGNP surface atoms enabling the addition of a larger amount of Br^- with respect to that used in water solution, without occurring in false positive results. Indeed, an excess of the etchant would lead to uncontrolled fast etching and an immediate color change even in absence of glucose (control condition). In biological media, due to the presence of the protein corona, the control is better stabilized and the excess of Br^- enables a higher sensitivity and resolution. The biomolecular corona is also involved in the reshaping process, promoting it. Indeed, the protein layer protects more the core than the tips, that, in turn, are more susceptible to oxidation. The structural changes are also promoted by the oxidation of the salivary thiol ligands by Br_2 and, hence, the surface is more available for reshaping. Finally, thiols play a double role, both protecting the surface in absence of glucose and promoting the reshaping instead of etching since they foster gold atoms to rearrange in the surface concavities, avoiding NPs dissolution.

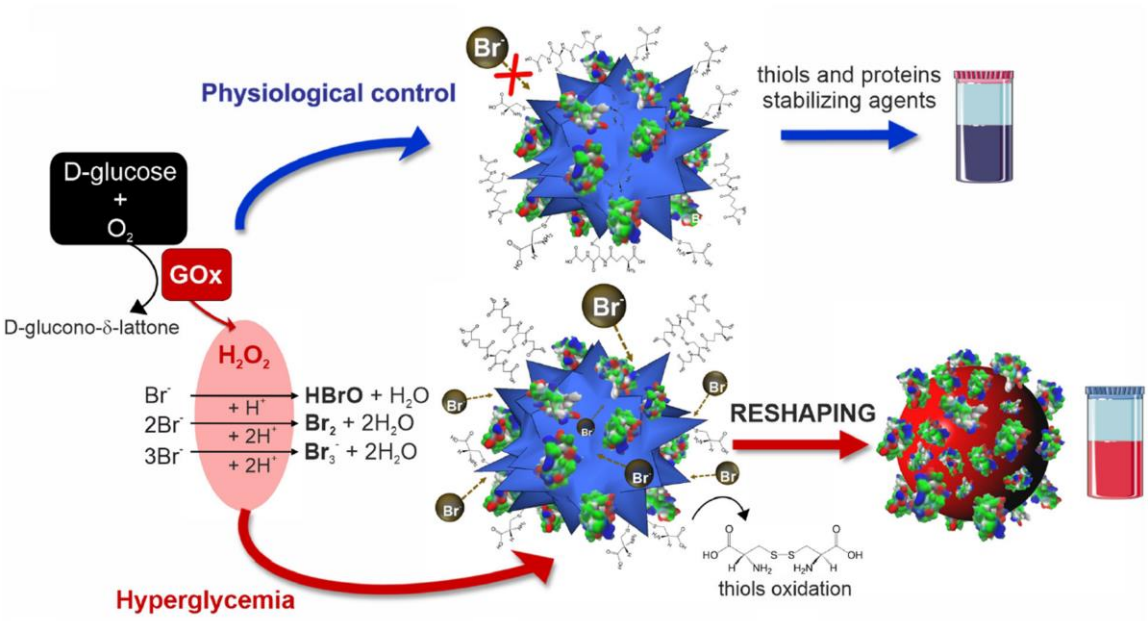
Br^-
Physiological control
thiols and proteins
stabilizing agents
D-glucose
+
O_2
GOx
D-glucono-δ-lattone
H_2O_2
Br^- $\xrightarrow{+H^+}$ HBrO + H_2O
$2Br^-$ $\xrightarrow{+2H^+}$ $Br_2 + 2H_2O$
$3Br^-$ $\xrightarrow{+2H^+}$ $Br_3^- + 2H_2O$
Br
RESHAPING
thiols oxidation
Hyperglycemia

Figure 21. Proposed mechanism of glucose sensing.

A step forward in the proposed sensing mechanism is its successful transfer on a solid substrate for the realization of a home-testing prototype for the self-monitoring of salivary glucose levels (fig.22). With this aim, MGNPs were immobilized (through filtration with a syringe) onto the selected membrane and, after a drying step, a layer of GOx was placed on it. Depositing reagents on the solid support strongly improves their stability over time, enabling the storage of the POCT for months at ambient conditions. As I have previously stressed, POC glucose devices are highly required to improve patient compliance with the therapy and to reduce the side effects of diabetes. The possibility to detect glucose in biological fluid collected with noninvasive approaches, like saliva, would be a great success for the diabetic community, especially for patients who require frequent measurements.

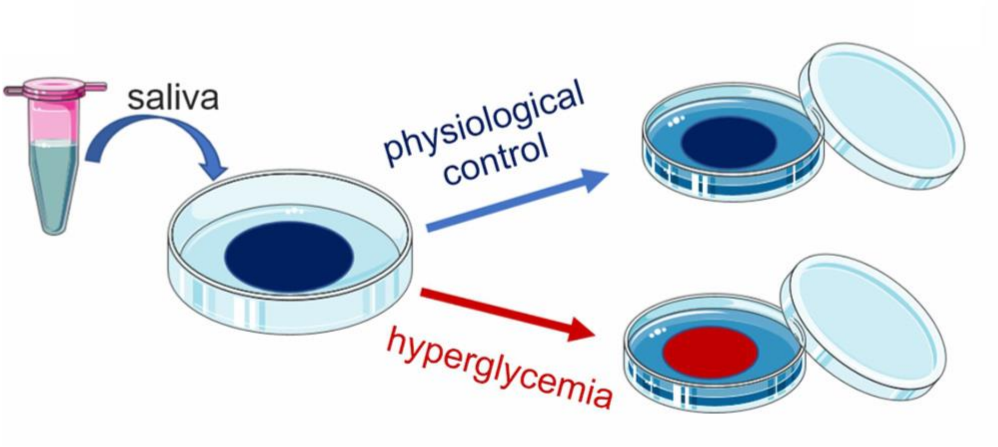
saliva
physiological control
hyperglycemia

Figure 22. Assay prototype for home-testing of salivary glucose.

A further advantage of our technique lies in its universality since it is versatile and easily adaptable to different targets. Indeed, it is worth mentioning that there are several other biomarkers that, like glucose, produce H_20_2 involving different oxidase enzymes. The proposed platform, under specific optimizations, can be extended to a variety of POCTs, aiming to detect pathological conditions like hypercholesterolemia or uricemia.

2.4 Results and discussions

2.4.1 Synthesis of multibranched AuNPs

The synthesis of MGNPs was achieved starting from AuNPs seed, following the common synthetic protocol developed by Turkevich's group[99]. In this approach, a gold precursor (generally the $HAuCl_4$ acid) was boiled and reduced to metallic gold, Au (0) using the reducing agent citrate. The activated Au (0) species underwent to nucleation process, leading to well-dispersed AuNPs, stabilized by citrate (fig.23).

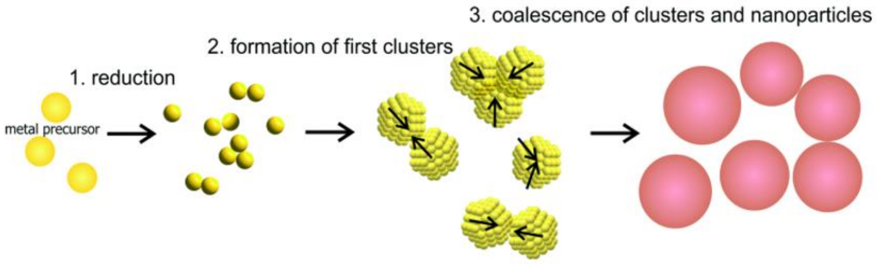
3. coalescence of clusters and nanoparticles
2. formation of first clusters
1. reduction
metal precursor

Figure 23. Synthesis of 15 nm AuNPs following Turkevich's method[99].

With some modifications of this protocol regarding $HAuCl_4$/citrate ratio, pH, and temperature, in our group, we achieved well-monodisperse and stable AuNPs of 15 nm, fully characterized with common laboratory techniques (see fig.24), confirming reproducible features.

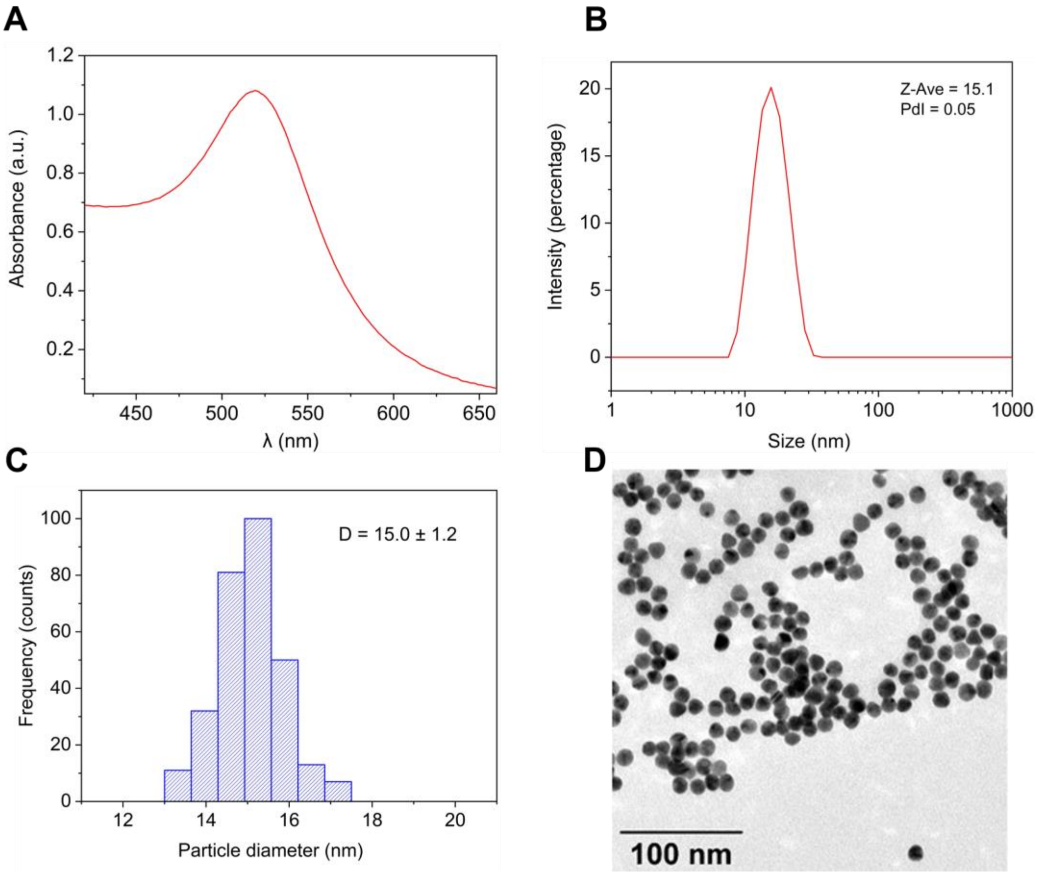

Figure 24. 15 nm AuNPs characterization including A) UV-vis absorption spectrum; B) DLS measurement; C) TEM size distribution analysis; D) TEM micrograph.

The above 15 nm spherical AuNPs were used as seeds for the synthesis of 60 nm MGNPs. This particular morphology was realized following and slightly modifying the Maiorano-Pompa method[100], which is a seed-mediated growth[101]. The protocol relied on the ability of hydroxylamine to efficiently and selectively reduce Au (III) to 0 valent metal in presence of Au seeds. HEPES solution ensured NPs colloidal stability and acted as a shape-directed agent, enabling the formation of several small tips. Optimizations of shape and plasmonic features were performed by varying reagents' stoichiometry until the realization of well-monodispersed MGNPs, with an average size of 60 nm, fully characterized with common laboratory instrumentation (see fig.25).

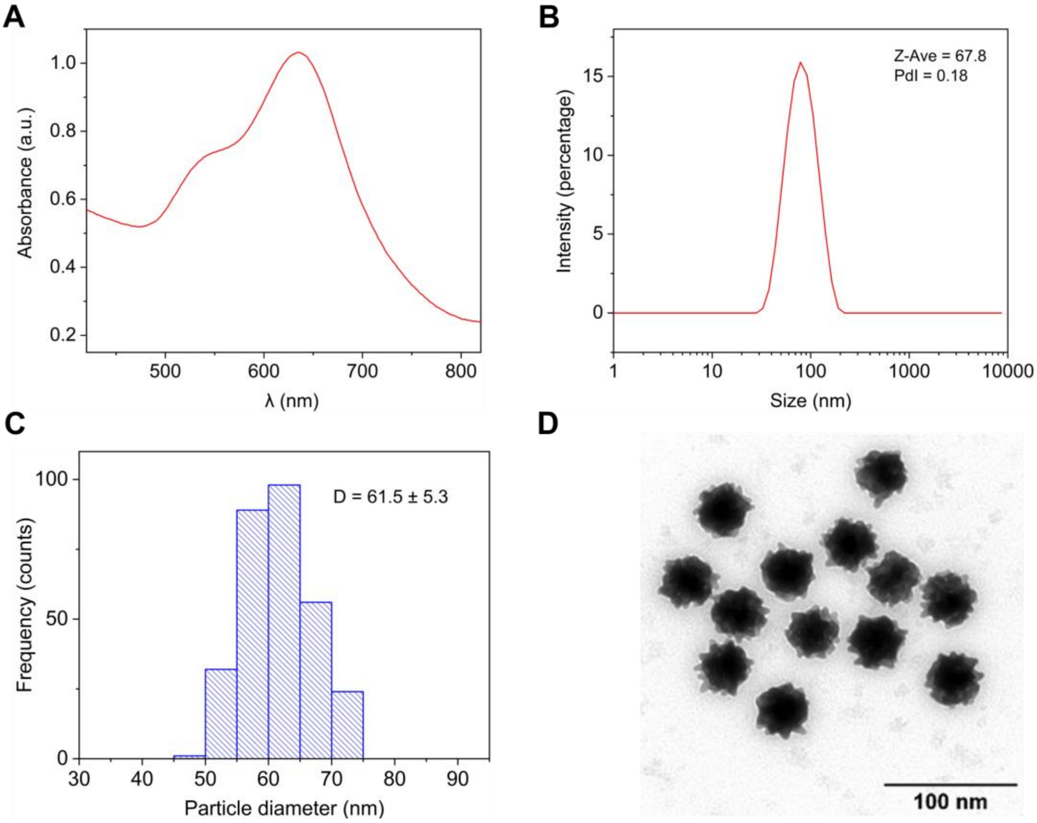

Figure 25. 60 nm MGNPs characterization including A) UV-vis absorption spectrum; B) DLS measurement; C) TEM size distribution analysis; D) TEM micrograph.

2.4.2 Optimization of MGNPs morphology

Our rapid and highly sensitive glucose sensing strategy was based on the reshaping of MGNPs, which led to a rapid change of shape and color in the presence of hyperglycemic conditions, enabling naked-eye detection. For the optimization of the colorimetric mechanism and the realization of the POC prototype, I started performing the assay in water and with a simplified mechanism that did not include the enzyme. As discussed before and it is clearly shown in fig.26, 60 nm MGNPs, in presence of halogen ions and H_20_2, underwent a fast etching of the small tips (of about 8 nm length), leading to a final spherical shape with a blue-shifted plasmon band. Regarding the optimization of MGNPs morphology, I observed that small and numerous tips, instead of long spiked structures, enabled a clear color distinction with minimal morphological changes; hence, I tuned HEPES concentration, which acted as shape directing agent, to obtain the final shape that is illustrated in fig.25D. This particular morphology was characterized by an absorption peak around 640-650 nm, responsible for the blue color of the colloidal suspension, while, after the reshaping, the spherical NP absorbed at 550 nm, showing a distinctive pink color.

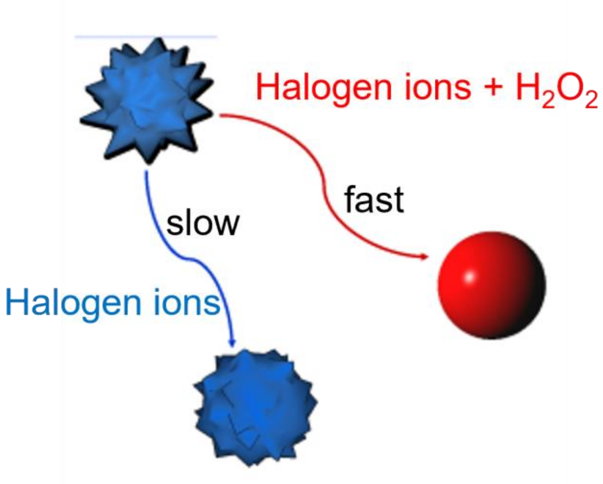

Figure 26. Proposed mechanism of MGNPs reshaping in water solution.

2.4.3 Optimization of the reshaping process

I first optimized the pH conditions monitoring the spectral shift over the addition of H_20_2. As it is illustrated in fig.27A, I tested the reshaping process in three acetate buffer solutions (pH 4.5, 5.0, 5.5), with the same KBr and H_20_2 concentrations. Remarkably the LSPR shifted in less than 10 minutes for all the pH conditions, showing a faster and wider blue shift with an acidic pH. On the contrary, controls showed only little variations in all the proposed conditions, showing minimal shift only when pH=4.5 was tested. Instead, as it is shown in fig.27B, the NPs remained generally stable for 1 hour in an acetate buffer solution pH=5 showing neither interference nor aspecific reactivity; hence, pH=5 was selected as the optimal compromise between the enzyme activity and the NP stability.

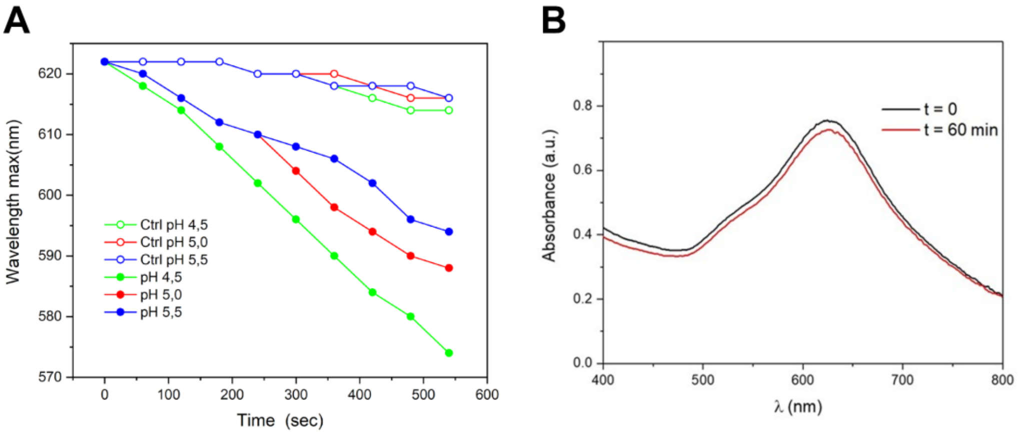

Figure 27. A) LSPR evolution over time shift as a function of the pH; B) Stability of the MGNPs at pH=5.

As I mentioned before, H_20_2 could itself act as an etchant in the reshaping of MGNPs, however, the process generally occurred in several hours. To shorten reaction time, I tested the oxidation ability of different halogen species, namely Br$^-$, chloride (Cl$^-$), and iodide (I$^-$), which can promote and boost the reshaping process due to the production of more potent etchants[93–96]. As it is clearly illustrated in fig.28, when 3 mM H_20_2 was tested in presence of optimized concentrations of the three ions, I$^-$ led to the widest LSPR shift; indeed, after the first 2 minutes, the spectral shift was about 40 nm. However, aspecific effects largely occurred, since even the control underwent a remarkable blue shift. On the contrary, reshaping mediated by Cl$^-$ was almost negligible. Instead, Br$^-$ enabled the best spectral shift in a relatively short time (10 min) without producing false positive results since controls remained almost stable (blue shift of about 20 nm).

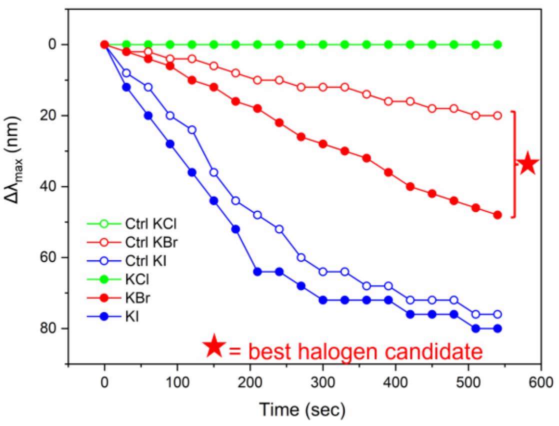

Figure 28. LSPR evolution of the reshaping in presence of different halogens.

The spectral shift associated with increasing H_20_2 concentrations, under the optimized halogen conditions (50 mM Br$^-$), was further tested with three independent experiments (see fig.29). As is shown in fig.29A, an increase in the H_20_2 amount induced a faster and wider spectral shift, confirming its contribution in the reshaping of MGNPs. The blue shift can be further observed in fig.29B where H_20_2 concentration was lowered to the range of interest (1-3 mM). However, when concentrations overcame 10 mM, OD loss occurred due to the aspecific corrosion of the NPs as evidenced by the spectral shift in fig.29.

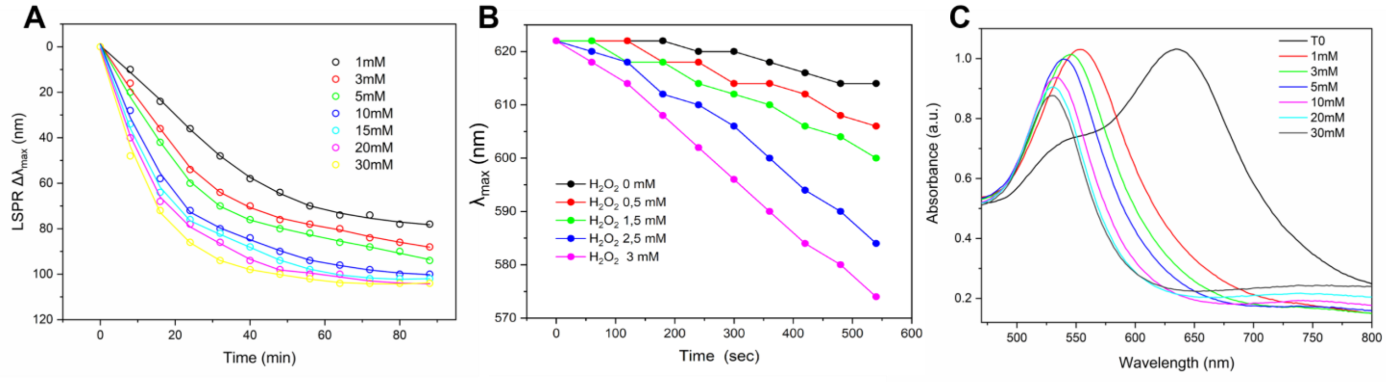

Figure 29. A) LSPR evolution over time of the reshaping process in presence of increasing H_20_2 concentrations; B) λ evolution over time of the reshaping process in presence of increasing H_20_2 concentrations in the range of interest; C) absorption spectra related to MGNPs before reshaping (T0) and after the reaction with increasing H_20_2 concentrations (reaction time: 90min).

Under the optimized assay conditions (pH=5, KBr= 50 mM, and H_20_2 = 3 mM), the reshaping process was evaluated for 90 min, recording the evolution over time of the absorption spectra. As it is immediately visualized in fig.30, the aspecific etching of NPs was almost completely avoided in the optimized conditions, even in the long-term. Indeed, the decrease in intensity was negligible between the starting and the final absorbance. Moreover, the spectral shift was very fast and wide reaching a final peak at 550 nm after 90 minutes, which could be appreciable by the naked-eye.

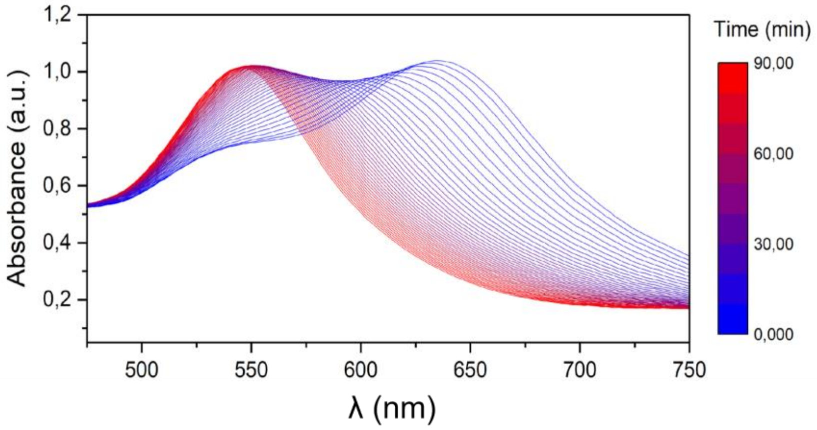

Figure 30. Absorption spectra related to the MGNP reshaping process under the optimized conditions.

2.4.4 Application in saliva

An important issue concerned the aspecific and uncontrolled etching which naturally occurred when the molar ratio between the reagents was slightly modified. Interestingly, a strikingly improved performance was achieved by adapting the platform in saliva. As I mentioned before, the presence of proteins and salivary thiols, which create the biomolecular corona, could protect the NPs surface and stabilize the surface atoms. I first performed some characterizations of MGNPs in the biological media. As it is illustrated in fig.31A, I measured the absorption spectrum of MGNPs in saliva, comparing it with that in acetate buffer demonstrating that a red shift naturally occurred when biomolecules create the corona around the NP, due to the morphological growth. Then, I proved that MGNPs maintained their plasmonic properties both in saliva and in acetate buffer containing GOx (fig.31B and C), confirming that the enzyme did not interfere with the LSPR. Finally, I demonstrated the colloidal stability of MGNPs in saliva when incubated with GOx for 1 hour (fig.31D). When MGNPs were incubated in saliva, the absorption spectrum did not suffer from any shift, demonstrating that the physicochemical properties were not altered in this matrix and proving that the proteins and metabolites protected and stabilized the surface atoms.

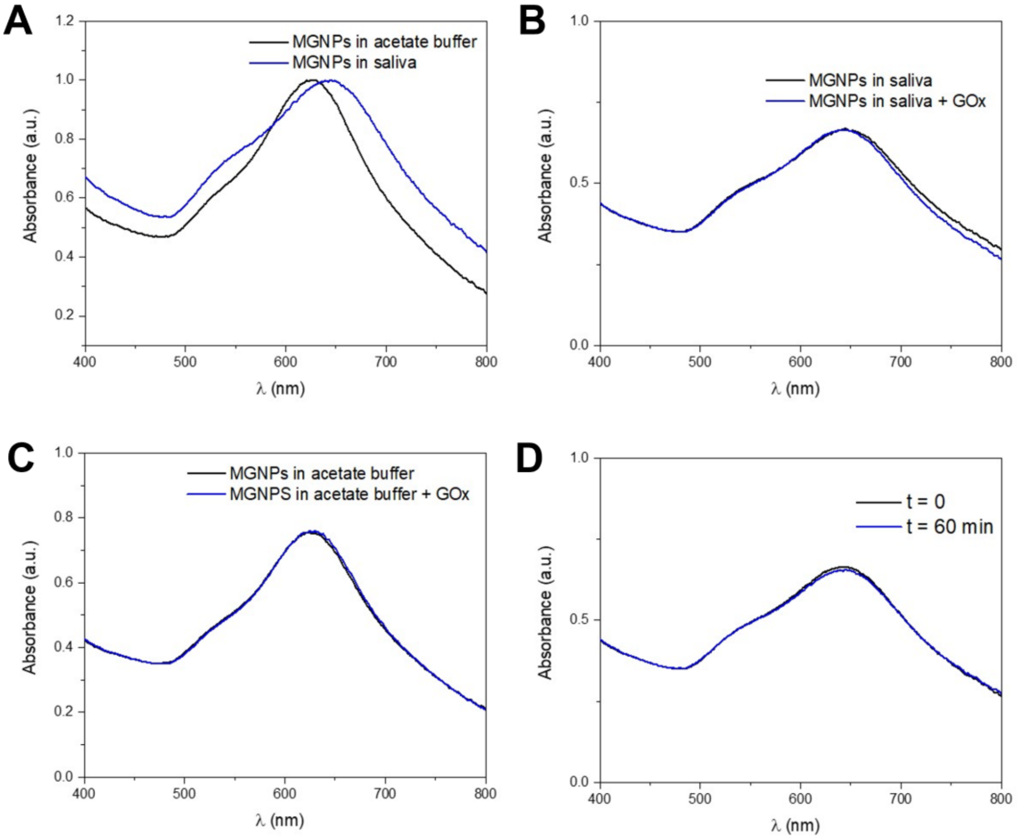

Figure 31. A) LSPR Red-shift related to the protein corona; B) MGNPs stability in saliva and in presence of GOx; C) MGNPs stability in acetate buffer and in presence of GOx; D) MGNPs stability in saliva after 1 hour of incubation with GOx.

The organic shield enabled to use higher Br^- concentrations compared to those in water and, in turn, a wider and faster spectral shift could be achieved, avoiding uncontrolled fast etching and color change in absence of glucose. Therefore, the assay conducted in saliva showed a better performance in terms of resolution and sensitivity since a significant extension of the dynamic range of the assay along with a faster response and a lower detection limit could be achieved. I tested the reshaping process in saliva collecting unstimulated samples from healthy donors, which I used as controls. To simulate hyperglycemia conditions, I supplemented saliva with glucose solutions to reach pathological concentrations (2 mM). In saliva, the ratio between reagents was finely tuned increasing KBr concentration up to 5 M, without introducing H_2O_2 in the reaction but enabling its formation from the reaction between GOx and glucose. First, I confirmed the superior performance of MGNPs in saliva by comparing the LSPR evolution over time in saliva and water (fig.32A), under the respectively optimized conditions of KBr and using the same NPs number and glucose concentrations (2 mM). As is clearly seen from the red lines in the graph, in saliva the spectral shift was wider, and no significant OD loss could be observed. Fig.32B and C represent the spectral shift of MGNPs in saliva when the assay was performed in pathological (B) and physiological (C) conditions. While in C) the blue shift is negligible, in B) MGNPs reach a final absorption peak at about 550 nm, without any intensity loss. Finally, I acquired TEM imaging of MGNPs after the assay performed in non-supplemented (ctrl) (D) and supplemented saliva(sample) (E), demonstrating negligible unspecific etching in the control and a remarkable reshaping in the sample: NPs became almost completely spherical (fig.32E). I further analyzed the TEM images of the MGNPs in control and sample solutions recording the dimensions of the tips and the internal diameter (core), not considering the tip. The statistical graphs (fig.32F) show a shortening of the nanostructure surface in hyperglycemic conditions but a final size distribution compatible with a redistribution of the MGNPs gold atoms onto the surface concavities, with a negligible loss of the metal atoms. The last graph in fig.32F further confirms the redistribution of the atoms on the NP surface since the sample core size seems bigger than that of the control, excluding MGNPs dissolution, typical of the etching approach. The negligible OD loss, which corresponds to a minimal color intensity decrease, is a promising achievement in naked-eye glucose sensing.

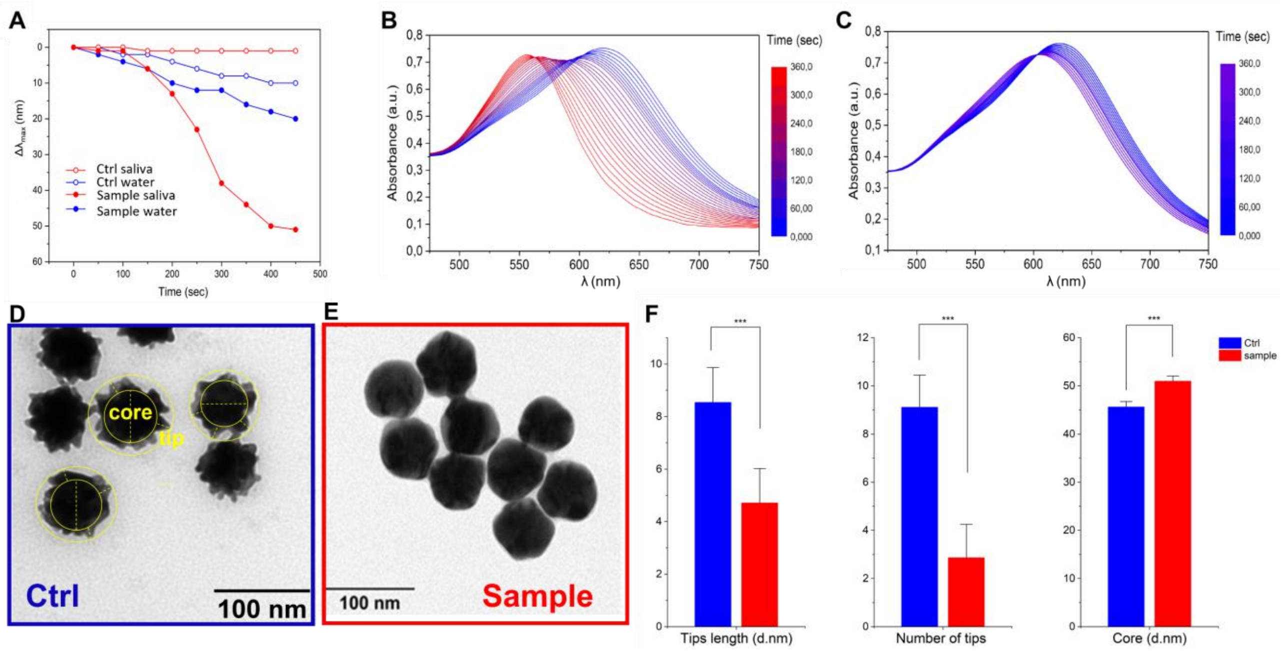

Figure 32. A) LSPR λ_{max} evolution over time of MGNPs reshaping in water (blue curves) and saliva; MGNPs absorption spectra when the assay is performed in glucose-supplemented saliva B) and

physiological saliva C); TEM micrograph of MGNPs after the assay with physiological saliva (ctrl) D) and glucose supplemented saliva (sample) E); F) Statistical TEM analyses measuring tips and core dimensions of the ctrl and sample.

2.4.5 Development of a home-testing device prototype

The next step was the realization of a home-testing device prototype and, with this aim, I transferred the sensing strategy on a solid support. I tested different materials (including cellulose acetate, nitrocellulose, nylon, and PVDF) that I embedded with a precise amount of MGNPs through a simple injection. Fig.33A shows the mechanism of NPs immobilization which relied on the use of a syringe containing MGNPs suspension, and a filter holder where the solid support was placed. After drying the substrate under vacuum, a layer of GOx was deposited on top of it aiming to have all the reagents embedded on the final device and ready for the test. Among the different substrates, I selected nylon both for its structural properties of wettability and hydrophobicity and because it retained the largest amount of MGNPs. Indeed, as is clearly shown in fig.33B, analyzing the spectra of the NPs suspensions resulted from the injection on the tested substrates, only nylon led to an almost colorless filtrate, indicating that it enabled the immobilization of a reproducible particle amount in a few seconds. Furthermore, a homogeneous deposition was achieved since the membranes acquired a uniform blue color with no imperfections. This is an important achievement for the final use of the device since the color change occurred on the solid support evenly, enabling to better interpret the colorimetric read-out and to facilitate the smartphone acquisition.

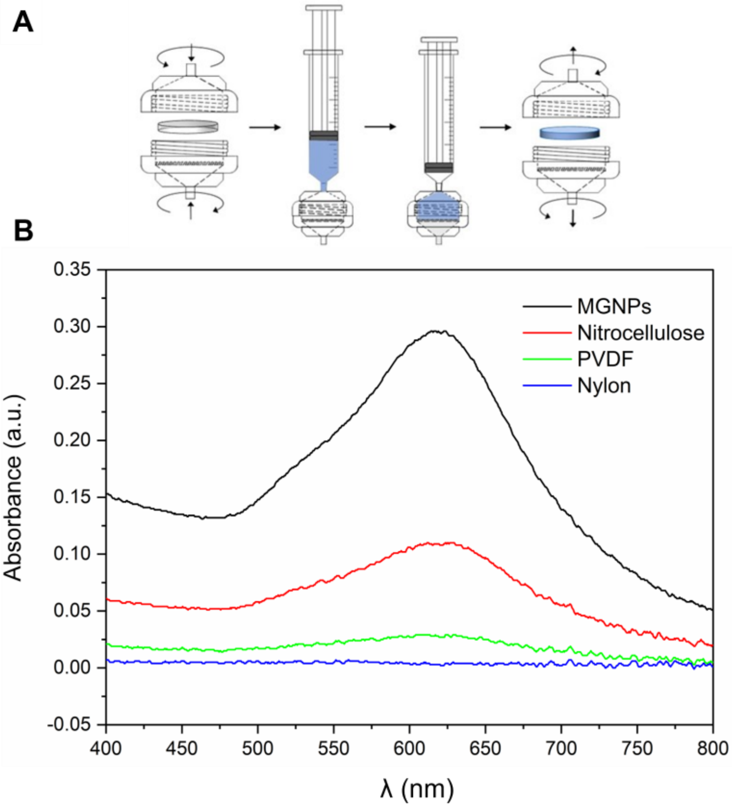

Figure 33. A) Mechanism involved in MGNPs transfer on a solid support; B) UV-vis spectra of the remaining MGNPs suspensions after their immobilization on different substrates.

After the preparation of the dipstick-like prototype, I validated its performance, by adding 20 µL of saliva supplemented with two glucose concentrations (1.5 (S1) and 3 (S2) mg/dL), which reproduced non-physiological conditions. I recorded photos of the device after 5 and 10 minutes. As it is illustrated in fig.34A, a visible and rapid color change was appreciable within 10/15 minutes, depending on the glucose concentration. Indeed, for lower glucose supplement a less striking color change was achieved (S1 in the figure). I further proved the reliability of the assay, testing the saliva of 4 healthy donors and supplementing them with 1.5 (S1), 3 (S2), and 5 (S3) mg/dL (fig.34B). I also included three controls in which the assay was performed on non-supplemented saliva but in absence of GOx (Ctrl 1) or in presence of denatured GOx (Ctrl 2), and with active GOx (Ctrl 3), to exclude false positive results.

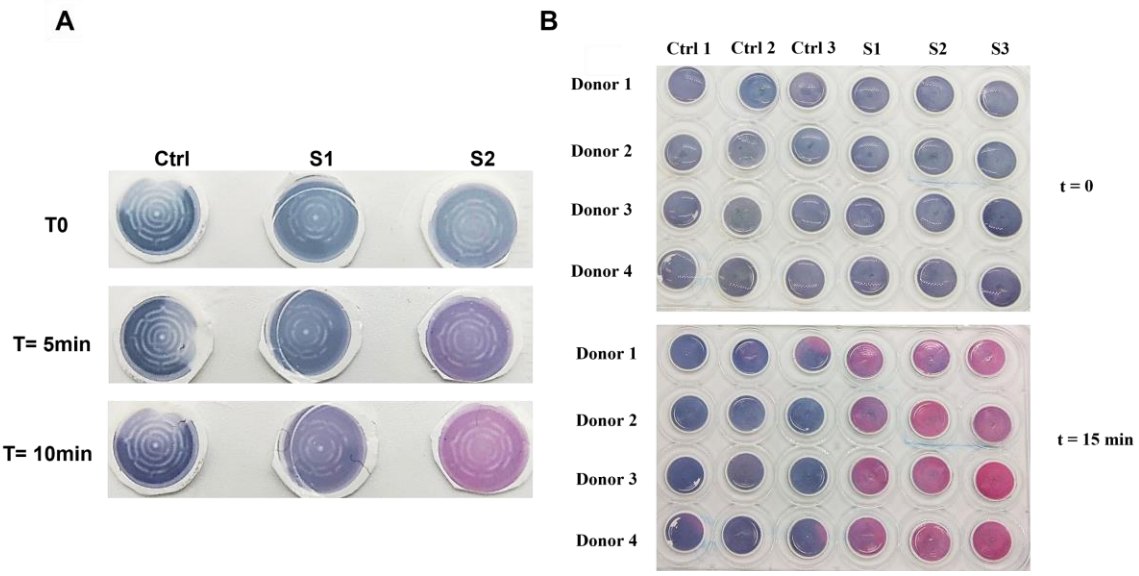

Figure 34. A) Colorimetric assay applied on healthy saliva (Ctrl), saliva supplemented with 1.5 mg/dL (S1) and 3 mg/dL (S2) glucose; B) Validation of the device prototype on different saliva samples including the controls: in absence of GOx (Ctrl1), with denatured GOx (Ctrl2), and with GOx (Ctrl3), and three supplemented samples: S1 (+1.5 mg/dL), S2 (+3 mg/dL) and S3 (+5 mg/dL).

I further analyzed two devices treated with native saliva (Ctrl) and supplemented saliva (S2 in the figure) recording the diffuse mode reflectance spectra of the detection zone(fig.35A). Reflectance spectroscopy was used to characterize the target-induced color change. As illustrated in fig.35A, Ctrl displayed a minimum reflectance peak at 600 nm, while most of the reflected light was in the range from 400 to 500 nm. On the other hand, S2 showed a spectral shift in the reflectance spectra of about 50 nm and the reflected percentage increased in the range from 650 and 800 nm. Ctrl was blue in terms of perceived color, while S2 turned red after the assay, as shown by the spectral shift. Then, I recorded SEM images of MGNPs in the two samples to demonstrate and further confirm that reshaping occurred even on the solid substrate (fig.35B). The micrographs in fig. 35B display a sensor area of the substrates treated with Ctrl (blue) and S2 (red). The detection zones presented a monodisperse and stable layer of active MGNPs (Ctrl) and spherical AuNPs (S2). In these higher magnification images, multibranched and spherical structures could be appreciated, confirming that the color change was primary due to the reshaping mechanism.

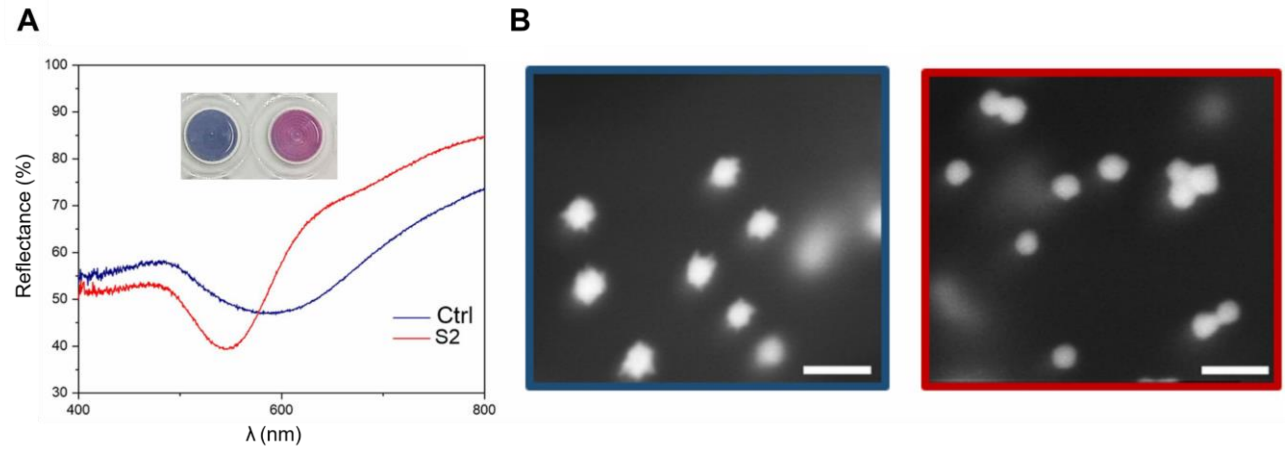

Figure 35. A) Reflectance spectra of the nylon membranes treated with native saliva (Ctrl) and supplemented saliva (S2) (picture in insert shows the colorimetric assay performed on the dipstick prototype); B) HR-SEM micrographs of ctrl (blue) and S2 (red).

Concerning the device prototype, I found that, when all the reagents were immobilized on the nylon substrate, the stability was strongly improved. Indeed, I tested the performance of the device over time up to 6 months testing non-supplemented saliva and saliva spiked with 1.5 mg/dL and 3 mg/dL to verify that the detection limit was not compromised over time (see fig.36). As it is shown in the pictures, the result remained unaltered compared with the test performed at time 0. This is an important achievement since the colloidal suspension of MGNPs in water normally undergoes aspecific etching over time, losing the original shape and characteristic plasmonic properties. Furthermore, this result demonstrated that the proposed prototype could be stored at least for 6 months, maintaining its reactivity and stability unaltered, paving the way for the realization of a test strip for the home testing of salivary glucose.

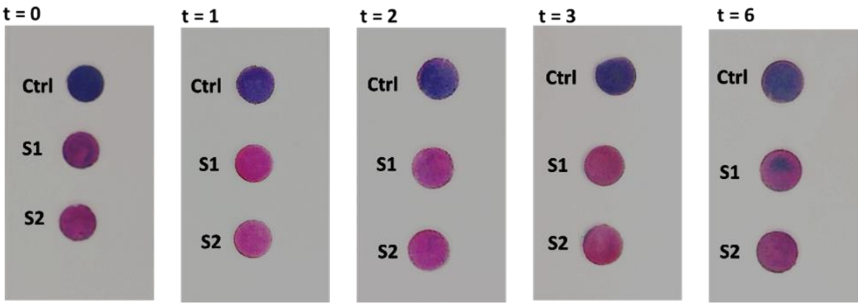

Figure 36. Stability test of the home-testing device prototype over time (t= 0, 1,2,3, and 6 months).

2.4.6 Assay validation on real diabetic saliva samples

Finally, I optimized the assay prototype for the analyses on real samples of healthy and diabetic donors. From the literature, I stated that the physiological glucose concentration in saliva is <2 mg/dL (<130 mg/dL in serum) while ≥4 mg/dL (≥ 160 mg/dL) corresponds to hyperglycemic condition. However, the correlation between hematic and salivary glucose is not well defined and constant over the whole range of concentrations[102]. With these considerations, I set a target threshold of 4 ± 0.5 mg/dL, aiming at an ON/OFF signal as an alarm for healthcare and I optimized the conditions to achieve an evident pink color change in case of values above this threshold. To make the colorimetric change numerically estimable, I collected the RGB coordinates of the treated substrate after 15 minutes of the assay, using a smartphone application namely ColorGrab. Then I calculated ΔRGB obtained at different glucose concentrations. To better illustrate the ΔRGB variability and ΔRGB value range, I normalized six saliva samples with glucose spikes to reach the final values of 2.5, 4, and 6 mg/dL (see fig.37A) and I plotted these concentrations against the respective ΔRGB. From this graph, I was able to better identify my threshold (4 mg/dL) which corresponded to a ΔRGB ≥ 30 (± 10). Then, to validate the reliability and validation of the assay, I performed the colorimetric test on twenty real saliva samples including eight healthy donors and twelve diabetic subjects and I compared the colorimetric result with a commercially available glucose assay kit, chosen as a standard reference technique (fig.37B). An evident color change was achieved for salivary glucose concentrations ≥ 4 (± 0.5) mg/dL after 15 min of the test (red dot in figure), while little or no color change was obtained for physiological concentrations (ΔRGB < 15 ± 5) (blue dot in figure). From these results I could conclude that my rapid assay prototype presented good reliability (95%) compared with standard techniques, paving the way for concrete future applications.

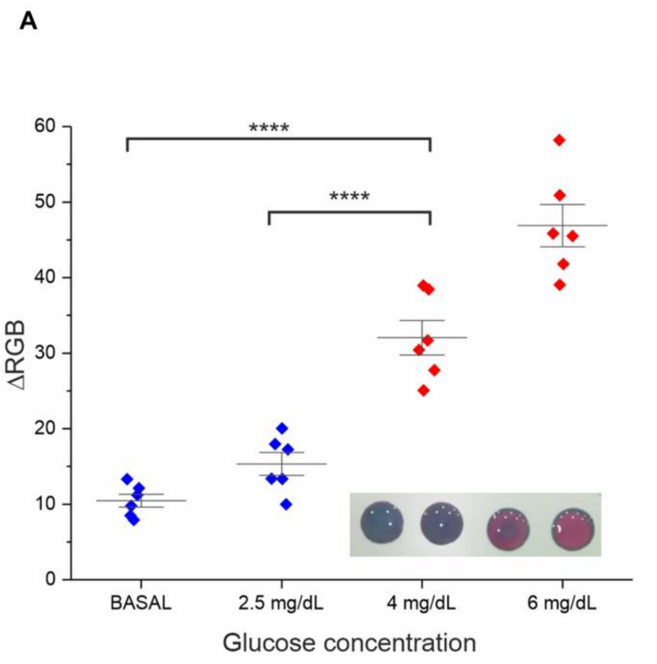

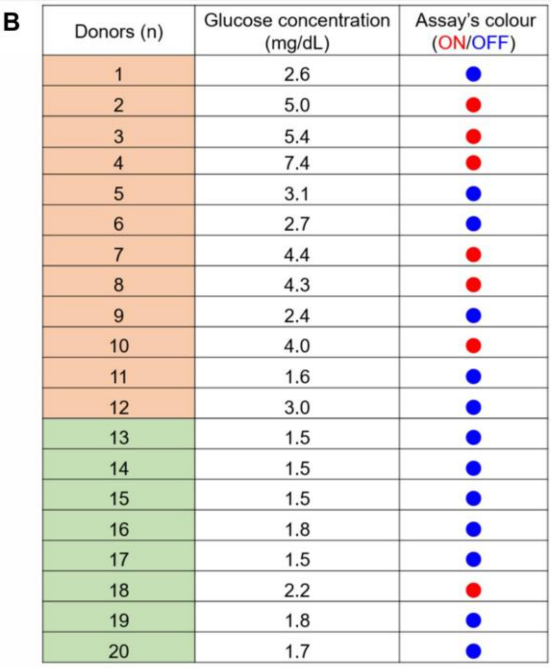

Donors (n)	Glucose concentration (mg/dL)	Assay's colour (ON/OFF)
1	2.6	🔵
2	5.0	🔴
3	5.4	🔴
4	7.4	🔴
5	3.1	🔵
6	2.7	🔵
7	4.4	🔴
8	4.3	🔴
9	2.4	🔵
10	4.0	🔴
11	1.6	🔵
12	3.0	🔵
13	1.5	🔵
14	1.5	🔵
15	1.5	🔵
16	1.8	🔵
17	1.5	🔵
18	2.2	🔴
19	1.8	🔵
20	1.7	🔵

Figure 37. A) Validation of the RGB-based readout obtained by testing six saliva samples normalized with glucose spikes to reach 2.5, 4, and 6 mg/dL (representative image of the color

change in the insert) and calculating ΔRGB with a smartphone app after 15 minutes of the assay. The statistical significance was determined using a one-way ANOVA and Tukey's multiple comparison test (****$P < 0.0001$); B) Results of the proposed assay performed on 20 donors compared with the commercially available glucose assay kit (green: healthy patients, orange: diabetic group).

The test was replicated using the same sample and different independently produced devices, confirming the reproducibility of the assay. Concerning the analytical performance, I employed the acquired ΔRGB, obtained at different glucose concentrations, to numerically estimate the detection limit. The LoD calculated by testing six saliva samples from healthy donors (glucose concentration <2 mg/dL), was established at 0.4 mg/dL. This result was comparable to other reported glucose colorimetric sensors[56,103]. However, due to the variability in the salivary composition, when saliva samples from multiple different donors were tested, LoD increased up to 1.4 mg/dL (see the plot in fig.38). The achieved result, still enabled an ON/OFF response, being more representative and realistic of the intrinsic biological variability of saliva samples.

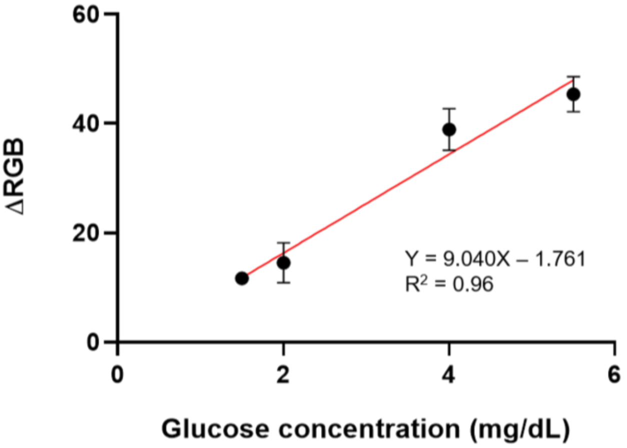

Figure 38. Analytical plot for LOD calculation.

2.5 Materials and methods

2.5.1 Chemicals

Hydrogen tetrachloroaurate ($HAuCl_4$) and hydroxylamine sulfate were purchased from Alfa Aesar. Trisodium citrate, HEPES, potassium bromide (KBr), potassium chloride (KCl), potassium iodide (KI), D-(+)-glucose, Glucose Oxidase from Aspergillus (Type X-S) were purchased from Sigma-Aldrich. Nylon membrane filters (pore size 0.45 µm), and polyvinylidene fluoride (PDVF) membrane filters (pore size 0.45 µm, hydrophilic) were purchased from Sigma-Aldrich. The syringe filter holder (polycarbonate) was purchased from Sartorius. A high-sensitivity glucose assay kit (Merck-MAK181-

1KT) was used as the reference standard technique. Physiological saliva samples were collected by healthy donors, with the approval of the Ethical Committee. Hyperglycemic saliva samples were provided by the San Matteo hospital of Pavia.

2.5.2 Instrumentation

Dynamic Light Scattering (DLS) Malvern Panalytical, Transmission Electron Microscope JOEL JEM 1400, NanoDrop® (wavelength Accuracy ± 1 nm, absorbance accuracy 3 % at 0.74 Abs@350nm) Thermo Fisher, Ocean Optics Spectrophotometer equipped with a reflection probe and an OCEAN-HDX-XR detector, Tecan Spark® multimode microplate reader (wavelength accuracy < 0.3 nm, absorbance accuracy < 0.5%@260 nm).

2.5.3 Synthesis of 15 nm AuNPs

The synthesis of colloidal 15nm AuNPs relied on a citrate reduction[99]. All the glassware and the magnetic stir-bar were washed with aqua regia ($HCl:HNO_3$ 3:1). 250 mL of a solution of 1 mM of $HAuCl_4$ was added in a 500 mL round-bottom flask, connected to a bulb condenser, and placed in a glycerol bath. After reaching the boiling point, 25 mL of 40 mM trisodium citrate solution was added to the flask under vigorous stirring. After 15 min a red wine color appeared. At the end of the reaction, the flask was placed in an ice bath, enabling it to rapidly reach room temperature. The suspension was filtered with a 0.2 µm cellulose acetate syringe filter and stored at 4°C.

2.5.4 Characterization of 15 nm AuNPs

The prepared AuNPs were characterized using UV-vis spectroscopy, TEM, and DLS. Particularly, 600 µL of the synthesized NPs with a concentration of about 2 nM were spectrophotometrically read through a disposable polystyrene cuvette. For the TEM analysis, 3 µL of 2 nM AuNPs suspension were placed on oxygen plasma cleaned grid. Finally, the DLS reading was obtained placing 600 µL of 2 nM AuNPs suspension in a disposable polystyrene cuvette and performing 3 measurements consisting of 11 runs (see fig.24).

2.5.5 Synthesis of MGNPs

The synthesis of 60nm MGNPs was performed by slightly modified Maiorano-Pompa protocol[100] with a seeded growth approach. All the glassware and the magnetic stir-bar were washed with aqua regia ($HCl:HNO_3$ 3:1). Ratio between the reagents was finely tuned to obtain MGNPs characterized by several small tips and an LSPR peak around 650 nm. Briefly, in a 500 mL round-bottom flask 250 mL of 50 mM HEPES solution, pH=7, under vigorous stirring were added. Then, 6.5 mL of the previously prepared seeds at a concentration of 1.8 nM, 0.28 mL of 100 mM $HAuCl_4$, and 0.8 mL of

100 mM of hydroxylamine sulfate were added consequently. After 15-20 minutes at room temperature, a blue color appeared. At the end of the reaction, centrifugation of the suspension was performed (4000 rcf, 25 min) to remove residual reagents excess.

2.5.6 Characterization of MGNPs

The prepared AuNPs were characterized using UV-vis spectroscopy, TEM, and DLS. Particularly, 600 µL of the synthesized MGNPs diluted to a concentration of about 2 nM in water were spectrophotometrically read through a disposable polystyrene cuvette. For the TEM analysis, 3 µL of 2 nM MGNPs suspension were placed on oxygen plasma cleaned grid. Finally, the DLS reading was obtained placing 600 µL of 2 nM MGNPs suspension in a disposable polystyrene cuvette and performing 3 measurements consisting of 11 runs (see fig.25).

2.5.7 Optimization of the platform in water

Experiments with different pH

Three different acetate buffers at a concentration of 14 mM were prepared by changing the ratio between acid (acetic acid) and base (sodium acetate), obtaining pH 4.5, 5, and 5.5.

20 µL of MGNPs at a concentration of 0.5 nM ($A_{LSPR} = 0.8$, $\varepsilon = 16.87 \times 10^9$ $M^{-1}cm^{-1}$) were incubated with 20 µL KBr 50 mM and 20 µL H_2O_2 2.5 mM in the three buffered solutions previously prepared. Ctrl was obtained in absence of H_2O_2 (replaced by water). The analysis was performed using a Tecan plate reader at room temperature, in a 96-multiwell plate.

Experiments with different halogens

Three halogen ion solutions were prepared to test the best candidate for the reshaping process. Their concentrations were independently tuned since they present different reactivity, hence, using them at the same concentration did not allow for a comparison of their activities. KCl was prepared at 500 mM. KBr at 50 mM and KI at 5 µM. 20 µL of MGNPs at a concentration of 0.5 nM ($A_{LSPR} = 0.8$, $\varepsilon = 16.87 \times 10^9$ $M^{-1}cm^{-1}$) were incubated with 140 µL H_2O_2 2 mM, 20 µL of acetate buffer pH= 5, 100 mM, and the three halogen solutions previously prepared.

Experiments of hydrogen peroxide detection

H_2O_2 was prepared at different concentrations: 0, 0.71, 2.14, 3.57, and 4.29 mM. 20 µL of MGNPs at a concentration of 0.5 nM ($A_{LSPR} = 0.8$, $\varepsilon = 16.87 \times 10^9$ $M^{-1}cm^{-1}$) were incubated with 20 µL KBr 50 mM, 20 µL of acetate buffer pH= 5, 100 mM and 140 µL H_2O_2 in the previously prepared solutions.

The analysis was performed using a Tecan plate reader at room temperature, in a 96-multiwell plate. Further experiments to evaluate the effect of H_2O_2 on the absorption intensity of MGNPs were carried out as previously described but with final H_2O_2 concentrations of 1, 3, 5, 10, and 30 mM.

Optimized conditions

20 µL of MGNPs at a concentration of 0.5 nM ($A_{LSPR} = 0.8$, $\varepsilon = 16.87 \times 10^9$ $M^{-1}cm^{-1}$) were incubated with 20 µL KBr 50 mM, 20 µL of acetate buffer pH= 5, 100 mM and 140 µL H_2O_2 with a final concentration of 3 mM.

2.5.8 Optimization of the platform in saliva

Saliva collection and handling

Saliva samples were obtained by healthy donors asking them to avoid eating, drinking, and practicing oral hygiene procedures for at least one hour before the collection. Furthermore, the sample must be unstimulated (no speaking or swallowing). A 15 mL sterile and protein low-bind tube was employed for collecting saliva and for its further storage at 4 °C. Assays were performed within 1 hour of the donation. Although the project aimed to use the proposed platform for the self-monitoring of the whole saliva, during this work for safety reasons, I preferred to filter saliva samples from different donors with a 0.2 µm methylcellulose acetate syringe filter, to remove bacteria. The same procedure was applied to saliva samples of diabetic patients provided by the San Matteo hospital of Pavia.

Reshaping in saliva

For simulated pathological conditions, saliva was spiked with aqueous glucose solutions in a concentration of 2 mM. Saliva from healthy subjects and non-supplemented was considered as the control. 20 µL of MGNPs at a concentration of 0.5 nM in acetate buffer pH= 5, 50 mM were incubated with 80 µL KBr 5 M, 20 µL of GOx (0.021 mg/mL, 3 U/mL), and 20 µL of saliva in normal or non-physiological level. The assay was performed at 37 °C and under stirring for 10 min.

TEM micrographs of the reshaping in saliva

After 10 minutes of the previously reported assay, the mixture was diluted and NPs were washed with centrifugation and resuspension in cold HEPES buffer at a concentration of 10 mM, pH=8. The as-prepared NPs were analyzed by TEM microscope and from the capture micrographs, I performed a dimensional analysis measuring the core diameter (N=1400), length of tips (N=1700), and the total number of NPs, making a comparison between controls and supplemented saliva. All samples are normally distributed while the Mann-Whitney test confirmed the statistical significance (p-value < 0.001) of the mean sizes distribution difference.

2.5.9 Glucose dipstick assay prototype

Substrate preparation

For comparing the MGNPs deposition on different substrates, a suspension of 0.4 mL MGNPs 25 pM, $A_{LSPR} = 0.4$ in 25 mM HEPES buffer, pH= 7 was taken with a syringe which was further connected to a syringe filter holder, in a vertical position. Then, MGNPs were passed through the membrane (Ø= 13 mm) located inside the filter holder. In this way, MGNPs were uniformly distributed on the substrate. In the end, 2 mL of air was injected to remove any residual water from the system. After the deposition, the substrate was placed under vacuum for 10 minutes and then, a layer of GOx (1 U/mL) in 100 mM acetate buffer, pH=5 was placed on top of it. The final device was further dried under vacuum and, finally, stored in low humidity conditions. The functionalized membrane was cut in circular pieces of 3 mm of diameter with a biopsy puncher before the performance of the assay.

Glucose assay protocol

When the substrate was completely dried with all the reagents immobilized on it, the assay on saliva was performed by placing 50 µL of a mixture containing native saliva and saliva supplemented with 1.5 or 3 mg/dL of glucose and 5 M KBr in 10 mM acetate buffer, pH= 5. The assay was performed at 37 °C for 15 minutes but the same outcome could be also achieved at room temperature waiting for a longer time.

Assay reliability and validation

The tested sample was first analyzed in their real glucose content using a high-sensitivity glucose assay kit which was chosen as the standard reference technique.

For calculating the colorimetric changes of the proposed device, six samples of healthy donors, containing a glucose concentration < 2 mg/dL were collected. Glucose level was normalized by adding glucose solution to reach a final concentration of 2.5, 4, and 6 mg/dL.

The reshaping process occurred in 15 minutes. After this time, RGB coordinates were recorded using ColorGrab (a smartphone app). The ΔRGB was calculated following the formula below:

$$\Delta RGB = \sqrt{(R_{t1} - R_{t0})^2 + (G_{t1} - G_{t0})^2 + (B_{t1} - B_{t0})^2}$$

The ΔRGB variability, related to 2.5, 4, and 6 mg/dL was plotted, allowing to identify the assay threshold. A ΔRGB> 30 (± 10) corresponded to a glucose concentration ≥ 4 (± 0.5) mg/dL, associated with a visible color change; while with glucose concentration below 2 mg/dL, the relative ΔRGB was < 15 (± 5).

Twenty saliva samples, eight from healthy subjects and twelve from diabetic subjects) were tested with a glucose assay kit and then, analyzed with the proposed colorimetric platform to perform a small clinical trial.

Assay reproducibly and limit of detection

The reproducibility assay was performed using five independently produced assays, prepared with the same protocol. These devices were treated with non-supplemented saliva samples and saliva supplemented with glucose concentrations ≥ 4 (± 0.5) mg/dL. RGB coordinates were collected to numerically identify the color change. The ΔRGB obtained at different glucose concentrations were used for establishing the LoD, calculated following the formula below:

$X_{LOD} = 3.3 * SD_{pseudo\text{-}blank}/b$

Where X_{LOD} is the limit of detection, $SD_{pseudo\text{-}blank}$ is the standard deviation for the control and b is the angular coefficient obtained from the analytical curve.
Subsequently, LOD was calculated from six saliva samples of different donors presenting a glucose concentration < 2 mg/dL and it was established at 1.4 mg/dL.

2.6 Conclusions

The proposed glucose sensing platform exploited a particular nanoscale architecture of MGNPs characterized by sensitive and remarkable plasmonic properties. The detection mechanism relied on a reshaping approach that combined the oxidation of gold atoms on the NP surface and their rearrangement on the surface concavities, leading to a morphological change into a spherical shape, followed by a spectral absorption shift and a negligible OD loss. This strategy could be exploitable to assess hyperglycemia with a colorimetric and naked-eye approach.

Interestingly the reshaping platform showed increased solidity and sensitivity when applied in the saliva medium thanks to the presence of the biomolecular corona which acted as a stabilizer, protecting the NP surface in absence of glucose. Moreover, the protein corona promoted reshaping and discouraged the etching phenomenon since proteins participated in the oxidation/reduction and rearrangement of gold atoms on the NP surface.

Furthermore, this sensing strategy was successfully transferred on a solid substrate allowing for the development of a dipstick prototype with all the reagents deposited on it. The as-prepared device showed superior stability compared with the colloidal suspension of MGNPs, which normally lose the morphological and plasmonic properties over time. Up to 6 months, the on-substrate assay showed reproducible results confirming the preservation of all the reagents on it.

This device prototype was tested with saliva samples of healthy donors, supplemented with glucose solutions to reach the pathological threshold ($\geq$ 4 mg/dL) and RGB coordinates were collected to numerically quantify the color change. After 15 minutes of the test, a clear ON/OFF outcome was achieved which is in accordance with the established ΔRGB ranges. ΔRGB values were further used to calculate the LoD of the assay, which was 1.4 mg/dL.

The assay was finally validated on twenty clinical samples, showing great reliability, and paving the way for the realization of a dipstick-like prototype for non-invasive self-monitoring of glycemia.

In conclusion, it should be noticed that this platform could be adapted to the detection of several other prognostic analytes whose metabolic pathway involves an oxidase enzyme, capable to form H_2O_2, proving to be a highly versatile and useful tool for the early diagnosis of pathological diseases.

CHAPTER 3

PAPER-BASED MULTIPLEXED COLORIMETRIC DEVICE FOR THE SIMULTANEOUS DETECTION OF SALIVARY BIOMARKERS

3.1 An overview of POCT

This chapter can be considered a natural evolution of the previous one since it presents an improvement in the proposed dipstick prototype, maintaining the aim of early detecting pathological diseases.

Point-of-care testing (POCT) refers to an assay performed near the patient, which provides immediate quantitative (like the electrochemical glucose monitor), semi-quantitative (like the urine strips), or qualitative (like the COVID-19 antigen test) information about the individual's condition (see fig.39), enabling timely treatment, or encouraging other prognostic tests. POCT can also lead to enhanced economic outcomes by reducing the number of clinical visits, unnecessary hospital admissions, and the use of staff and equipment, and by improving quality of life[104]. The global market of POCT is expected to reach USD 72.0 billion by 2027 and this enormous growth can be attributed both to an increased prevalence of respiratory diseases (such as COVID-19 and influenza) across the globe and to the improved access to POC through online platforms. POCT is also widely diffused in China and India where the number of chronic and infectious diseases among the large population is enormously increasing.

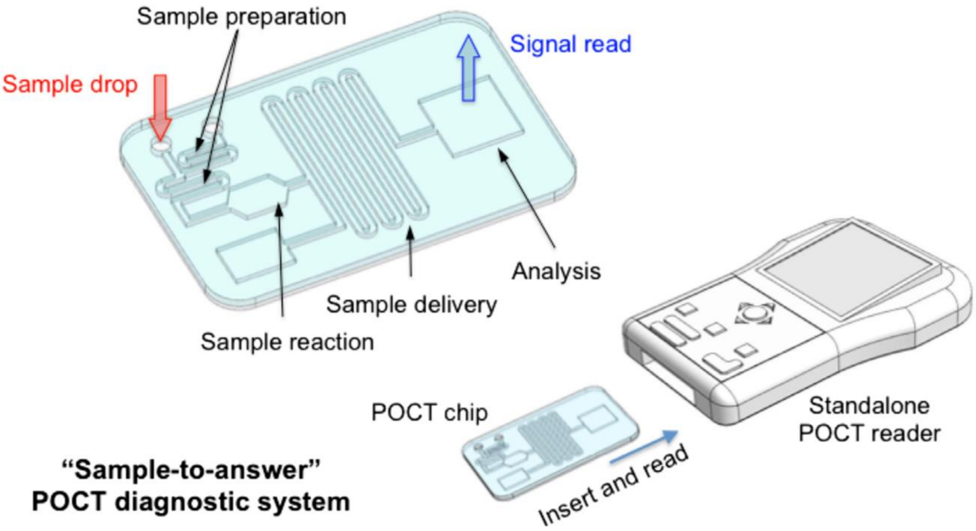
Sample preparation
Signal read
Sample drop
Analysis
Sample delivery
Sample reaction
POCT chip
Standalone
POCT reader
"Sample-to-answer"
POCT diagnostic system
Insert and read

Figure 39. Schematic illustration of a POCT system characterized by a rapid signal read-out (sample-to-answer property)[5].

In this framework, the i-STAT system represents a remarkable goal in the global POC community (fig.40). I-STAT, from Abbott, is a portable and easy-to-use blood analyzer that operates with test cartridges. This system provides patients with diagnostic information generally related to a combination of different targets to suit a wide range of clinical needs. I-STAT gives a 2-minute response as well as it can be connected to data management systems which allow to better handle test results.

Figure 40. i-STAT from Abbott.

A wide number of targets can be detected using POC devices such as small molecules, where glucose electrochemical sensor represents a milestone, proteins like HIV antibodies, cardiac and cancer biomarkers, and cell count which provides information about severe conditions like anemia[105].

3.1.1 Paper-based POCT

Emerging technologies in POCT includes paper-based assays. Paper presents numerous advantageous features such as its low cost, the possibility to exploit its capillary for moving the sample, and to be easily folded to fabricate 2D or 3D patterns[106–109]. Conventional substrates employed to realize paper-based POCT are filter paper, nitrocellulose, paper/polymers, and paper/nanomaterials composites, characterized by defined porosity and surface chemistry, which must be considered in the realization of the diagnostic tool.

3.1.2 Microfluidic paper-based POCT

Among paper-based formats, the most promising are lateral flow assays, dipstick assays, and microfluidic paper-based analytical devices (μPADs). The latter has been extensively investigated due to the low sample and reagent volume required, high capability of integration, and rapid reaction from small feature sizes[5]. Furthermore, µPAD requires a very short reaction time and shows enormous advantages in areas with scarce medical resources. The incorporation of microfluidics in POC devices allows to create those portable systems which can integrate sample preparation, dilution, mixing, chemical reaction, and detection[7].

The physical-chemical properties of cellulose paper make it extremely suited for application to microfluidics. Patterning paper is the key factor in the development of µPAD since liquid, exploiting the capillary force, must be confined inside hydrophilic microchannels separated by hydrophobic walls, enabling a controlled flow of the biological/analytical fluid under testing, without requiring an external pump. In addition, paper presents a large surface and a chemical composition that enable the simple immobilization of all the reagents[110].

3.1.3 CO_2 laser cutting fabrication technique

The hydrophilic pathway and hydrophobic walls can be obtained through a variety of methods such as photolithography[111], oxygen plasma[112], plotting[113], wax printing[114], inject printing[115], and CO_2 laser cutting[116]. The latter technique involves the design of the pattern in common drawing software like CorelDRAW or AutoCAD and the precise setting of laser beam speed and power. CO_2 laser cutting presents several advantages compared with the other reported techniques, allowing for very rapid creation of the pattern in a single process and with high resolution, reducing the costs and avoiding additional steps like melting and ink formulation[14,116].

3.2 Multiplexed analysis

Another huge advantage of patterning paper is the possibility to physically separate samples and reagents into multiple channels, enabling to perform different assays in one single microfluidic device. Multiplexed analysis can save reagents, time, cost, and labor, whilst giving a more comprehensive and complete evaluation result for a single sample[16,17,117–121]. A µPAD for the quantitative analysis of different electrolytes in tear fluid, useful for dry eye diagnosis, has been recently developed. The system exploits the microfluidic pattern of the device to distribute the tear sample into four separated regions, functionalized with fluorescent probes. Each sensing zone is composed of a fluorescent chelating agent which forms stable complexes with cations by ion-dipole interaction, inducing a conformational and electronic change in the fluorophore and a variation of the fluorescence intensity. In this way, the µPAD can detect Na^+, K^+ Ca^{2+}, and pH, simultaneously. The quantitative analysis is achieved by placing the µPAD in a portable readout device composed of different LEDs for the fluorescence excitation and by digitally processing the captured smartphone image(see fig.41)[122].

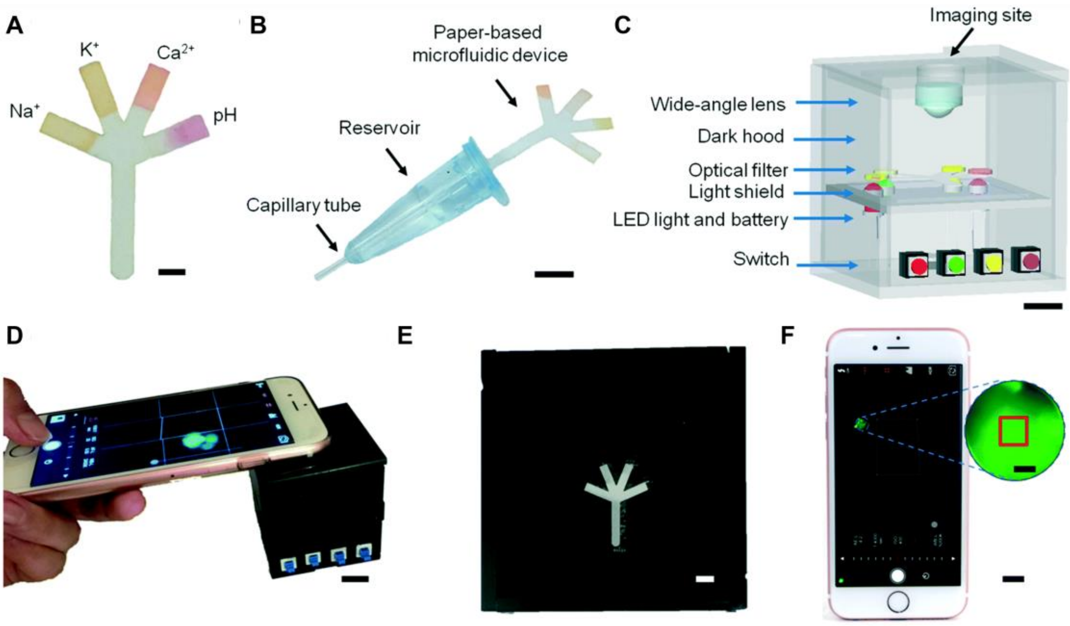

Figure 41. A) Schematic illustration of the µPAD for the analysis of electrolytes in tear fluids; B) Sample collection and assay procedure; C) Schematization of the portable device; D) Capturing of the smartphone image; E) Interlayer groove used to place the µPAD; F) Smartphone application to measure the fluorescence[122].

3.3 Colorimetric paper-based POCT

The widespread diffusion of communication technology like smartphones, scanners, and digital cameras integrated with image processing software has promoted the development of colorimetric assays, characterized by a qualitative and, quite often, a quantitative analysis of the signal intensity. The combination of µPAD with these visual systems has provided affordable, low-cost, and miniaturized tools that have been used, for example, for the detection of trace amounts of contaminants in water. In the work published by Jarujamrus et al., the smartphone was exploited as a colorimetric analyzer on µPAD for the determination of Hg^{2+} in water samples in resource-limited settings. After the development of an android application based on the RGB color model and the design of a novel µPAD with a housing light controlling system, they realized a reliable system for unskilled end-users, adaptable on different Android smartphones[123].

µPADs for optical detection (colorimetry and luminescence) are generally based on chromogenic reagents; for example, Zincon, dimethylglyoxime, diethyldithiocarbamate, and diphenylcarbazide, have been used for the multiplexed detection of heavy metals in water (fig.42A)[124]. However, the LSPR property of nanostructured materials, in particular of metal NPs like Au and Ag, gives rise to remarkable absorption phenomena, strictly dependent on the size, shape, and composition of the NP and widely exploitable for colorimetric assays in µPADs[125]. NPs indeed, compared to chromogenic probes, provide enhanced sensitivity and improved detection limits. Plasmonic NPs present increased stability and higher extinction coefficients[92]. Furthermore, thanks to their compatibility with different materials, they can be easily immobilized on cellulose substrates[126].

The µPAD developed by Chang et al. for the detection of Hg^{2+}, for example, is based on thymine-Hg(II)-thymine coordination chemistry in presence of oligonucleotide sequences attached to AuNPs. The strategy relies on the color change from red to purple and, finally, blue based on the degree of NPs aggregation (fig.42B). The achieved LoD was 50 nM, proving to be sensitive and suitable for the on-site mercury pollution monitoring[127].

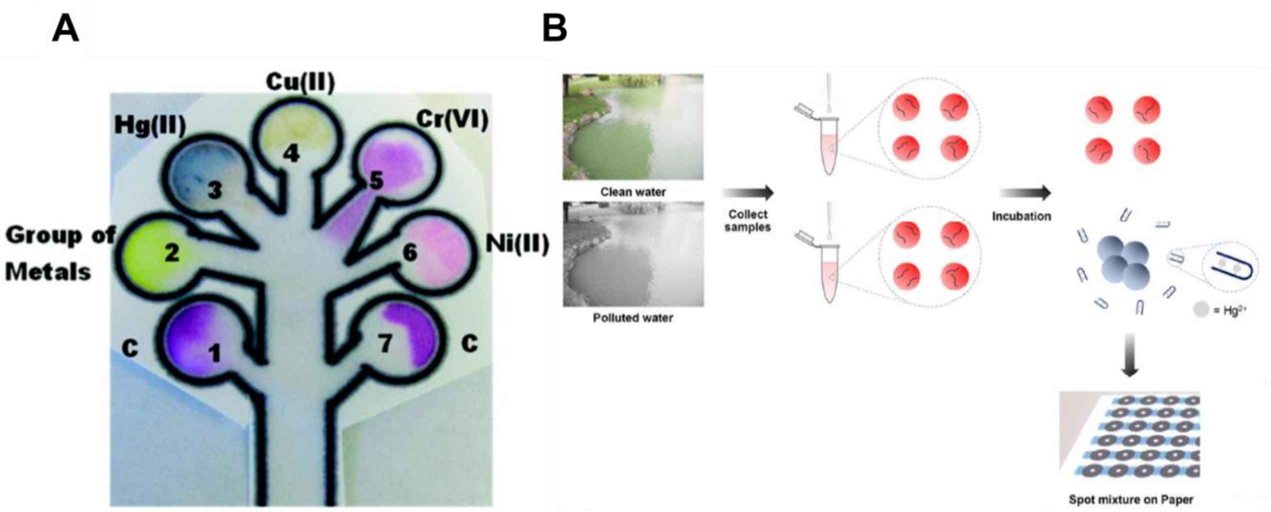

Figure 42. A) Colorimetric µPAD for the detection of heavy metals based on organic probes[124]; B) Sensing strategy of Hg (II) detection based on AuNPs[127].

Moreover, NPs can be easily adapted for the colorimetric detection of biomarkers thanks to the possibility to boost the device performance, especially in terms of sensitivity and long-term stability at ambient conditions, increasing the diagnostic potential of µPAD. AuNPs, for example, present tunable affinity toward different organic compounds and are characterized by low costs, and simple production and manipulation[77,128–131].

Due to the large surface-to-volume ratio, which enables to maximize the binding with the target, NPs can be employed in µPAD for the detection of biomarkers in biological matrices different from blood, where their concentrations are typically 1 or 2 orders of magnitude less[50,132–140]. Non-invasive fluids like urine, saliva, and tears can be collected in large amounts without pain and avoiding the risk of bloodborne pathogens transmission.

Plasmonic NPs-based µPAD can be of high interest for self-monitoring prognostic biomarkers in non-invasive fluids enabling the early monitoring and preventing the occurrence of pathological conditions associated with abnormal levels of these biomarkers like diabetes, cardiovascular diseases, retinopathy, or nephropathy.

3.4 Our strategy: a multiplexed paper-based device for colorimetric detection of salivary biomarkers

With these premises this work aims to realize a monolithic and fully integrated paper-based device for the simultaneous colorimetric detection of three model biomarkers in saliva, exploiting the plasmonic properties of MGNPs that were presented in Chapter 2. The colorimetric signal proportional to the targets' concentration can be visualized both by the naked-eye and through a smartphone camera, recording RGB coordinates which enable a semiquantitative detection[141].

To prove the multiplexing ability of the proposed device, I selected three significant target analytes (glucose, cholesterol, and lactate) which are all present in saliva at different concentrations. They have been chosen for their clinical impact on human health(fig.43); however, it was only a proof-of-concept demonstration since the platform can be easily extended to a variety of other biomarkers.

3.4.1 Target biomarkers and their metabolic role

The importance of monitoring glucose for diabetes management has been widely discussed in the previous chapter (fig.43A)[102]. But other than this, cholesterol and lactate are model targets of clinical relevance, which play important roles in metabolic processes.

Cholesterol belongs to the family of lipids, a class of biological insoluble molecules. Abnormal levels of cholesterol in plasma are related to hypercholesterolemia and consequent xanthomas, arcus corneae, and coronary heart disease (fig.43B). Familiar hypercholesterolemia is a largely diffused disease that could remain undiagnosed until a catastrophic cardiovascular event[142]. For instance, early detection of abnormal cholesterol concentration is highly required. Analysis of cholesterol levels is currently performed through a blood test and the available analytical techniques include the Abell-Kendall protocol which involves saponification, extraction and color development, fluorometric-enzymatic assays based on cholesterol oxidase-coupled reaction, and analytical instrumentation approaches such as gas and liquid chromatography[143]. The cholesterol test can be also carried out through two POC tests: Cholestech LDX® System and Professional CardioChek PA. Both of them are based on fingerpicking blood sampling and a reader[144]. Measuring cholesterol in saliva could represent a valid alternative for overcoming the issues related to blood sampling. Correlation between serum and salivary lipid profile has been analyzed by Singh et coworkers founding that there is a moderate level of correlation between the two biological fluids, with an increase of the salivary mean value as the serum level rises. They have concluded that saliva can be used as a non-invasive diagnostic tool for assessing cholesterol[145].

Lactate is the natural product of our body from carbohydrates metabolism when the energy demand is high and the oxygen availability is low, such as during intense physical exercises. Glucose, indeed, can be metabolized during glycolysis forming pyruvate, which, in turn, can be used for aerobic and anaerobic energy production (fig.43C). The first occurs when oxygen is largely available and it leads to the production of ATP, while the second forms lactate. Lactate is then released in the blood and is further reconverted in glucose in the liver. However, this molecule carries a proton that can decrease the pH of the blood, compromising body functionalities both in energy production and muscle contraction. This phenomenon leads to muscle fatigue. Blood lactate during exercises rises gradually up to the so-called anaerobic threshold and after this level, its concentration exponentially increases. Testing protocols to determine lactate threshold are highly required in the sport since it is an indicator of running fitness and endurance performance[146]. An athlete can measure his lactate levels over time to predict its performance and to target specific adaptations for the body to make[147]. Lactate is commonly measured with a very expensive laboratory testing which relies on the collection of blood samples during an exercise until exhaustion. A non-invasive, rapid, and low-cost POC device is highly required for continuous health monitoring and to evaluate improvements in the athlete's personal aerobic base. Moreover, lactate has been reported in salivary secretions and its concentration during physical exercises has been demonstrated to rise up to 4 mM, with an anaerobic threshold of 2 mM[148].

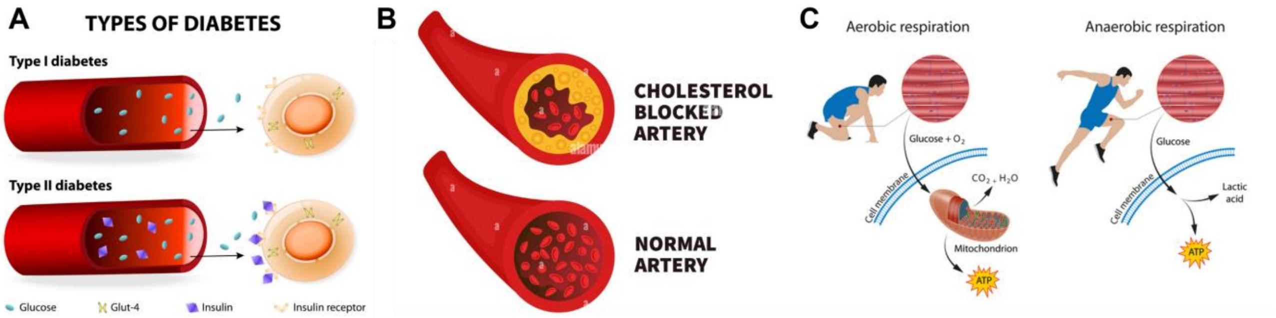
A
TYPES OF DIABETES
Type I diabetes
Type II diabetes
Glucose
Glut-4
Insulin
Insulin receptor
B
CHOLESTEROL BLOCKED ARTERY
NORMAL ARTERY
C
Aerobic respiration
Anaerobic respiration
Glucose + O_2
Cell membrane
CO_2 + H_2O
Mitochondrion
ATP
Glucose
Cell membrane
Lactic acid
ATP

Figure 43. Schematic illustrations of the target biomarkers of the proposed µPAD.

3.4.2 Detection strategy: reshaping process

The sensing strategy I exploited for the detection of these biomarkers is the reshaping of MGNPs, described in detail in chapter 2 and illustrated in fig.44. Briefly, glucose, cholesterol, and lactate were oxidized by glucose oxidase (GOx), cholesterol oxidase (ChOx) and lactate oxidase (LOx) respectively, forming H_2O_2. This byproduct of the target oxidation, in presence of the halogen, produced potent etchants species, which, in turn, oxidized Au atoms on the NP surface, leading to the morphological change from multibranched NP to spherical NP, thus promoting a color shift from blue to pink. As can be seen in fig.44C, the process did not involve optical density loss due to the redistribution of Au atoms on the NP concavities and the reaction occurred in a few minutes thanks to the presence of the halogen which boosted the oxidation process.

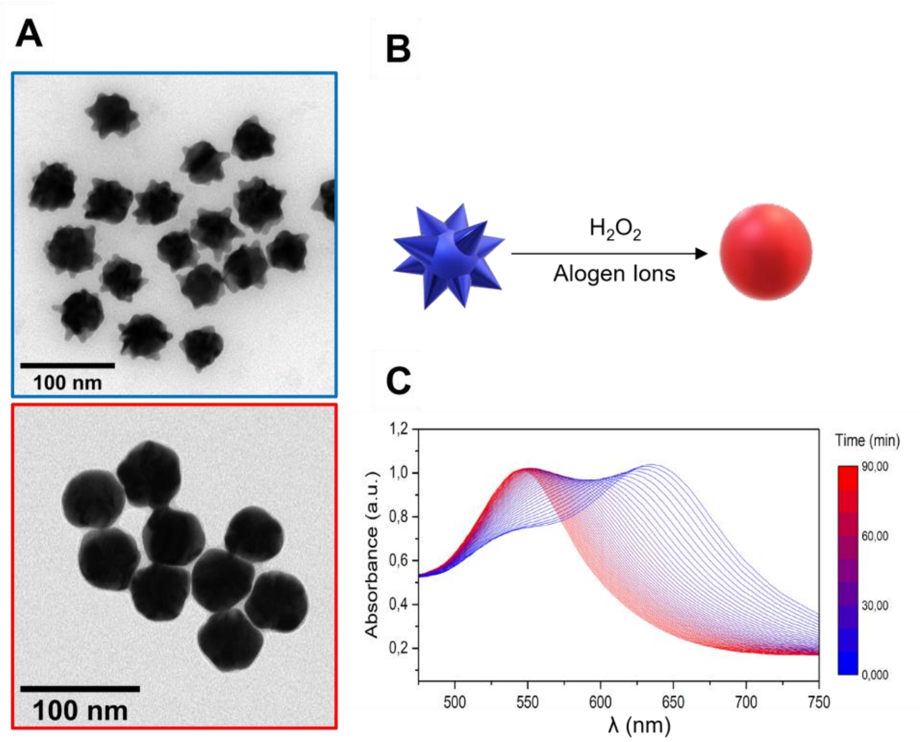

Figure 44. A) TEM micrographs of the MGNPs involved in the multiplexed detection of glucose, cholesterol, and lactate before (blue) and after (red) the reshaping process; B) Schematic illustration of the mechanism involved in the reshaping; C) evolution spectra over time of the reshaping process.

The evolution of the proposed µPAD compared with the dipstick prototype presented in the previous chapter relied on the incorporation of microfluidics on the paper-based device for the realization of a monolithic and fully integrated platform which allowed for the multiplexing analysis of three prognostic biomarkers upon deposition of a single drop of saliva.

3.5 Results and discussions

3.5.1 Device configuration and working mechanism

The schematic illustration of the µPAD for the simultaneous detection of glucose, cholesterol, and lactate in saliva is illustrated in fig.45. Specifically, I selected chromatographic filter paper grade 1 as the substrate for the realization of the monolithic and fully integrated µPAD and I designed the structure of my device using commercially available drawing software (AutoCAD). The final pattern was characterized by a main central area (sample zone) with a diameter of 7 mm where the saliva sample was placed, three round sensing areas of 7 mm functionalized with MGNPs and the oxidase enzymes, and three microfluidic channels between deposition and detection zones with a final length of 14 mm. In the middle of the branches, I placed three round areas of 3.5 mm, called pretreatment zones, that I functionalized with the halogen solution, specifically sodium iodide (NaI). Each detection zone was devoted to the detection of a singular biomarker; thus, each pretreatment zone was treated with a precise halogen and MGNP concentrations, and the specific enzyme units were deposited in the sensing zone.

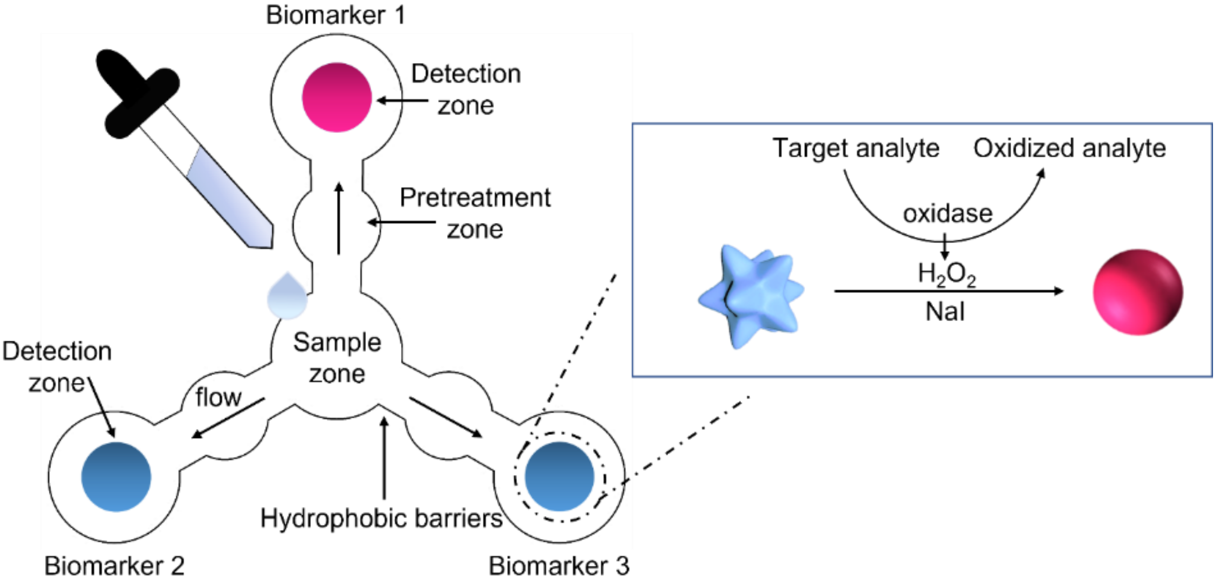

Figure 45. Schematic illustration of the proposed µPAD for the simultaneous detection of glucose, cholesterol, and lactate in saliva and the detection strategy involved in the target-induced reshaping of MGNPs.

The assay was performed by dropping a few microliters of saliva in the sample zone and by letting it flow through the microfluidic channels exploiting the capillary forces. Passing through the pretreatment zones, saliva was mixed with NaI, and the as-formed solution reached the MGNPs in the detection zone. As I previously mentioned, the sensing strategy relied on the reshaping of MGNPs, characterized by the specific morphology shown in fig.44A (blue) and an LSPR peak at 648 nm which corresponds to a blue color. The target oxidation by the specific enzyme, promoted a morphological change into spherical NPs, inducing a color shift from blue to pink of the colloidal suspension. For this specific application, with respect to the work I illustrated in chapter 2, I replaced Br- with I- since iodide halogen allowed for a wider and faster reshaping process (see fig.28), necessary for a rapid response of the POC device. I confirmed the target-induced reshaping process, incubating MGNPs with saliva supplemented with glucose for simulating a hyperglycemic condition (glucose was chosen as the model biomarker for displaying the reshaping process) (fig.46).

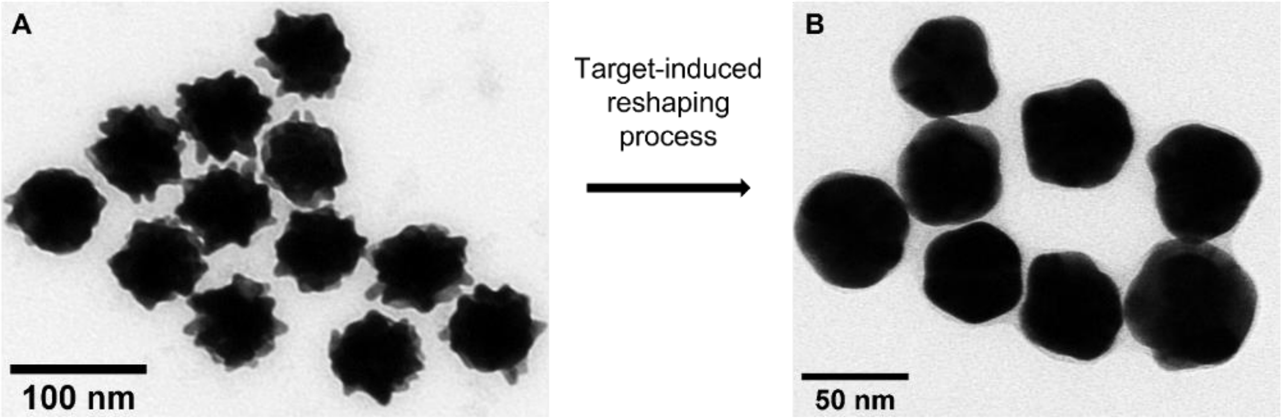

Figure 46. Glucose-induced reshaping process.

The reshaping process was finely optimized in the ratio between MGNPs, oxidases, and halogen to respond in the physiological range of concentration of the three proposed targets and to give a predictive color change in case of pathological conditions.

Concerning the realization of the µPAD, I chose the CO_2 laser ablation technique, due to its rapidity, low-cost, single-step process, and the possibility to parallelize the procedure for scalability to medium-level production. I optimized the two main settings of the system concerning the power and the speed amount to realize 12 well-defined devices in less than 1 minute, whilst avoiding burning edges (typical of a too-low speed or an excessive power) or ill-defined boundaries (occurring when low power is set). Fig.47 shows a paper sheet after CO_2 laser cutting treatment for the realization of the µPAD. This result was achieved by setting the power to 12 W and the speed amount to 50 mm/s. One single device was obtained in less than 5 seconds, maintaining high cutting precision and lateral resolution of 1 µm, confirming the enormous potential of this technique.

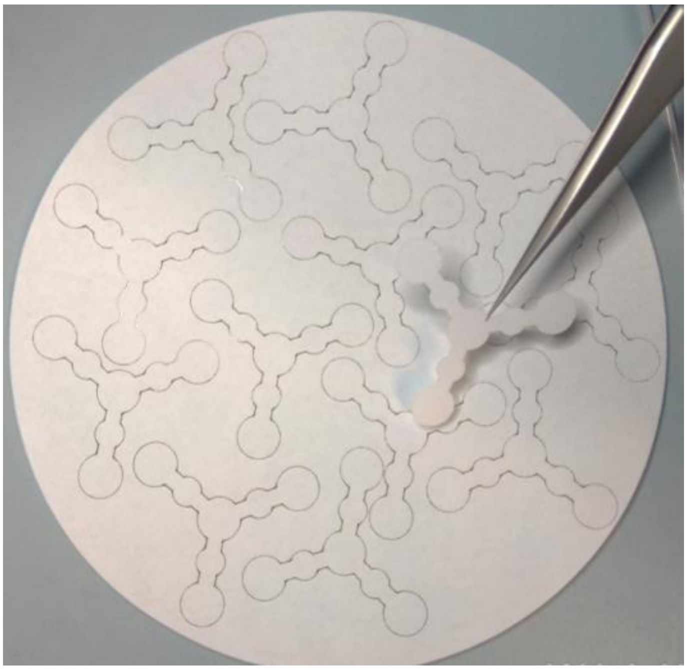

Figure 47. A paper sheet after the CO_2 laser cutting treatment.

After the realization of the three-branch device, I functionalized each zone with the specific reagents at the proper concentration. In the three sensing areas, I placed the same concentration of MGNPs (OD=12), while GOx, LOx, and ChOx were tuned for the specific assay. In the same way, pretreatment zones were functionalized independently, as a function of the specific biomarker to be detected and its range of interest. The reshaping process was finely tuned to give a predictive colorimetric shift in less than 10 minutes for the three biomarkers at their salivary concentration. Particularly, referring to the literature, I established three pathological thresholds above which the assay should give an ON/OFF signal: for salivary glucose the non-physiological condition occurs when the concentration is above 14 µM (which corresponds to 130 mg/dL in the blood), for cholesterol > 5.2 µM (> 200 mg/dL in the blood), and for lactate > 2 mM (> 4 mM in the blood)[102,145,148]. Moreover, for the lactate and glucose assay, I proposed a semi-quantitative assay. Indeed, their concentrations can reach an additional non-physiological threshold. For the glucose assay, this second level is an index of severe hyperglycemia corresponding to a blood glucose level above 200 mg/dL and 28 µM in saliva, while for lactate it corresponds to the “maximal lactate steady state” (> 4 mM in saliva) and it gives further important information about athlete’s cardiovascular and pulmonary health[149].

3.5.2 Assay optimization

For the realization of a suitable µPAD for the detection of the proposed salivary biomarkers, I had to perform several optimizations related to the reagents' volumes and concentrations and to the device configuration.

First, I analyzed the sample flow to establish the optimum volume required for a homogeneous distribution on the three branches. With this aim, I tested 20-30-40-50 µL of saliva mixed with a red dye to follow the flow evolution over time. I found that 40 µL was the proper volume since it completely filled the three detection zones, with no more flowing solution (see fig.48). Moreover, an isotropic evolution of the salivary flow could be achieved in all the three branches, and in less than 10 seconds saliva reached the three detection zones, exploiting capillary forces. From the image below, it is also clear that the flow slowed down passing through the pretreatment zones since they presented higher diameter compared to the branches and, for Bernoulli's principle[150,151], the fluid's speed increases when the pressure decreases, according to the energy conservation principle.

A further improvement in the optimization of the flow was the introduction of a round piece (7 mm) of Fusion 5 that I placed in the sample deposition zone. Fusion 5 is generally employed in LFD and it provides multiple functions to the device among which acting as a sample pad, and hence, enabling a controlled release and an even flow of the sample, whilst retaining minimal volume.

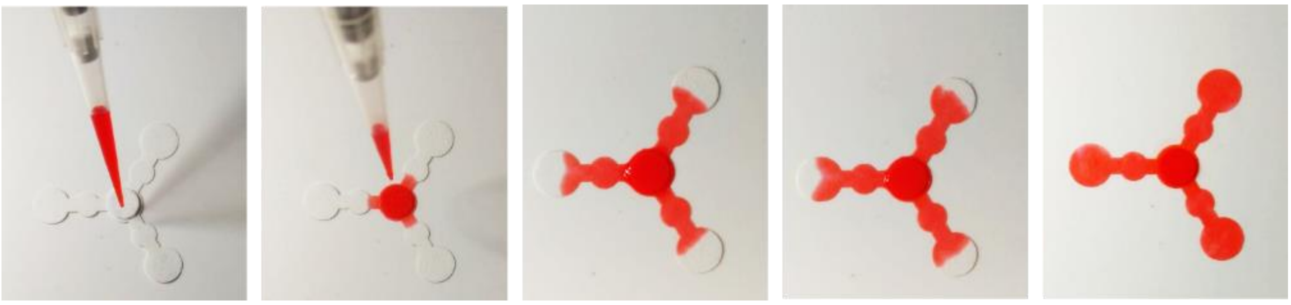

Figure 48. Evolution over time of the flow of saliva mixed with a red dye on the µPAD.

Then I moved to the optimization of the pH that I used for buffering the enzyme solutions. As I stressed in the previous chapter and as it can be seen in fig.27, an acidic pH boosted the reshaping process however it led to aspecific etching and false positive results. On the contrary, a basic solution slowed down the reaction, making the color change almost unclear after 10 minutes. For instance, for each target-induced sensing assay, I performed a systematical analysis to establish the best pH condition. Fig.49 shows the optimization I performed for the glucose assay, which I used as the model biomarker. I compared the response of the device when the enzyme was solved in phosphate buffer solutions pH=6, 7, and 8. Red hatch represents the condition that I chose (pH=7) since it gave the stronger stability of the control (device treated with non-supplemented saliva), with a minimal color-shift after 10 minutes, whilst displaying the more intense pink color when the sample (saliva supplemented with glucose concentration above the threshold) was tested. The result was confirmed even for cholesterol and lactate.

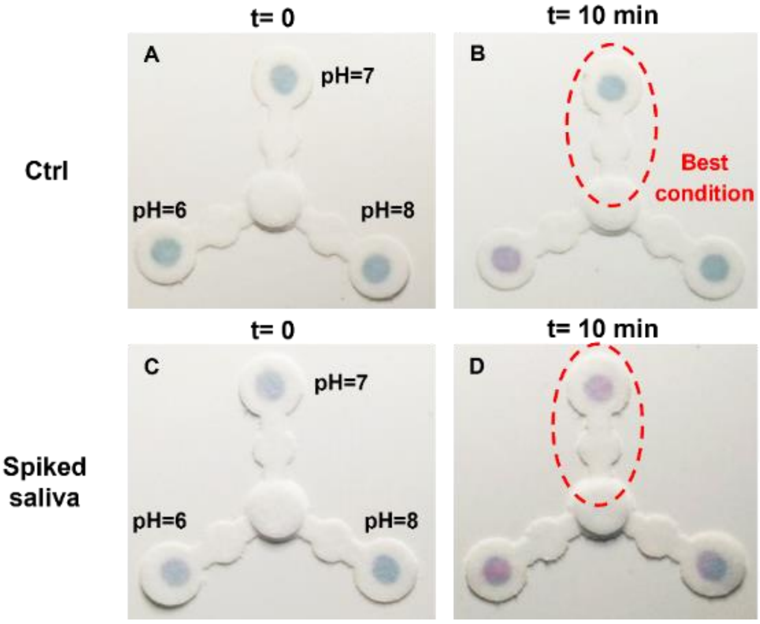

Figure 49. Optimization of pH used for enzyme solution in glucose assay.

Similarly, I optimized the pH of the buffer that I used for the NaI solution. In this case, apart from changing the pH, I tested two different buffer solutions to explore a wider pH range. In fig.50, I decided to show the optimizations I performed on lactate-induced reshaping, despite similar considerations being done for the other targets. I compared the response of the device when acetate buffer pH= 6, phosphate buffer pH= 6, and phosphate buffer pH=7 were compared. Even in this case, I selected the condition which gave the best read-out both for the control (remained blue) and for the sample (displayed vivid pink color). Acetate buffer promoted a quick LSPR shift which resulted in an aspecific etching, as can be seen in fig.50B. Phosphate buffer pH=6 was selected as the best condition for lactate assay since it allowed for a faster reshaping process in 10 minutes (fig.50D). The result was confirmed even for cholesterol and glucose.

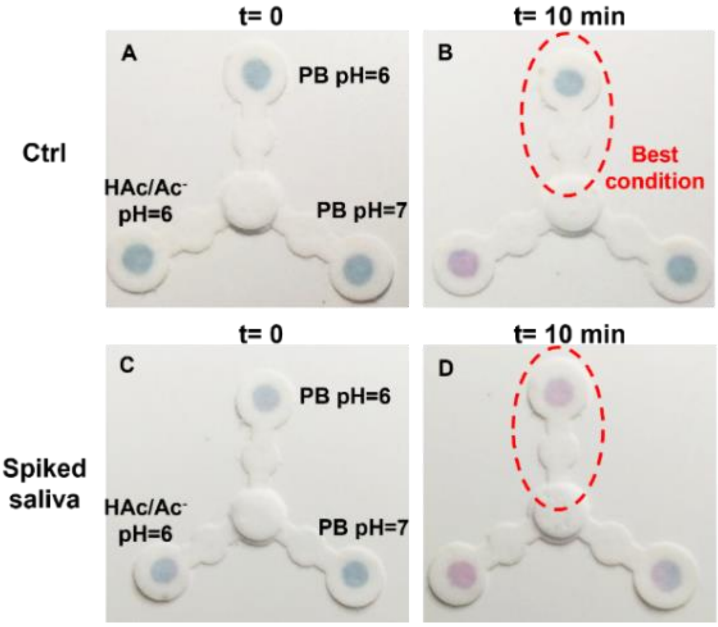
t= 0
t= 10 min
A
B
PB pH=6
Ctrl
Best condition
HAc/Ac- pH=6
PB pH=7
t= 0
t= 10 min
C
D
PB pH=6
Spiked saliva
HAc/Ac- pH=6
PB pH=7

Figure 50. Optimization of the buffer used for NaI solution in lactate assay.

Finally, I did the same considerations for the enzyme units, and I decided to show in fig.51 cholesterol-induced reshaping optimization. I tested three cholesterol oxidase concentrations namely 0.25 U, 2.5 U, and 5 U. The enzyme created on the MGNPs a protein layer that protected the surface from aspecific etching, indeed, as it is shown in fig.51B, when too low units were tested, a color shift occurred even with the control solutions. 2.5 U was selected as the best condition, according to these reflections. For glucose assay, I chose 145 U, and for lactate 0.25 U.

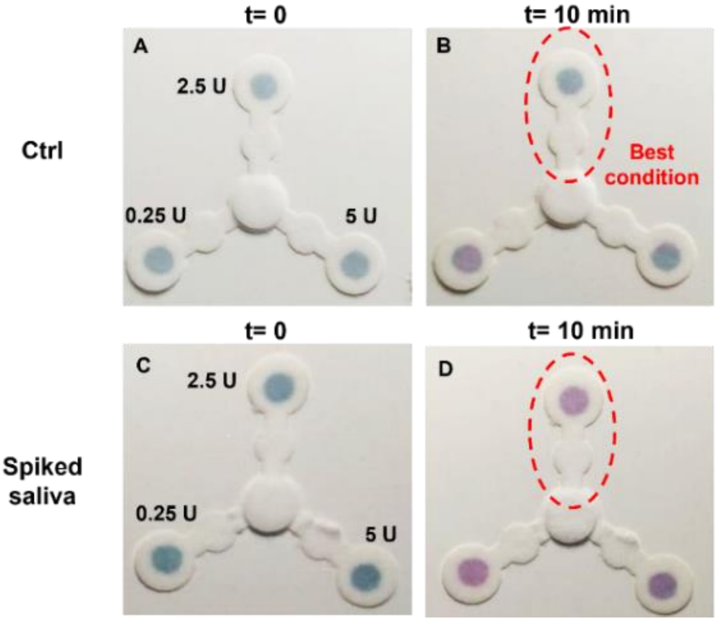
t= 0
t= 10 min
A
B
2.5 U
Ctrl
Best condition
0.25 U
5 U
t= 0
t= 10 min
C
D
2.5 U
Spiked saliva
0.25 U
5 U

Figure 51. Optimization of enzyme units for cholesterol assay.

I further optimized the concentration of the halogen for each sensing assay, singularly. For glucose, I set a concentration of 250 µM, for cholesterol 100 µM, and for lactate 150 µM.

All these tests were performed aiming to obtain a clear optical read-out in ca. 10 minutes, with an ON/OFF signal in case of concentrations above the established threshold, avoiding false positive results related to aspecific etching. As I mentioned before, for the glucose and lactate assay, my aim was to achieve a semi-quantitative result, fixing a second interesting threshold in the higher concentration range.

MGNPs concentration was finely tuned to provide a vivid color before and after the reaction. Reshaping led to a negligible OD loss, hence, I expected the same color intensity after the 10 minutes-test. For instance, I chose a starting OD=12, which I considered well distinguishable both by the naked-eye and by a smartphone camera, and I deposited 0.5 µL in the middle of the sensing zone to ensure that saliva reached the test zone homogeneously mixed with all the reagents, allowing for the uniformity of the colored spot.

3.5.3 Analytical performance

After all the optimizations, I tested the performance of the device for the detection of glucose, lactate, and cholesterol, singularly. With this aim, I functionalized the devices for the detection of a single target, and I placed a drop of native saliva and of supplemented saliva in the sample deposition zones. I repeated the experiment with 10 saliva samples collected from healthy donors. I acquired one smartphone image at the beginning of the test and one after treating the device with the sample and waiting 10 minutes for the color development. I analyzed the images with ImageJ software recording red (R) coordinates (in the RGB space) which were the most predictive of the color change. Finally, I plotted the variation in R (ΔR) obtained by comparing the end with the starting point, of the spiked samples (red) against the native saliva samples (blue) (fig.52).

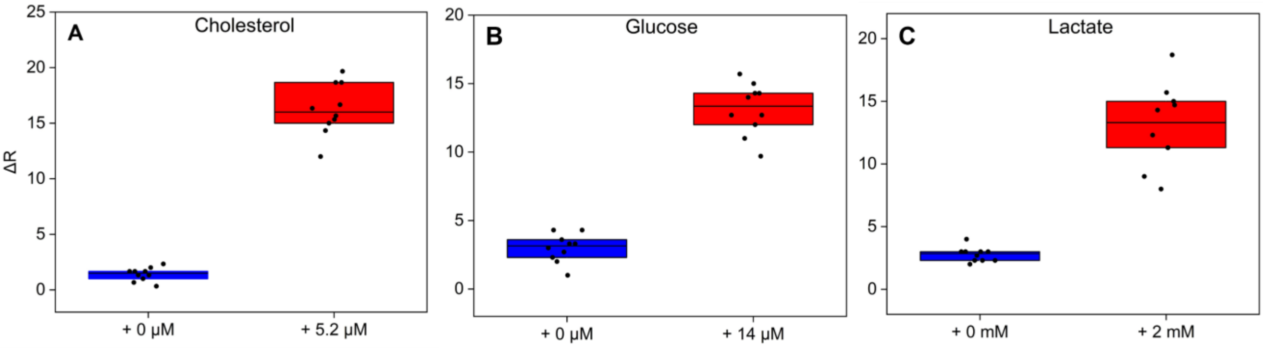

Figure 52. Analytical performance of the device obtained by plotting ΔR values of the implemented saliva (red bars) with that of native saliva (blue bars). Points represent the analyses performed on 10 saliva samples.

From the graphs in fig.52, it can be noticed that there was a remarkable difference between ΔR values of native saliva samples and those of samples containing the target concentration above the established threshold, which could be appreciable both by the naked-eye and by the smartphone camera. Although points distribution in the graphs shows that there was variability among samples collected by different individuals, I could state that an ON/OFF signal was always obtained, for all the biomarkers tested. Furthermore, false positive results were excluded since, for each assay, native saliva samples showed a negligible ΔR value (less than 5). Instead, spiked samples presented ΔR between 10 and 20 for all the targets, confirming that the colorimetric read-out was well distinguishable compared with the controls, both by R coordinates and by the naked-eye.

As I mentioned before, I was interested in fixing a second, higher threshold for glucose and lactate assays to provide a semiquantitative result for these two analytes. With this aim, as it is illustrated in fig.53, I tested the device with native saliva and saliva spiked with the concentrations of the targets corresponding to the two thresholds. I followed the colorimetric evolution over time of the detection spot, capturing images every 2 minutes and recording ΔR coordinates. As in the previous experiments, I performed the test on 10 samples collected by different donors. From the graphs, it can be noticed that there is a different kinetics between the two concentrations. Apart from the controls (no spiked saliva), which did not present appreciable color variation, confirming any false positive results, ΔR of the highest concentration started to rise after the first 4 minutes, resulting in an immediately appreciable positive result. Instead, ΔR of the first non-physiological threshold increased after 7-8 minutes, reaching at the end of the assay, a lower but still evident colorimetric shift. This result demonstrated that a specific oxidation time was required when different concentrations of the target were processed, leading to a delay in the response for lower concentrations.

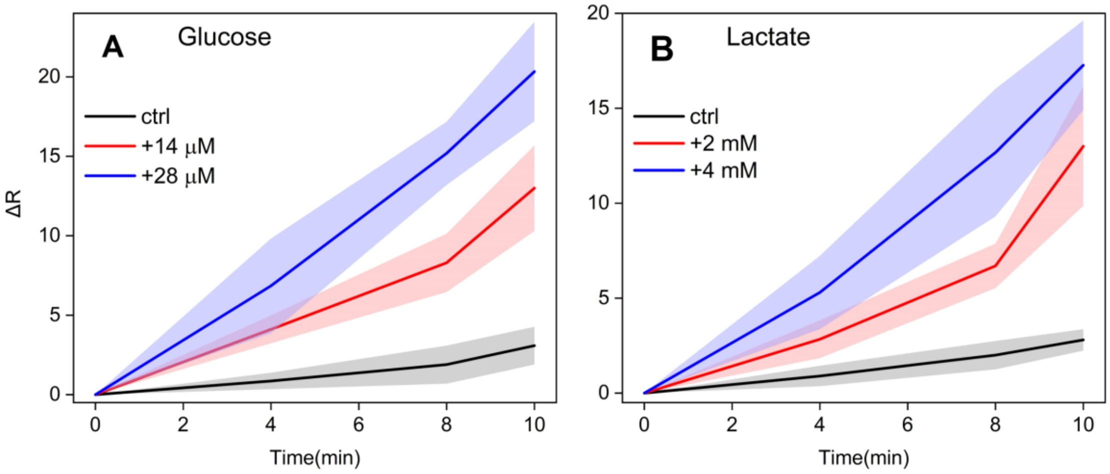

Figure 53. Evolution over time of the ΔR of native saliva (black lines), saliva spiked with the first analyte threshold (red lines), saliva spiked with the second analyte threshold (blue lines). The color band represents the standard deviation of measures performed on 10 different samples.

3.5.4 Multiplexing assay

After the evaluation of the analytical performance of the device for the detection of the biomarkers singularly, I demonstrated its multiplexing ability by performing a series of experiments with saliva containing all the three analytes.

First, I proved the absence of interference between the targets. I functionalized the three sensing areas and the respective pretreatment zones with all the reagents required for the simultaneous detection of the targets. Then, I tested on four different devices, native saliva and saliva spiked with the pathological concentration of the three analytes singularly. As it is shown in fig.54, native saliva never gave false positive results and each analyte promoted the color change of its own detecting zone, without interfering with the others, which, in turn, remained blue.

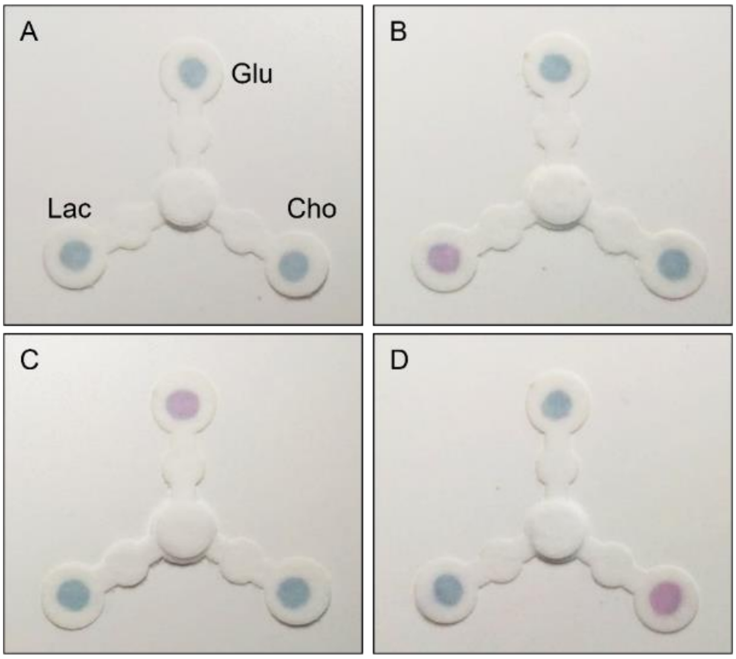

Figure 54. Images of the devices treated with native saliva (A); lactate spiked saliva (B); glucose spiked saliva (C); cholesterol spiked saliva (D).

Finally, I demonstrated the ability of my device to detect the three analytes simultaneously present in the sample. With this aim, I tested four, completely functionalized µPAD with native saliva and saliva spiked with above-threshold concentrations of one, two, and three biomarkers simultaneously (see fig.55). The result shows that the detection zones were sensitive to the specific analyte but when all the targets are simultaneously present in the sample, all the sensing areas underwent to a remarkable color change, exhibiting a vivid pink color. I could state that my µPAD can be exploitable for the multiplexing detection of different biomarkers in saliva.

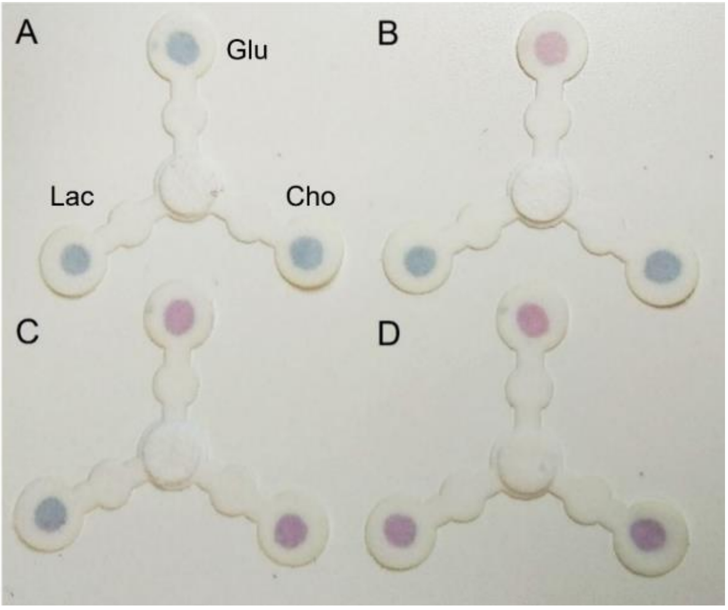

Figure 55. Images of the devices treated with native saliva (A); saliva implemented with glucose (B); saliva implemented with glucose and cholesterol (C); saliva implemented with glucose, cholesterol, and lactate (D).

3.5.5 Interference study

To evaluate the possible interference of salivary species in the glucose, cholesterol, and lactate assays, I spiked native saliva and saliva supplemented with the three targets, with aqueous solutions of sucrose, maltose, fructose, and lactose, one by one (see fig.56). This experiment aimed to determine if these compounds created some interference both in the control sample, giving false positive results and in the supplemented samples, influencing the reshaping process. Hence, I tested the devices, functionalized for the detection of only one analyte, with control and supplemented saliva, and I compared their performance (in terms of ΔR) with devices treated with the same samples spiked with the interferent. As can be seen from the graphs below, the color change was almost the same in all the samples, confirming that the interference was negligible for all the salivary compounds tested.

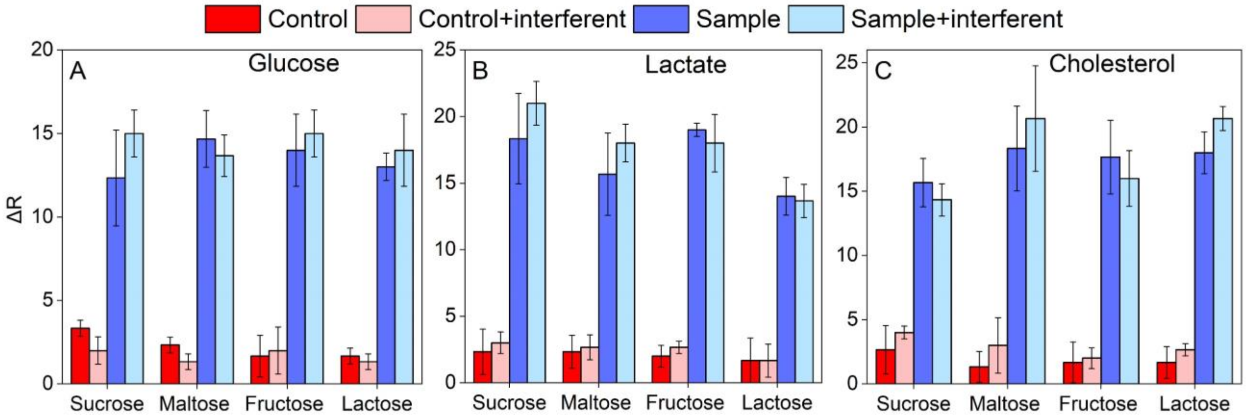

Figure 56. Graphs showing ΔR values of controls (red graph), control + interferent (pink graph), saliva supplemented with glucose (A), lactate (B), and cholesterol (C) (blue graphs), supplemented saliva + interferent (light blue graphs). Error bars represent the uncertainty from three independent measurements.

3.5.6 Development of a device prototype

In conclusion, aiming to realize a home testing prototype for the multiplexing detection of salivary biomarkers, I designed a mask using AutoCAD, which would provide my µPAD with robustness and handling. Starting from a sheet of polyvinyl chloride (PVC) adhesive film, I realized, with the CO_2 laser cutter, three holes in correspondence of the spots in the sensing areas and one hole in the sample deposition zone (fig.57A). Then, I placed my µPAD between the PVC film and an adhesive sealing film, achieving a sandwich-like structure. Finally, I proved the non-interference of the mask on the device performance, testing saliva supplemented with non-physiological concentrations of all the analytes (fig.57B, C). As it is shown in fig.57C, the mask did not hamper the multiplexing ability of the µPAD, whilst providing increased versatility and paving the way for the realization of a user-friendly POCT.

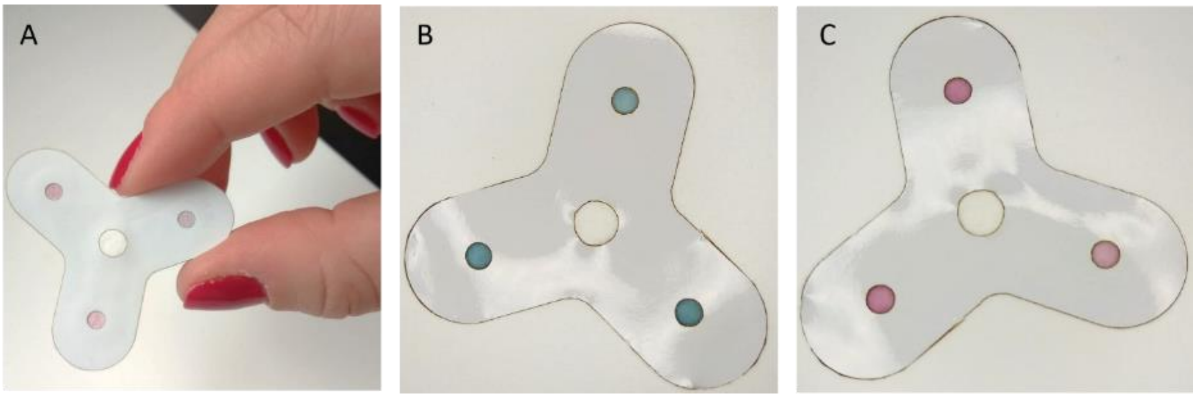

Figure 57. A) Image of the device prototype with the µPAD embedded in the patterned PVC film and a sealing film; the device prototype treated with saliva supplemented with the tree analytes at the beginning (B) and the end of test (C).

3.6 Materials and methods

3.6.1 Chemicals

Sodium iodide (NaI), D-(+)-Glucose, Glucose Oxidase from Aspergillus (Type X-S,), Sodium L-Lactate, Lactate Oxidase from Aerococcus viridians, Cholesterol, Cholesterol Oxidase from microorganisms Triton™ X-100, Sucrose, D-(+)-Maltose monohydrate, D-(−)-Fructose, D-Lactose monohydrate, Sodium phosphate monobasic, Sodium phosphate dibasic, and Whatman® qualitative filter paper (Grade 1, diam. 110 mm) were purchased from Merck-Sigma-Aldrich. MPI™ 3000 Gloss High Opacity Series (95 µM thickness) was purchased from Avery Dennison®. Whatman Fusion 5 was purchased by Cytiva. 96W PE Sealing film (adhesive, optical, Corning®) was purchased from VWR.

3.6.2 Instrumentation

Lasercut61 was used to draw microfluidic channels on paper. Dynamic Light Scattering (DLS) Malvern Panalytical, Transmission Electron Microscope JOEL JEM 1400, NanoDrop® (wavelength Accuracy ± 1 nm, absorbance accuracy 3 % at 0.74 Abs@350nm) Thermo Fisher, Ocean Optics Spectrophotometer with OCE-HDX-XR detector were used for AuNPs characterizations.

3.6.3 Synthesis of 15 nm AuNPs

The synthesis of colloidal 15nm AuNPs relied on a citrate reduction[99]. All the glassware and the magnetic stir-bar were washed with aqua regia ($HCl:HNO_3$ 3:1). 250 mL of a solution of 1 mM of $HAuCl_4$ was added in a 500 mL round-bottom flask, connected to a bulb condenser, and placed in a glycerol bath. After reaching the boiling point, 25mL of 40 mM trisodium citrate solution was added to the flask under vigorous stirring. After 15 min a red wine color appeared. At the end of the reaction, the flask was placed in an ice bath, enabling it to rapidly reach room temperature. The solution was filtered with a 0.2 µm cellulose acetate syringe filter and stored at 4°C.

3.6.4 Characterization of 15 nm AuNPs

The prepared AuNPs were characterized using UV-vis spectroscopy, TEM, and DLS. Particularly, 600 µL of the synthesized NPs with a concentration of about 2 nM were spectrophotometrically read through a disposable polystyrene cuvette. For the TEM analysis, 3 µL of 2 nM AuNPs suspension were placed on oxygen plasma cleaned grid. Finally, the DLS reading was obtained placing 600 µL of 2 nM AuNPs suspension in a disposable polystyrene cuvette and performing 3 measurements consisting of 11 runs (see fig.24).

3.6.5 Synthesis of MGNPs

The synthesis of 60nm MGNPs was performed by slightly modified Maiorano-Pompa protocol[152] with a seeded growth approach. All the glassware and the magnetic stir-bar were washed with aqua regia (HCl:HNO_3 3:1). Ratio between the reagents was finely tuned to obtain MGNPs characterized by several small tips and an LSPR peak around 650nm. Briefly, in a 500mL round-bottom flask, were added 250 mL of 50 mM HEPES solution, pH=7, under vigorous stirring. Then, 6.5 mL of the previously prepared seeds at a concentration of 1.8 nM, 0.28 mL of 100 mM $HAuCl_4$, and 0.8 mL of 100 mM of hydroxylamine sulfate were added consequently. After 15-20 minutes at room temperature, a blue color appeared. At the end of the reaction, centrifugation of the suspension was performed (4000 rcf, 25 min) to remove residual reagents excess.

3.6.6 Characterization of MGNPs

The prepared AuNPs were characterized using UV-vis spectroscopy, TEM, and DLS. Particularly, 600 µL of the synthesized MGNPs diluted to a concentration of about 2 nM in water were spectrophotometrically read through a disposable polystyrene cuvette. For the TEM analysis, 3 µL of 2 nM MGNPs suspension were placed on oxygen plasma cleaned grid. Finally, the DLS reading was obtained placing 600 µL of 2 nM MGNPs suspension in a disposable polystyrene cuvette and performing 3 measurements consisting of 11 runs (see fig.25).

3.6.7 Design and fabrication of the analytical device

The design of the µPAD was realized through AutoCAD software. I further transferred the pattern on a sheet of Whatman® qualitative filter paper (Grade 1) using the Lasercut61 which has a precision of +/- 0.1 mm and a cutting speed of 200 mm/sec. I set the power to 12 W and the speed amount to 50 mm/s, and I realized in less than 1 sec 12 well-defined devices from a paper sheet (see fig.47). The final design was characterized by a circular sample deposition zone with a diameter of 7 mm, three branches of 14 mm with a circular pretreatment zone of 3.5 mm in the middle, and three circular zones at the end of the branches characterized by a diameter of 7 mm.

3.6.8 Reshaping process

The platform was developed for the multiplexing detection of glucose, cholesterol, and lactate. The sensing strategy relied on the reshaping process, which I explained in the previous chapter. The ratio between the regents was finely tuned for each assay, while the amount of MGNPs deposited on the test zones and their OD was the same (0.5 µL, OD=12 @ 648 nm). The halogen selected to boost the reshaping of MGNPs was NaI. Used in a concentration-dependent on the specific assay (see “Assay Optimization” paragraph).

3.6.9 Assay procedure

Before performing the assay, the µPAD was functionalized with the optimized conditions for the detection of the three biomarkers. Hence, in the pretreatment zones, I placed 1.5 µL of NaI solved in sodium phosphate buffer solution, 100 mM, pH=6, at a concentration of 250 µM for glucose assay, 150 µM for lactate assay, and 150 µM for cholesterol assay. These concentrations were finely tuned according to the consideration I discussed in the "Assay Optimization" paragraph (fig.50). Then I immobilized 0.5 µL of MGNPs (OD=12 @ 648 nm) in the sensing zones and I placed a layer of the oxidase (1.5 µL) on top of the NPs. Depending on the assay, I optimized the concentrations and the pH of the phosphate buffer solution in which I solved the three enzymes (see paragraph "Assay Optimization" and fig.49 and 51): 150 U of GOx were solved in pH= 7, 100 mM, 0.25 U of LOx in pH=7, 50 mM, and 2.5 U of ChOx in pH7, 50 mM). Finally, I put the device under vacuum for 15 minutes to stably dry all the reagents. I performed the assay by dropping 40 µL of saliva (see paragraph "Assay Optimization" and fig.48) on the sample deposition zone and I let it flow through the microfluidic channels exploiting the capillary forces.

3.6.10 Data collection and analysis

At the end of the assay (10 minutes), I recorded a smartphone image of the device, standardizing the acquisition condition: the smartphone was placed on a support that guarantees the same distance during acquisition, the paper-based device was located on a white and matt photography backdrop, and illumination was provided by an external lamp. I processed the pictures through ImageJ software, recording red coordinates (R) in the RGB space of the colored spot. I performed the assays on 10 samples collected from 10 different healthy subjects and I repeated the experiments in triplicate.

3.6.11 Saliva samples preparation

The use of saliva in this study was approved by the Ethical Committee of Regione Liguria (405/2022-DB id 10787). Saliva samples were obtained by healthy donors asking them to avoid eating, drinking, and practicing oral hygiene procedures for at least one hour before the collection. Furthermore, the sample must be unstimulated (no speaking or swallowing)[153]. A 15 mL sterile and protein low-bind tube was employed for collecting saliva and for its further storage at 4 °C. Assays were performed within 1 hour of the donation. Although the aim of the project was to use the proposed platform for the self-monitoring of the whole saliva, during this work for safety reasons, I preferred to filter saliva samples from different donors with a 0.2 µm methylcellulose acetate syringe filter, to remove bacteria. Native saliva was considered a control, while for simulating non-physiological conditions I spiked samples with solutions of glucose (14 µM and 28 µM for the second, higher threshold), cholesterol (5.2 µM), and lactate (2 mM and 4 mM for the second threshold). Cholesterol stock solutions were obtained by solving the powder in Triton X-100 10% and further dilutions were made in sodium phosphate buffer 50mM, pH=7.

3.7 Conclusions

The proposed paper-based platform for the multiplexing visual detection of three salivary biomarkers was realized with a low-cost and highly efficient CO_2 laser cutting technique. It did not require multiple steps and treatments with chemical materials or organic solvents, and it produced in less than 1 minute about 12 completed devices, whilst maintaining precision and high resolution. The microfluidic pattern enabled to move the sample into three different channels, selectively functionalized for the detection of a target biomarker. The sensing strategy relied on the reshaping of MGNPs, placed as a spot in the detection zone, and covered with a layer of oxidase. In presence of a non-physiological concentration of the analyte, a clear and well-defined color change from blue to pink was appreciable, due to the oxidation of gold atoms on the NP surface which induces a morphological change into spherical NP. The presence of the halogen which was deposited in the middle of the microfluidic channel, along the sample path, further boosted the reshaping process, enabling a 10-minute reaction. The colorimetric read-out could be visualized by the naked-eye and by a smartphone image collecting R coordinates in the RGB space. Glucose, cholesterol, and lactate above the established physiological threshold were immediately visualized as an ON/OFF signal. Moreover, for glucose and lactate assays, a higher threshold was fixed since it is of high interest to know if their concentrations slightly or significantly exceed the non-physiological level and it was achieved a reliable semi-quantitative result. Interferences by other components normally present in saliva were excluded. Finally, the paper-based device was embedded in a PVC mask, realized through CO_2 laser cutting aiming to improve the versatility and the handling of the paper sheet and it proved to be a valid prototype for the home testing of salivary biomarkers.

In conclusion, it is important to stress that the three selected biomarkers were models that I used to demonstrate the feasibility to realize a multiplexed-based POCT. Indeed, lots of analytes prognostically important can be detected with a similar approach, after finely changing the oxidase enzyme and tuning the reaction conditions in terms of reagents concentration and pH. Other implementations can be achieved by morphologically modifying the pattern of the device to increase the number of microfluidic channels, enabling the detection of more than three biomarkers, whilst saving money, reagents, and costs and providing a more exhaustive clinical value of the test.

CHAPTER 4

A LATERAL FLOW DEVICE FOR POINT-OF-CARE DETECTION OF DOXORUBICIN

4.1 An overview of chemotherapy

Cancer is a severe condition caused by uncontrolled cellular growth and it is one of the primary causes of death worldwide. Cancer treatment is mainly based on surgery, radiotherapy, and chemotherapy. The use of chemotherapy drugs, which act by destroying cells or by limiting tumor proliferation, is an extremely powerful tool but presents many side effects due to the lack of selectivity. Indeed, these drugs destroy both tumor and healthy cells, leading to myelosuppression, gastrointestinal tract lesion, nausea, hair loss, and clinical resistance. Although their remarkable toxicity and the development of more selective therapy, anticancer drugs still remain widely used in the current world. Therefore, there is an enormous risk for the patients to be affected by adverse reactions; hence, analytical methods to determine these drugs are of high interest and importance. Nowadays, commonly employed techniques are liquid chromatography (LC) with a UV detector, LC-mass spectroscopy (MS), LC-fluorimetry, LC-electrochemical sensors, Raman spectroscopy, and infrared spectrometry[61].

4.2 The importance of drug monitoring in chemotherapy

Analysis of cytotoxic drugs is required as quality control for the prepared formulation before patient administration and as therapeutic drug monitoring (TDM). TDM is usually difficult to realize due to the use of combination therapies and the personalization of the drug concentration. However, it could potentially improve the clinical success of the therapy and reduce the side effects (fig.58)[154].

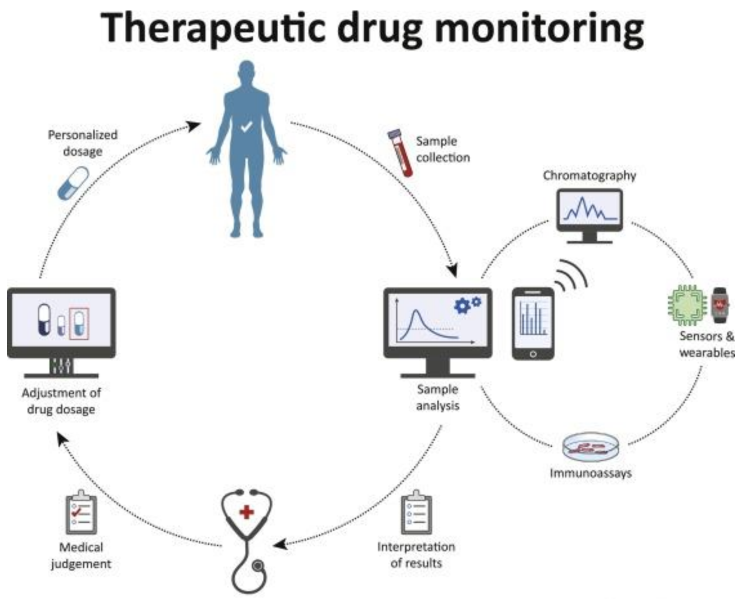
Therapeutic drug monitoring
Personalized dosage
Sample collection
Chromatography
Sensors & wearables
Adjustment of drug dosage
Sample analysis
Immunoassays
Medical judgement
Interpretation of results

Figure 58. Schematic explanation of how TMD works[154].

4.3 Healthcare workers’ exposure to chemotherapeutic drugs

Another important issue is related to the exposure of healthcare workers in the occupational environment where the drug is administered. Several studies have reported that exposure to cytotoxic drugs is associated with potential cancer risk[155]. Extensive safety precautions have been taken to prevent healthcare professionals’ exposure such as guidelines, protocols, biological cabinets, and personal protective equipment. Despite such measurements, there is still a risk for the staff. For example, during the preparation of an intravenous injection, the connection of the syringe to the intravenous line can lead to potential contamination. For instance, biomonitoring of trace amounts of cytotoxic drugs in the urine or blood samples of healthcare workers is highly required. Moreover, these analyses should be very sensitive and selective since drug concentrations in the biological fluids of workers are significantly lower than those of patients[156].

For practical reasons, urine is preferred over blood even if the drug concentrations are generally lower. Several studies have analyzed healthcare workers’ exposure monitoring urinary metabolites like in the work published by Ndaw et al. concerning the detection of 5-fluorouracil main urinary metabolite[157]. Commonly employed methods for the analysis of drug contamination in urine are gas chromatography- MS or LC-MS, which provide the required sensitivity.

Beyond the urine samples analysis, monitoring environmental contamination is essential to quantify potential health risks, and, with this aim, standardized sampling techniques and analytical methods are generally applied. Wipe sampling, in this regard, is used to assess residual contaminants on the surfaces of the workrooms and the effectiveness of personal protective equipment. A variety of materials like Kleenex professional wipes or glass fiber filters as well as different wetting solutions can be employed. Wipe sampling is followed by drug extraction and further analysis through instrumental techniques like voltammetry or LC-UV[158].

4.4 Doxorubicin: therapeutic and side effects

Doxorubicin is one of the most used chemotherapy drugs due to its broad spectrum of activity. Indeed, it is active against leukemia, lymphomas, and a variety of solid tumors. It belongs to the family of Anthracyclines, a class of antibiotics glycosidic derivates of tetrahydronaphthacene. The antineoplastic activity of these drugs has been mainly attributed to their strong interaction with DNA at different levels: intercalation between the base pairs, strand breakage, and the inhibition of the topoisomerase II enzyme[159]. Adverse effects include nausea, vomiting, myelosuppression, alopecia, and highly relevant cardiotoxicity (see fig.59)[160,161].

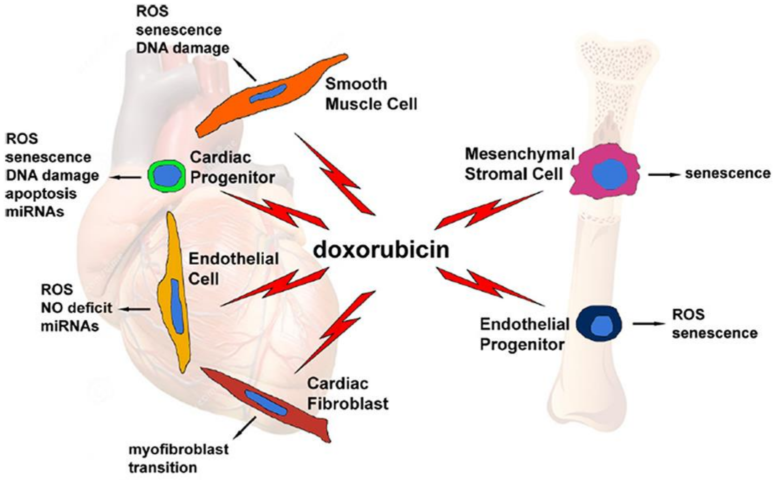
ROS
senescence
DNA damage
Smooth
Muscle Cell
ROS
senescence
DNA damage
apoptosis
miRNAs
Cardiac
Progenitor
Mesenchymal
Stromal Cell
senescence
Endothelial
Cell
doxorubicin
ROS
NO deficit
miRNAs
Endothelial
Progenitor
ROS
senescence
Cardiac
Fibroblast
myofibroblast
transition

Figure 59. Doxorubicin's adverse effects[160].

4.4.1 Doxorubicin: detection strategies

Due to its high toxicity, the regulated dosage of doxorubicin is essential in chemotherapy. This anticancer drug can also penetrate protective clothes and, when it is administered at the therapeutic concentration (2 mg/mL), it has been reported to persist on the hand of a volunteer for 30 seconds, even after washing with common detergent[156,162]. Therefore, analyses of doxorubicin contamination in hospital settings and in the biological fluids of healthcare workers are of great interest. To date, the analytical reference techniques are HPLC[163,164], spectroscopic methods[165,166], MS[167], and electrochemical sensors[168,169].

For example, the environmental monitoring of doxorubicin on contaminated surfaces was successfully achieved by Bobin-Dubigeon and coworkers using an LC-MS method. Coupling a solid-phase extraction approach with wiping filter paper, they obtained, after 30 minutes, the separation of the sample to be detected which was further analytically analyzed reaching a LoD of 5 ng. This instrumental technique proved to be suitable to assess the exposure of healthcare workers in the cancer research hospital[170].

Likewise, several works reported the assessment of doxorubicin in urine samples of healthcare workers. Sottani et al. in their toxicologic study, for example, employed a reversed-phase HPLC interfaced with electrospray ionization, and coupled to tandem MS. The method reached a LoD of 0.3 mg/L and was validated on urine samples of pharmacy technicians and nurses who work in hospitals[171].

Although instrumental techniques are all highly accurate and sensitive, they require trained personnel for the interpretation of the results, as well as costly instrumentation, long-time, and multistep procedures. Fast and on-site sensing methods would represent a key technological advancement, and POCTs, in this context, meet the desired requirement to address this issue, showing undoubted advantages over common laboratory techniques[172,173].

Among the different strategies of doxorubicin detection, exploiting its fluorescent properties appears a promising and versatile approach in cancer research and images. The molecule indeed acts as a biocompatible fluorophore which, when stimulated by ultraviolet (~250 nm) or blue light (~465 nm), emits a broad-spectrum orange-red light (530-700 nm range) (see fig.60A)[174]. Motlagh and coworkers demonstrated a strict dependence of the fluorescent signal intensity with the fluorophore concentration as clearly shown in fig.60B[175].

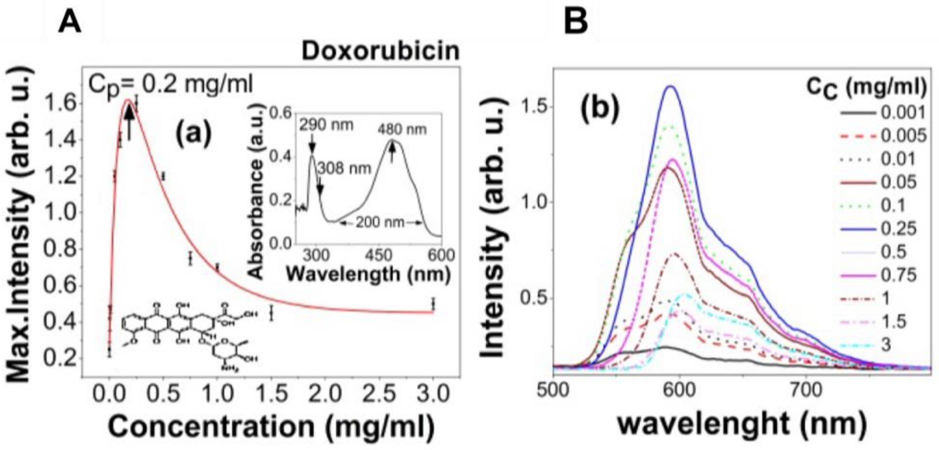

Figure 60. A) Peak intensity in terms of concentration of doxorubicin and corresponding UV-vis spectra of the drug; B) fluorescent peak as a function of the drug concentration[175].

This property has been largely exploited in cancer therapy[175], for example aiming to monitor the drug release from delivery vehicles composed of silica (SiO_2) NPs[176]. In this work, following the drug fluorescence, the authors demonstrated the efficiency of this innovative system in releasing the drug into cancer cells, proving it to be a good candidate for drug delivery and clinical application.

However, to the best of our knowledge, only a few articles reported the analysis of doxorubicin contaminations on surfaces exploiting the intrinsic fluorescence of the molecule[177], especially in the context of POC sensors.

4.5 Our strategy: a POC device for on-site detection of doxorubicin contamination

This work aims to develop a simple and rapid POC device which can be exploited on-site for the assessment of healthcare workers' exposure to doxorubicin by analyzing surface contamination and urine. The proposed POC device was designed in the configuration of an LFA with some innovative modifications[178].

Conventional LFA, both in the competitive and in the sandwich format, are based on the use of label molecules for the naked-eye detection of the signal and a capture probe that selectively binds the analyte, enabling the sensing process. Regarding the first point, commonly used label molecules are nanomaterials characterized by remarkable optical properties. Among them, AuNPs have become the most widely used detection labels for their LSPR and tunable plasmonic properties which produce a vivid color and a significant colorimetric variation. AuNPs have low toxicity, they can be easily functionalized, and they are relatively stable; however, they require precise optimization and strict control of the synthetic procedure to obtain a standardized morphology which allows for a reproducible read-out signal[23]. On the contrary, in the LFA that I proposed for the detection of doxorubicin, I exploited the intrinsic fluorescence of the drug to achieve a naked-eye detection instead of the NPs.

Concerning the detection mechanism, in conventional LFA, the capture bioreceptor is mainly represented by an antibody that has a strong binding affinity for the target molecule. However, for the detection of doxorubicin, there is a very limited commercial availability of anti-doxorubicin antibodies and, if present, they present remarkably high costs. For instance, I proposed a promising and novel recognition mechanism that exploits the pharmacological interaction of doxorubicin with its biological target, namely dsDNA (double-strand DNA), avoiding hard-to-find antibodies, whilst gaining in the lowering of the costs. Furthermore, exploiting the pharmacological interaction of the drug with DNA significantly boosts the specificity and sensitivity of the assay[179].

Concerning the detection mechanism, I immobilized the dsDNA in the test region of the LF device to enable the intercalation when the drug flows through the running pad. NALFAs have been largely reported in the literature and they are gaining increasing interest. NALFAs have been developed for the detection of several targets like DNA sequences, biomarkers, metal ions, and drugs of abuse[180–183]. Most of them, are based on single-strand DNA (ssDNA) or aptamers which are primarily used for hybridization-based platforms for the complementary recognition of a target oligonucleotide strand. ssDNA-based NALFAs have been reported for the detection of pathogens in food and water[184,185] and, as demonstrated by Jauset-Rubio et al., for the rapid detection of the isothermally amplified DNA[184]. On the contrary, aptamers-based NALFAs are mainly exploited for the detection of toxins achieving a sensitivity that is even better that that of conventional LFA[30].

To the best of our knowledge, no NALFA has been reported for the detection of doxorubicin, and generally of cytotoxic drugs. Furthermore, no examples of NALFA with a dsDNA as the capture probe have been shown in the literature. Hence, my LF device combined these innovative features to realize a valid POCT for the detection of doxorubicin contamination on surfaces and urine, aiming to monitor and limit healthcare workers’ exposure in occupational environments.

4.6 Results and discussions

4.6.1 Device design and detection mechanism

The proposed LF device is illustrated in fig.61. It was a simplified LFA with no conjugate pad because I exploited the intrinsic fluorescence of doxorubicin instead of label molecules for the detection. It was mainly composed of a running pad and an absorbent pad. In the middle of the running pad, 15 mm far from the origin, in the “test region” zone, I placed a drop (0.5 µL) of dsDNA, that acted as the capture probe. The sample was deposited on the running pad, it flowed exploiting the capillary forces and it passed across the test region where, if the drug was present in the sample, the intercalation occurred, and doxorubicin remained captured. Upon irradiation by a simple UV lamp, the test region emitted an intense orange-red fluorescent signal which could be appreciable by the naked-eye with no further instrumentation. In the case of non-contaminated samples, no intercalation happened and, hence, no fluorescence was visualized.

Specifically, I selected a positively charged nylon (nylon+) membrane as the running pad and a blend of cotton and glass fibers as the absorbent pad which, due to the high wicking capacity, enabled the deposited sample to reach efficiently the end of the strip exploiting the capillary force. Materials were cut obtaining a final width of 4 mm and they were assembled on a backing card, overlapped each other. The deposition of dsDNA was realized by exploiting the electrostatic interaction between the nucleotide with its negatively charged phosphate groups and nylon+.

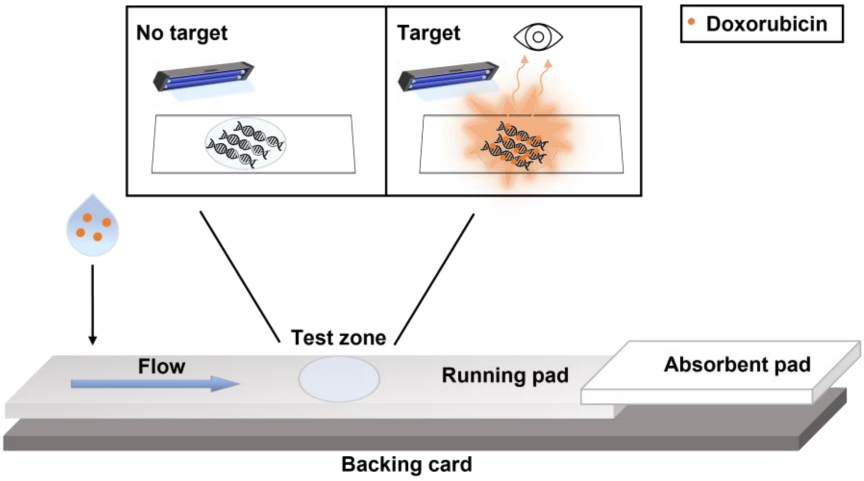

Figure 61. Schematic illustration of the LF device for the detection of doxorubicin contamination on surfaces and urine. The device is composed of a nylon+ membrane as the running pad and a blend of cotton and glass fibers as the absorbent pad, laminated on a backing card. In the test zone, there is a spot of dsDNA, used as the capture bioreceptor. The test sample is deposited on the lateral side of the running pad, and it flows through the membrane exploiting the capillary forces. If doxorubicin is present in the sample, it intercalates with the dsDNA, conferring an intense, naked-eye fluorescence to the test region upon irradiation by a UV lamp. In the case of a non-contaminated sample, no fluorescence is visualized.

4.6.2 Optimization of the capture probe

For the realization of the LF device, I performed several optimizations starting from the immobilization of the capture bioreceptor. As previously anticipated, I exploited the electrostatic interaction between the dsDNA and the running pad. The reported strategies for DNA probe immobilization are chemical and physical adsorption[186,187]. The first approach relies on the use of linker molecules which enable a strong and stable immobilization of the probe, for example exploiting the binding between streptavidin and biotinylated capture ssDNA[188]. Although this approach enables efficient and sensitive detection, it implies high costs which are not suitable for a POCT. For instance, I opted for physical adsorption that does not include chemical reagents and DNA modification.

With this aim, as illustrated in fig.62, I tested four different running pads: nylon+ (A), nitrocellulose western blotting membrane (B), nitrocellulose membrane CN95 (C), and Whatman qualitative filter paper grade 1 (D). I placed a drop of 0.5 µL dsDNA and I ran the sample containing doxorubicin. I found that only nylon+ enabled a clear fluorescent signal under the UV lamp. This is mainly due to the electrostatic adsorption of DNA in the test region promoted by the positively charged groups of the membrane which allowed for a stable immobilization and the intercalation of doxorubicin, enabling the detection. As clearly shown in fig.62, the other tested substrates gave no signal due to an unstable immobilization of the probe which was washed away during the sample flow.

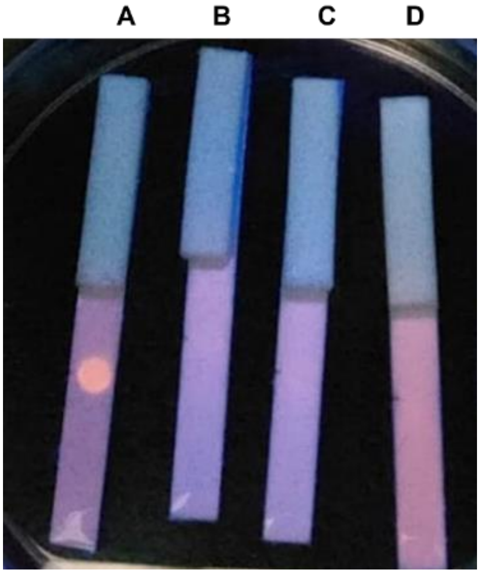

Figure 62. Performance of the device when the dsDNA probe is immobilized on different running pads: nylon+ (A), nitrocellulose western blotting membrane (B), nitrocellulose membrane CN95 (C), and Whatman qualitative filter paper grade 1 (D).

Referring to some published works[186], I tried to improve the probe immobilization process, using some molecules that should promote the ionic interaction creating a positively charged film. In particular, I tested poly-L-lysine[189] and chitosan[190] functionalized dsDNA that I immobilized as a spot on the test region. As shown in fig.63, when I run doxorubicin, no great improvements came from the use of these molecules. Indeed, chitosan gave false positive results while poly-L-lysine suffered from an uncontrolled drying process which led to non-uniform and non-reproducible signals, often characterized by coffee ring effects (fig.63B). DNA alone, on the contrary, showed the best signal, with a well-defined spot.

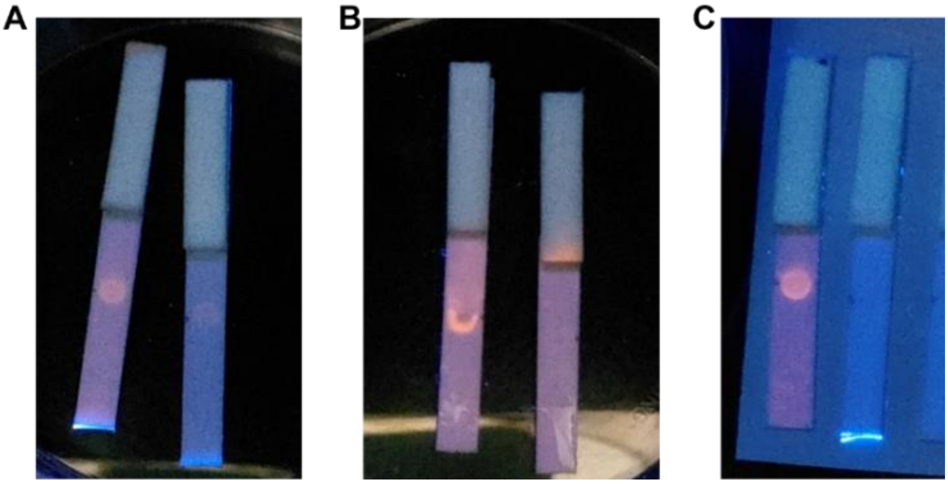

Figure 63. Detection of doxorubicin using an LF device with a capture probe composed of chitosan and DNA (A), poly-L-lysine and DNA (B), and DNA alone (C). Devices on the left were treated with a sample containing doxorubicin, and the ones on the right with the solvent alone.

Additionally, I examined how the nature of the dsDNA probe could influence the intercalation process; hence, I tested two different probes: a short chain (27 nucleotides) duplex oligonucleotide with 3' overhangs and DNA from calf thymus, composed of 10 Kilobase pairs. The performance of the devices treated with the two nucleotides after running a solution containing doxorubicin is illustrated in fig.64A. DsDNA oligonucleotide with 3'overhangs showed the best-defined signal upon exposure to UV light and, hence, it was selected as the proposed capture probe. The long DNA sequence suffered from a worst drying process, leading to a significant coffee ring effect of the fluorescent spot. The selected sequence took advantage from the presence of overhangs which promoted the electrostatic interaction between the negatively charged phosphate groups in DNA, in particular in the tails, and nylon+. Furthermore, it is reported that a smaller sequence presents increased flexibility and, hence, favored surface adsorption due to the reduced conformational restrictions[191]. To further verify this concept, I performed the assay on the devices prepared by immobilizing the two capture probes, testing decreasing doxorubicin concentrations (see fig.64B and C). The result confirmed that the selected probe allowed for increased sensitivity and a better-defined spot, with no appreciable coffee rings.

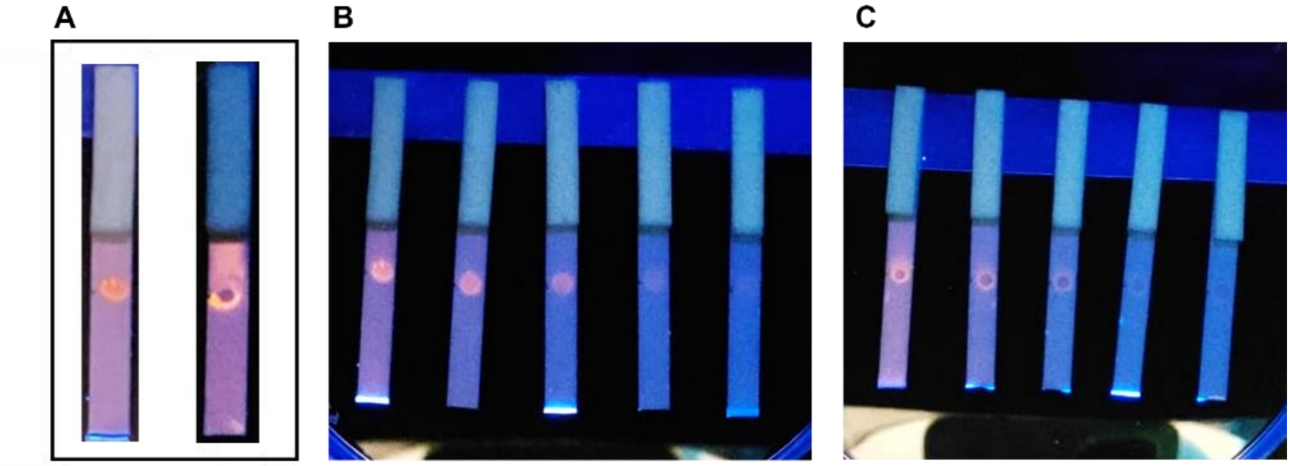

Figure 64. A) Comparison of the performance of two devices treated with a short dsDNA oligonucleotide with 3’overhangs (left) and DNA calf thymus (right); devices treated with a short dsDNA oligonucleotide with 3’overhangs (B) and DNA calf thymus (C) when decreasing concentrations of doxorubicin were tested (10, 5, 1, 0.5, 0 µM).

Finally, I evaluated two important aspects related to the capture probe concerning the drying time and the concentration. Regarding the first point, I tested the performance of the device at different drying time points: 5, 10, 30, and 60 minutes. Results are illustrated in fig.65. 60 minutes was the optimal time required for immobilizing the DNA probe, giving the best-defined fluorescent spot and a negligible fluorescent tail. Indeed, by using a shorter time, the probe was unstable and it was washed away when the sample flowed leaving a fluorescent tail.

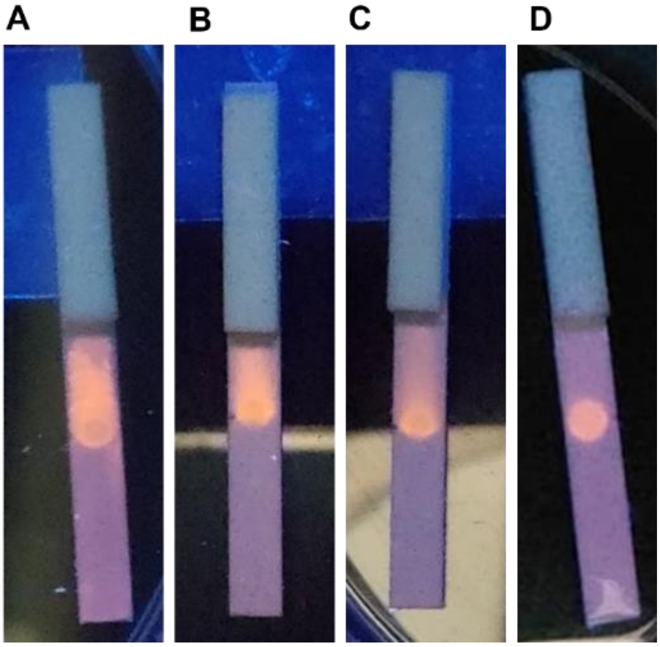

Figure 65. Evaluation of the drying time. The test was performed after drying the probe for 5 minutes (A), 10 minutes (B), 30 minutes (C), and 60 minutes (D).

The second aspect I optimized was the amount of the capture probe. With this aim, I immobilized increasing dsDNA concentrations (see fig.66): 1, 20, 100, and 200 µM. From the test, I could state that although 100 µM gave a well-defined fluorescent spot, 200 µM was the optimal concentration since it gave the best visual read-out.

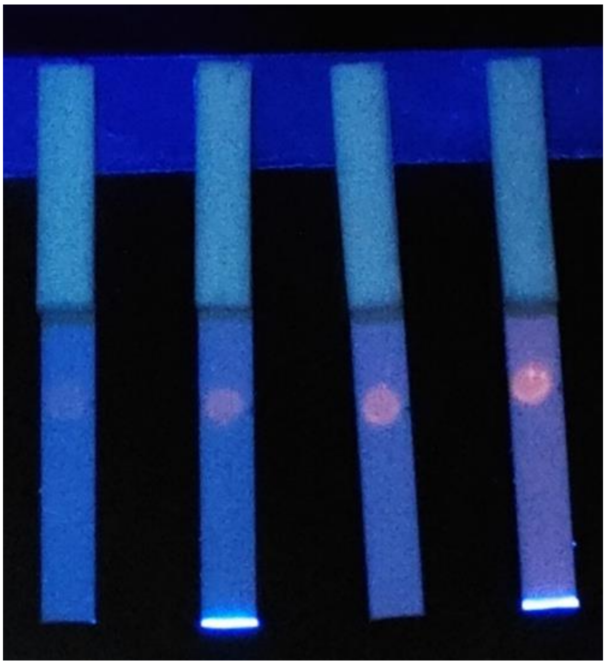

Figure 66. Comparison of the performance of the device after immobilizing increasing probe concentrations: from left to right, 1, 20, 100, and 200 µM.

4.6.3 Optimization of the flow

After determining the best conditions for the capture probe, I moved on to the optimization of the flow. Indeed, I selected the nylon+ membrane as the running pad due to its positive charge which promoted the stable immobilization of the dsDNA by exploiting the electrostatic interaction. However, this membrane was characterized by a small pore size (0.45 µm) which did not allow the flow of the sample due to the slow capillary flow rate[23]. Hence, I had to find strategies to overcome such issues, ensuring that the doxorubicin reached the end of the strip.

I started introducing sample pads composed of different materials (cotton and glass fibers) in the LF design to assess their ability to load the sample and ensure an even flow. As reported in fig.67, both pads retained a huge amount of doxorubicin. They allowed for the release of the solvent, but the flow of the target analyte was strongly hampered, due to the possible interaction of the doxorubicin molecules with the tested sample pads. Therefore, these pads were not included in the final design of the device.

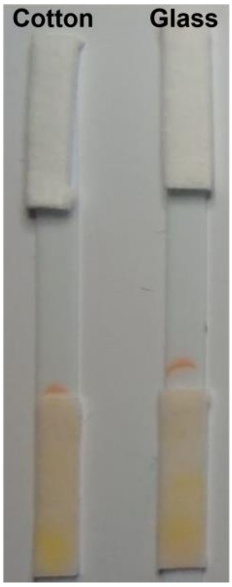

Figure 67. Performance of the device after including sample pads of cotton fibers (left) and glass fibers (right) in the design.

Successively, I studied the importance of the sample solvent. Firstly, I tested the performance of the device solving doxorubicin in water (see fig.68A). As it is shown in the photograph, water gave an uneven flow of the sample, hampering the analyte to reach the end of the strip. I had to add two further water supplements to enable the sample to complete the run, without stopping along the membrane. However, a residual fluorescence remained on the running pad (see the orange-red color of the substrate in fig.68A). Afterward, I tested different running buffers, commonly employed in LFA to promote a uniform flow. Specifically, I solved doxorubicin in BSA, Triton, SDS, Tris Buffer, and Tween (see fig.68B), without further additions of the solvents. As it is clearly illustrated in the picture, only Triton enabled a uniform flow of the sample containing the target since in all the other tested conditions doxorubicin stopped along the running pad and only the solvent was allowed to reach the absorbent pad.

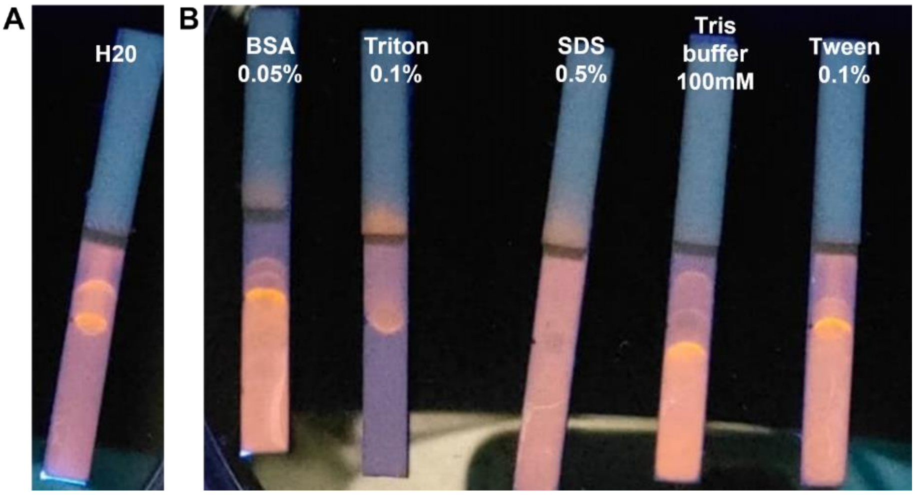

Figure 68. A) Device tested with a water solution of doxorubicin with two subsequent additions of water. B) Devices tested with doxorubicin diluted in BSA, triton, SDS, Tris buffer, and tween, with no further additions of solvents.

4.6.4 Analytical performance of the LF device

After defining the best assay conditions, I tested the analytical performance of my device aiming establish the sensitivity for doxorubicin detection. Hence, I placed on the running pad of different devices 30 µL of decreasing doxorubicin amounts (160, 80, 40, 16, 8, 4, 1.5 ng) and the negative control was simulated with 30 µL of the solvent (Triton) alone. As is shown in the photograph in fig.69A, a visible fluorescence could be appreciable down to a doxorubicin amount of 4 ng, which I considered my visual LoD (defined as the capacity of the human eye to appreciate the presence of a fluorescent spot). However, I further calculated the LoD of the device, analyzing the image of the fluorescent spots acquired by a smartphone device (see Methods for details). Specifically, I collected the green coordinate (G) of the spot in the RGB space, since green is complementary to the orange-red fluorescent signal. Then, I calculated the ΔG from the difference between the G values of the sample and that of the negative control. As shown in fig.69B, I plotted the dependence of ΔG on doxorubicin amounts and I found a good linear relationship between the two variables over the tested range. I could state that the LoD of my device was down to 1.5 ng. This result proves that my device is a valid and highly sensitive POC sensor for the detection of trace amounts of doxorubicin on contaminated surfaces since the sensitivity is comparable, and even superior, to other laboratory-based techniques, with the advantage of being instrument-free and rapid (see table 1).

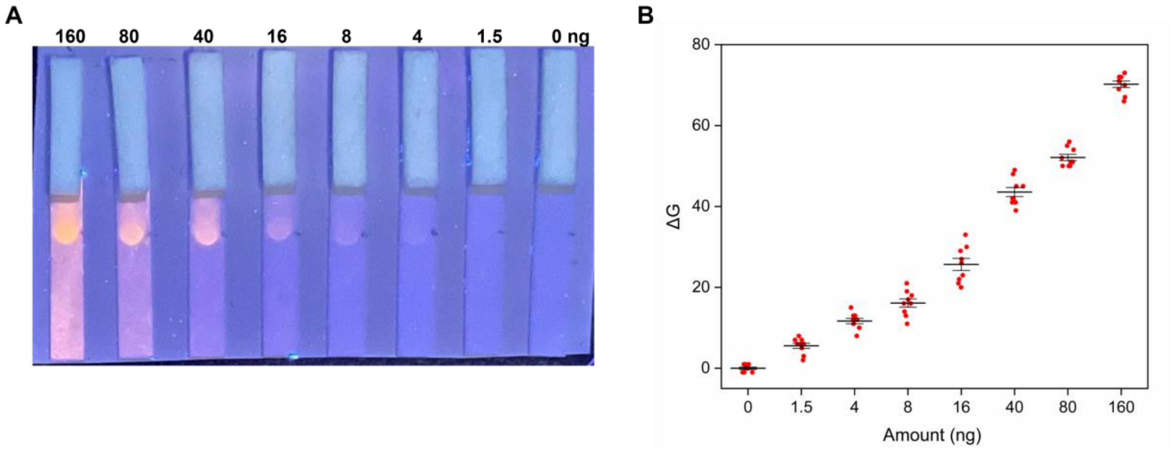

Figure 69. A) Performance of the device tested with decreasing doxorubicin amounts (reported in the upper part of the image); B) Dependence of the optical response on doxorubicin amounts (points represent the ΔG values of 9 independent experiments).

Sample Type	**LOD (µM)**	**Preparative procedure**	**Visual detection (Instrument-free)**	**Ref.**
Pharmaceutical formulations	0.034-0.22	-	X	[192]
Pharmaceutical formulations	0.46	-	X	[193]
Exhaled breath condensate	0.004	Water bath 70 °C for 10 min	X	[194]
Skin and surfaces	1.8	-	✓	[177]
Blood and plasma	0.92	Extraction with ethyl acetate and drying	X	[195]
Cultured cells	0.18	Washing and lysis	X	[196]
Urine samples	0.055	Flow injection	X	[197]
Surfaces and urine samples	0.10	-	✓	This work

Table 1. Comparison of UV-vis instrumental techniques and my POCT for the detection of doxorubicin.

4.6.5 Detection in urine

As I previously stressed, the assessment of healthcare workers' exposure to doxorubicin is generally performed by analyzing drug amounts in urine. With this aim I decided to test the performance of my device in a real urine sample, avoiding complex steps of pretreatment or purification of the sample to maintain the POC concept of the device.

Clinically, doxorubicin and its metabolites are eliminated through the urinary route. Indeed, the concentrations after the first infusion (0-4 h) are generally 95× higher than those in plasma and it ranges from 17 to 33 μM[198].

Most of the techniques reported in table 1 refer to the detection of doxorubicin in pharmaceutical formulations to avoid the possible interferences of biological components with the detection of the drug. The ones that used biological matrixes resort to pretreatment procedures before the sample analysis and they often achieve a LoD lower than that in aqueous solutions. Sikora et al., for example, spectrophotometrically studied doxorubicin in blood and plasma after a long procedure of extraction with ethyl acetate and centrifugation to separate the organic phase containing the drug from the solid components of the plasma and blood. The achieved LoD was 3 times lower than in aqueous solution[195]. However, these complicated procedures are not suitable for a POC device, hence, I had to face the complexity of the urinary matrix, avoiding the use of complicated instrumentations or pretreatment steps for the detection of doxorubicin.

First, I evaluated the interference of urinary salts (at their physiological concentrations) in the detection of the drug. For instance, as illustrated in fig.70, I tested samples prepared with equimolar solutions of doxorubicin spiked with urinary components singularly. As shown in the photograph of the treated devices, chlorides and ammonia completely blocked the signal, hampering the intercalation process. Sodium hydroxide strongly interfered with drug detection, resulting in a poorly defined spot.

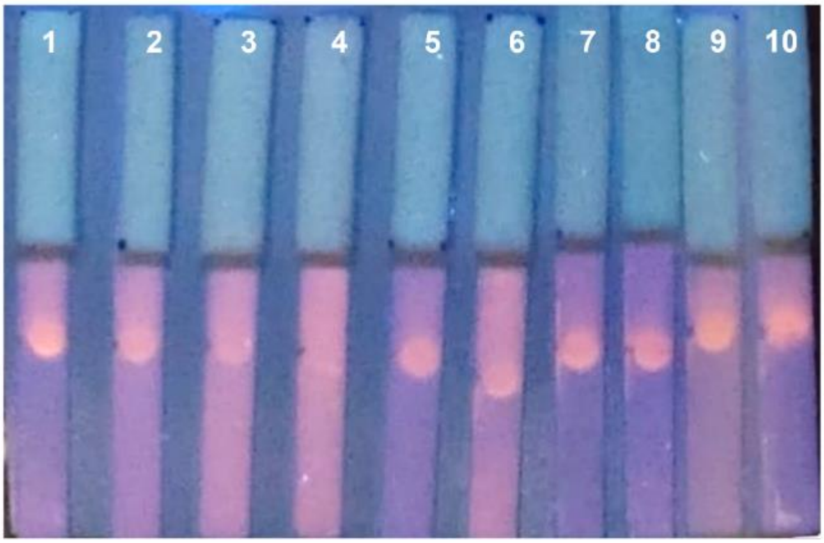

Figure 70. Interference study of urinary components on the detection of doxorubicin: no interferents (1), sodium and magnesium sulfates (2), sodium and potassium chlorides (3), ammonia (4), sodium phosphate and phosphoric acid (5), sodium hydroxide (6), sodium citrate (7), urea and uric acid (8), creatinine (9), and hippuric acid (10).

From this result, I could conclude that the interference came from a synergic combination of components rather than a single one. However, maintaining the initial idea of POCT, I tried to reduce this effect by diluting the sample. As reported in fig.71, I tested several dilutions of real urine after spiking it with doxorubicin. I observed a partial restoration of the fluorescence when a dilution of 1:5 was applied, while the best-defined signal was achieved with a 1:50 dilution. However, since the assay in real urine was performed by spiking the sample with the analyte and diluting it before the test, I decided to apply a factor of 1:10 to avoid an excessive sensitivity loss.

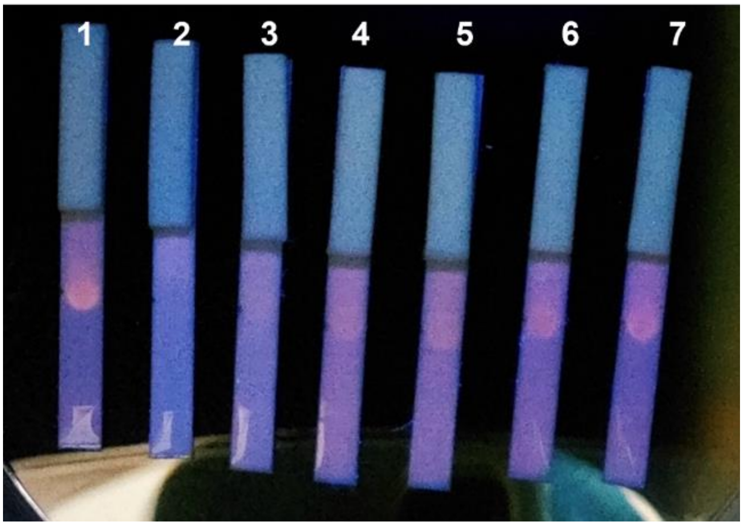

Figure 71. Performance of the device with real urine sample after sample dilution: no dilution (1), 1:1 (2), 1:2 (3), 1:5 (4), 1:10 (5), 1:25 (6), 1:50 (7).

After all these optimizations, I tested the analytical performance of the device for the detection of doxorubicin in urine to establish the visual LoD. As it is illustrated in fig.72, I spiked urine with decreasing drug amounts (240, 160, 80, 40, 16, and 0 ng). The samples were treated as previously reported (spiking the native urine with the desired target concentration and diluting it 1:10 in Triton), and I recorded the fluorescence after irradiating the devices with a UV lamp. The achieved LoD was down to 80 ng which, as previously mentioned, was lower than that obtained in the aqueous solution (4 ng); however, it was clinically relevant compared with the concentrations reported by Maliszewska and coworkers after the first 4 hours post-infusion[198].

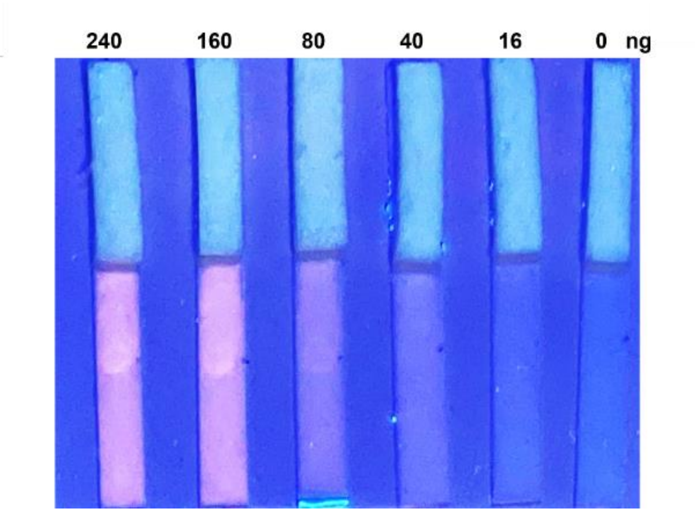

Figure 72. Analytical performance of the LF device with real urine samples spiked with decreasing doxorubicin amounts (reported in the upper part of the photograph).

4.7 Materials and methods

4.7.1 Chemicals

The chemicals employed for this project were of high technical grade and used without further purification. All solutions and buffers were prepared using ultrapure deionized water (MilliQ). Doxorubicin hydrochloride, bovine serum albumin, Tween-20, sodium dodecyl sulfate (SDS), deoxyribonucleic acid from calf thymus (Type XV), poly-D-lysine hydrobromide, chitosan, Triton™ X-100 solution, hippuric acid, creatinine, magnesium sulfate heptahydrate, sodium sulfate, potassium chloride, sodium chloride, sodium citrate tribasic dihydrate, urea, uric acid, ammonia solution 25%, sodium phosphate dibasic, phosphoric acid, and sodium Hydroxides were purchased from Merck (Sigma-Aldrich). UltraPure™ 1 M Tris-HCI Buffer, pH 7, TE Buffer (20X) were purchased from ThermoFisher. For use as a sensing element, a 3'overhangs duplex sequence was designed, and purchased from Integrated DNA Technologies.

Sample pad (grade 319, composition Cotton Fibers), sample pad (grade 8980, composition Chopped Glass w/Binder), and absorbent pad (grade 440, composition Cotton/Glass Blend) were purchased from Ahlstrom-Munksjö. As running pad Whatman® qualitative filter paper, Grade 1, Hybond®-N+ hybridization membranes, Amersham™ Protran® Supported Western blotting membranes, nitrocellulose were purchased from Merck (Sigma-Aldrich) while Unisart® nitrocellulose membrane (CN95) was purchased from Sartorius.

4.7.2 Instrumentation

UV lamp (UVP UltraViolet Product™ EL Series UV Lamps, 95-0252-02) was purchased by Fisher Scientific (part of Thermo Fischer Scientific).

4.7.3 Lateral flow device assembly and electrostatic immobilization of the capture probe

The LF device was composed of a strip of nylon+, which acted as the running pad and cut in a rectangular shape with a final dimension of 4 mm ×25 mm, and by a piece of the absorbent pad with a size of 4 mm × 18 mm. The two materials were laminated on a backing card, with a partial overlap of 2 mm, and, hence, the final dimension of the device was 4 mm × 40 mm. Concerning the optimizations of the running pads, Whatman® qualitative filter paper, Amersham™ Protran® Supported Western blotting membranes, and Unisart® nitrocellulose membrane were tested and their performances were compared with that of nylon+. Regarding the optimization of the capture probe, 0.5 µL of 3′ overhangs duplex sequence (200 nmol double-stranded DNA (dsDNA)) and DNA calf thymus were dropped on the test zone, 15 mm far from the beginning of the running pad, and in the middle of the strip. The immobilization of the dsDNA was promoted by the electrostatic interaction between the negatively charged phosphate groups of DNA and the positively charged membrane. The probe was allowed to dry for 60 minutes at room temperature before testing of the sample. Solutions of capture probe and poly-L-lysine and chitosan were prepared by mixing the two reagents in an equal volume (200 nmol dsDNA was incubated with 0.1 mg/mL aqueous solution of poly-L-lysin and with 0.01 % (m/v) diluted acetic acid solution of chitosan). The as-prepared solutions were immobilized as previously reported for the selected probe.

4.7.4 Assay procedure and data processing

For the performance of the assay, I placed a drop of 30 µL of doxorubicin hydrochloride, previously solved in water and diluted at the desired concentration in 0.1 % Triton solution, on the running pad at the beginning of the strip. Negative controls were prepared by treating the device with the solvent alone (Triton at the same volume and concentration). After the deposition of the sample, it took about 20 seconds to reach the end of the strip, flowing uniformly till the absorbent pad. Considering the wicking capacity of the absorbent pad, 30 µL were established as the correct volume to avoid overflow and to allow the fluid to reach the end of the strip. For ensuring an even flow, I solved doxorubicin in different buffers: 0.05% BSA solution in PBS, 0.5% SDS solution in PBS, 100 mM Tris Buffer solution, and 0.1% Tween solution in PBS, and compared with doxorubicin solved in Triton X-100. The fluorescent signal was evaluated upon irradiation by a UV lamp operating at 254 nm. At the end of the assay, a smartphone image was recorded, and the image analysis of the fluorescent spot was realized through ImageJ software, collecting green coordinates (G) of the RGB space. G was selected as the most significative coordinate to analyze the evolution of the orange-red fluorescent spot since it is the complementary color, and, hence, it showed the largest variation in the color change and the highest sensitivity[195,199]. ΔG coordinates were obtained by subtracting the G values of the samples from those of the negative controls (strip treated with the solvent alone). Data analysis was performed by collecting the G coordinate of 9 independent experiments. The LoD of the device was obtained by testing decreasing doxorubicin amounts and mathematically following the equation: $(3.3\times\sigma)/S$ where σ is the standard deviation of the response and can be determined as the standard deviation of the blanks and S represents the slope of the graph in the linear range[200].

4.7.5 Assay in a real urine sample

For the assessment of doxorubicin amounts in a real urine sample, I first evaluated the interference of all the urinary salts singularly. I solved the drug in aqueous solutions of the salts at their physiological concentration[201] and I tested the detection ability of the device. Then, I moved to a real urine sample that I spiked with 10 µM of doxorubicin and I further diluted 1:10 in Triton to avoid the synergic interplay of the urinary salts without an extreme sensitivity loss. For the evaluation of the LoD of the device in urine, I spiked the biological fluid with decreasing doxorubicin amounts, and I diluted the sample 1:10 in Triton. The experiments were carried out in triplicate.

4.8 Conclusions

To assess healthcare workers' exposure to doxorubicin in hospital settings, I designed a POC device that allowed for visual and immediate detection of trace amounts of the drugs both on contaminated surfaces and in urine. The design was based on a conventional LFA with some important novelties. I exploited the intrinsic optical properties of doxorubicin which produces an orange-red fluorescence when stimulated by a UV lamp for naked-eye detection, without resorting to additional label molecules. Moreover, regarding the recognition mechanism, I avoided the use of antibodies. Indeed, although antibodies are the most widely used capture bioreceptors in LFA, anti-doxorubicin antibodies present very limited commercial availability and high costs. On the contrary, I exploited the pharmacological interaction of the drug with dsDNA, which I used as the capture bioreceptor in the test zone.

The sample was deposited on the running pad and it flowed through the strip due to the capillary forces of the membrane and the high wicking capacity of the absorbent pad. In case of doxorubicin was present in the sample, passing through the test zone, it intercalated with the dsDNA, and remaining captured. The detection was immediately visualized as an intense fluorescence of this zone after the UV irradiation.

For the realization of a valid and sensitive POC device, I performed several optimizations related to the running pads since I found that only a positively charged nylon membrane was able to stably immobilize the DNA probe thanks to the electrostatic interaction between the positive membrane and the negative phosphate groups of the dsDNA. To further promote the electrostatic immobilization, I selected a short dsDNA with 3' overhangs as the probe since it gave a more defined and uniform spot due to its superior flexibility compared to a long sequence. Moreover, it presented a higher number of free negative phosphate groups in the tails which enabled for a more stable deposition. Further experiments were performed aiming to improve the flow of the sample containing the drug, ensuring an even flow, and to avoid the doxorubicin to stop along the membrane. I found that Triton was the proper solvent since, thanks to its detergent ability, it enabled the flow of both the solvent and the target till the end of the strip, allowing for the intercalation.

After all the optimizations, the sensitivity of the device was studied in order to determine the LoD. I tested decreasing doxorubicin amounts and I found that the visual LoD was down to 4 ng. With further investigations, obtained by analyzing the fluorescent spots and recording G coordinates (complementary to the orange-red fluorescence), I found that the LoD was 1.5 ng. This result was comparable and even superior to other laboratory techniques, with the advantage of being portable, instrument-free, and rapid. The proposed POC device appears as a promising candidate for the on-site assessment of surface contamination.

In the final part of this work, I investigated the ability of my device to detect doxorubicin in a real urine sample. Contrarily to what many works reported, I avoided complex pretreatments of the biological sample to maintain the point-of-care concept of my device. In particular, after finding that urinary salts synergically interfered with the detection process, I diluted the sample 1:10. At these conditions, I tested my device with decreasing doxorubicin amounts in a real urine sample and I found that the visual LoD was down to 80 ng which is clinically relevant for the drug monitoring in non-invasive fluids.

Overall, the proposed POCT shows interesting perspectives for routine monitoring of doxorubicin, possibly improving the safety of healthcare workers as well as the clinical practice, paving the way for personalized therapy.

CHAPTER 5

AN INNOVATIVE LATERAL FLOW DEVICE FOR METHOTREXATE DETECTION

5.1 An overview of methotrexate

Methotrexate (MTX) is a folic acid antagonist and shares with it a very similar structure (see fig.73A). MTX is a potent inhibitor of dihydrofolate reductase (DHFR), which is involved in the regeneration of tetrahydrofolate from dihydrofolate[202]. The inhibition of DHFR hampers DNA and purine biosynthesis (see fig.73B). MTX is used against a wide range of tumors such as leukemia, breast cancer, sarcoma, and prostate cancer[203]. Moreover, at a low dose, MTX is also largely employed against inflammatory diseases like psoriasis and rheumatoid arthritis since it acts on nucleotide metabolism, mitigating cytokine signaling[204]. However, MTX is highly toxic and can induce severe side effects in treated patients because the therapeutic range, between the minimal effective concentration and the maximal toxic concentration, is very narrow[205]. Myelosuppression and pancytopenia are the most common hematological toxicity[206]. Moreover, MTX and its primary metabolite 7-hydroxymethotrexate induce nephrotoxicity which leads to altered elimination and elevated plasma concentration of the drug, increasing its toxicity[207].

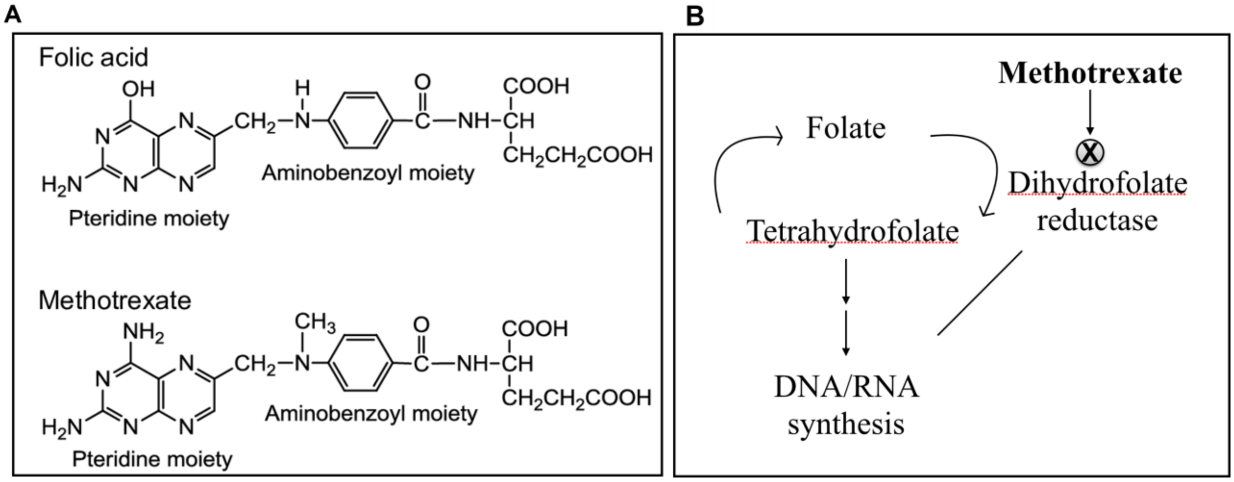

Figure 73. A) Comparison of the chemical structure of MTX and Folic Acid; B) Action mechanism of MTX.

Furthermore, MTX absorption and clearance in the organism are influenced by many factors, including age, gender, and metabolism. MTX is classified as dangerous due to its reproductive toxicity in human. Therefore, TDM in patients' body fluids is essential to control its pharmacokinetics and toxicity. Moreover, cases of contamination of professionals who handle this molecule have been reported in the literature since the 1990s. Recently, MTX has been detected in the urine of healthcare workers in concentrations ranging from 2.5 to 380 ng/L[208]. Nussbaumer and coworkers demonstrated a remarkable environmental toxicity of MTX by examining different contaminated surfaces with a wipe sampling procedure, followed by the analysis through LC coupled with tandem MS[209]. Hence, routine monitoring of professionals' exposure to MTX as well as the evaluation of the effectiveness of preventive measures like protective equipment are essential.

5.2 Methotrexate detection strategies

To date, the reference analytical techniques of MTX monitoring for therapeutic aims and environmental contamination are time-consuming and rely on complex instrumentations and centralized laboratories such as HPLC equipped with UV-vis[210], fluorescence[211], and MS[212], LC coupled with capillary electrophoresis[213], and electrochemical methods[214,215]. Nanomaterial optical probes have been used to increase the sensitivity and lower the detection limits. In this regard, Chen et al. reported a novel strategy for MTX detection in real samples exploiting a fluorescent probe composed of bovine serum albumin stabilized luminescent Au nanocluster. The proposed method is based on the selective quenching of the BSA-nanocluster fluorescence intensity upon the addition of MTX (see fig.74). The authors reported the sensitive detection of MTX in the range of 0.0016 µg/mL to 24 µg/mL with an achieved LoD of 0.9 ng/mL[216].

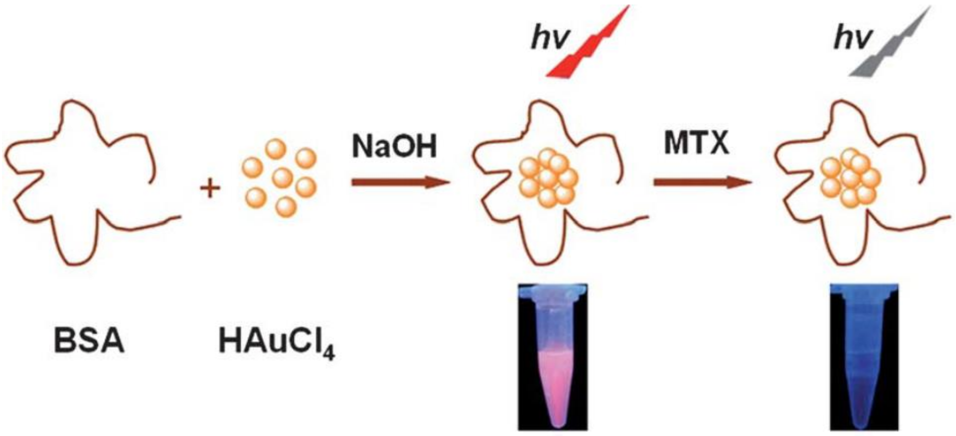

Figure 74. MTX detection mechanism based con BSA-Au nanoclusters[216].

Most of the standard assays for MTX detection rely on expensive and complicated protocols, often including pretreatments of the sample. Hence, a fast and on-site POC device would represent a technological advancement in MTX detection to ensure a continuous monitoring of the environmental contamination. In this context, a simple and inexpensive nanobiosensor has been recently developed. The sensing strategy is based on a competitive assay involving folic acid-derived AuNPs and human DHFR (hDHFR). The proposed mechanism is illustrated in fig.75. Specifically, AuNPs are deposited on solid support (a small glass sensor) after conjugation with hDHFR. When the solutions of folic acid-derived AuNPs and MTX are added, they enter a competition for the same binding site, namely hDHFR. Consequently, depending on the drug concentration, a dimer of AuNPs is formed, which induces a plasmon coupling and a consequent redshift appreciable by the naked-eye. MTX is calibrated in the range between 1 to 1000 nM and the visual LoD is 5 nM, showing comparable and even superior performances to other detection techniques[217].

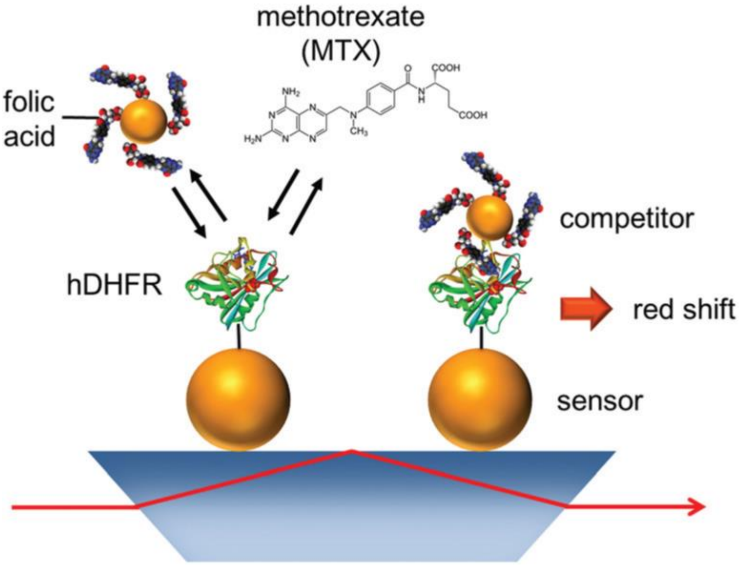

Figure 75. The naked-eye nanobiosensor for MTX detection[217].

The proposed system allows for a naked-eye detection, and it enables a semi-quantitative result which is extremely useful for POCT. Moreover, the proposed recognition strategy shows an important novelty: the authors replace the use of conventional recognition probes like anti-MTX antibodies with DHFR, which on the contrary is characterized by lower costs and larger availability. However, the strategy requires multistep additions with a delay time between them, which are detrimental for a POC assay.

5.3 Our strategy: a POC device for on-site detection of methotrexate contamination

In this work, I combined the previously reported sensing strategy for the detection of MTX[217] with a novel POC device in an LF configuration. My device offered a visual read-out signal provided by spherical AuNPs of 35 nm used as label molecules. To the best of our knowledge, no LF devices have been developed for the on-site and rapid detection of MTX. The use of the DHFR probe as the recognition mechanism, instead of expensive antibodies, strongly lowered the final cost of the device, making it more suitable for routine analysis of drug contaminations, whilst maintaining the specificity of the assay.

5.4 Preliminary results and discussions

5.4.1 Device design and detection mechanism

The schematic illustration of the device is represented in fig.76.

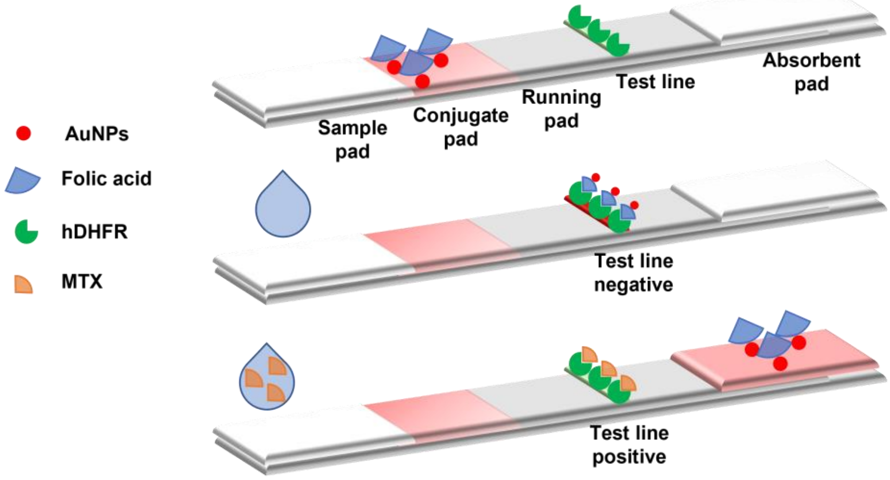

Figure 76. Schematic illustration of the proposed LF device for MTX detection.

I realized the on-site and instrument-free POCT for the detection of MTX on contaminated surfaces in an LF configuration. It was composed of a sample pad made of cotton fibers, a glass fibers conjugate pad functionalized with 35 nm AuNPs conjugated with folic acid, a running pad of nitrocellulose, and an absorbent pad made of a blend of cotton and glass fibers. Regarding the test line, I dropped a solution (0.6 µL) of the enzyme hDHFR, used as the capture bioreceptor, on the test zone. I let the device dry overnight to ensure the stable immobilization of the capture bioreceptor on the running pad and to avoid it being washed away when the sample flows on the membrane. I finally assembled the functionalized pads on a backing card before performing the assay. The sample was deposited on the sample pad and, exploiting the capillary forces, it passed across the conjugate pad, dragging with it the conjugate solution. Then, it flowed through the running pad, where it interacted with the t-line made of hDHFR, and the assay ended when the solution reached the absorbent pad.

The mechanism exploited for MTX detection was based on the general principle of a competitive LFA. Competitive assays are generally used for small target molecules that cannot be efficiently recognized by more than one bioreceptor[23]. Specifically, hDHFR selectively recognizes folic acid but also its unreactive analog MTX, which competes for the same binding site. If MTX was present in the sample, it bound to hDHFR on the test line, leaving fewer enzyme molecules available to link folic acid-conjugated AuNPs. Thus, increasing concentrations of MTX in the tested sample resulted in fewer AuNPs in the test line. Since AuNPs are characterized by a visible LSPR, they imparted a naked-eye vivid color to the t-line. The higher the drug concentration, the lower the intensity of the t-line, until it disappeared when the MTX concentration was very high.

5.4.2 Synthesis of the label molecules

Regarding the functionalization of the pads, I started preparing the conjugate solution that I placed on the conjugate pad. To this aim, I synthesized the label molecules for the visual readout of the signal. As in a conventional LFA, I exploited the plasmonic properties of AuNPs. Specifically, I synthesized spherical 35 nm AuNPs through seeded growth. It is reported that the sensitivity of an LFA biosensor is significantly influenced by the amount of accumulated AuNPs captured in the t-line and by the NP size[218–220]. AuNPs sizes around 20 and 40 nm are the most popular for the development of LFA because they are big enough to provide a clear and bright signal and small enough to avoid self-coagulation and instability[220]. Although bigger AuNPs should be characterized by increased signal visibility, their conjugation efficiency tends to decrease, leading to a weaker signal. Smaller NPs, on the other hand, require a fewer amount of antibody for the conjugation compared to bigger sizes but they have less sensitivity to detect the target[221]. For instance, I selected spherical 35 nm AuNPs as a compromise in the size and because they are often used in LFAs[222]. For their synthesis, I started from 15 nm AuNPs (see chapter 2, fig.24) and I exploited the selective reducing agent hydroxylamine to reduce Au (III) to bulk metal, which further deposited on Au seeds. I finely modified the ratio between the volume of the seed and the concentration of the Au salt to obtain the desired particle size. As can be seen in the characterization reported in fig.77, I finally obtained well-monodispersed spherical AuNPs with a diameter of about 35 nm and an LSPR peak at 525 nm, which provided an intense red color to the colloidal suspension.

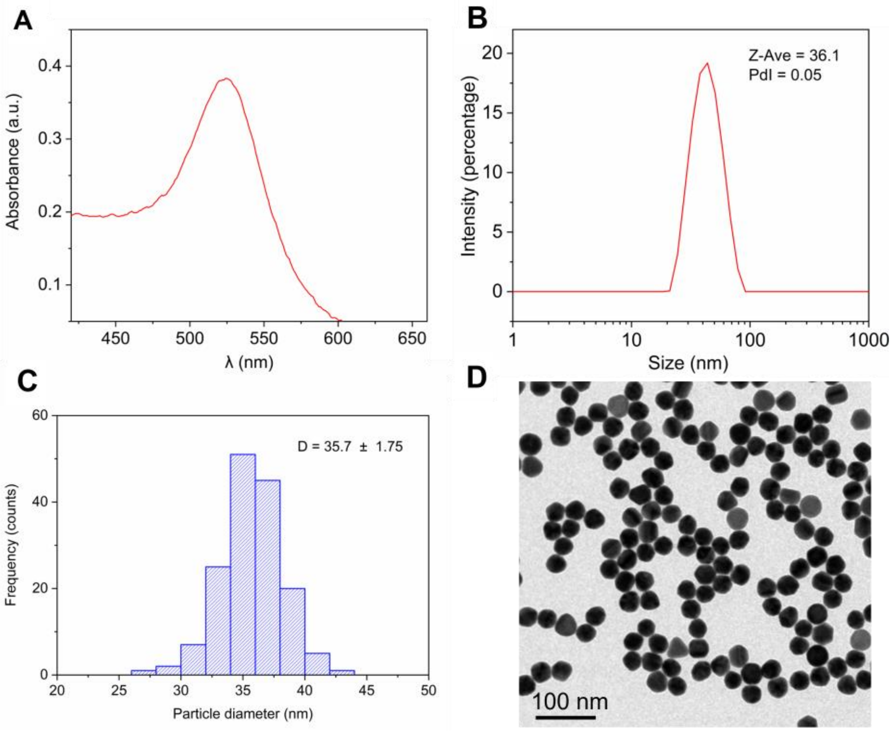

Figure 77. 35 nm AuNPs characterization including A) UV-vis absorption spectrum, B) DLS measurement, C) TEM size distribution analysis D) TEM micrograph.

5.4.3 Optimization of the conjugate solution

For the preparation of the conjugate, I followed the protocol reported by Yockell-Levièvre et al. in their work[217]. Specifically, I incubated a concentrated suspension of AuNPs with folic acid, and, after a centrifugation step to remove excess reagents, I deposited the solution, at the desired dilution, on the conjugate pad. However, when I solved folic acid and I resuspended the conjugate in ethanol, as reported in the article's procedure, I found that aggregation of the NPs occurred. Indeed, as is shown in fig.78A, the color of the conjugate appeared violet instead of the vivid red of the initial colloidal suspension of AuNPs. Moreover, when I tested the performance of the device by depositing a water solution on the sample pad to simulate the control, the flow of the label molecules through the running pad appeared strongly uneven and the signal was very weak (see fig.78B). On the contrary, when I replaced ethanol with water, the conjugate pad solution maintained the original red color, excluding aggregation phenomena, and the assay performance appeared strongly improved (see fig.78C and D). Hence, water was chosen as the solvent for the preparation of the conjugate.

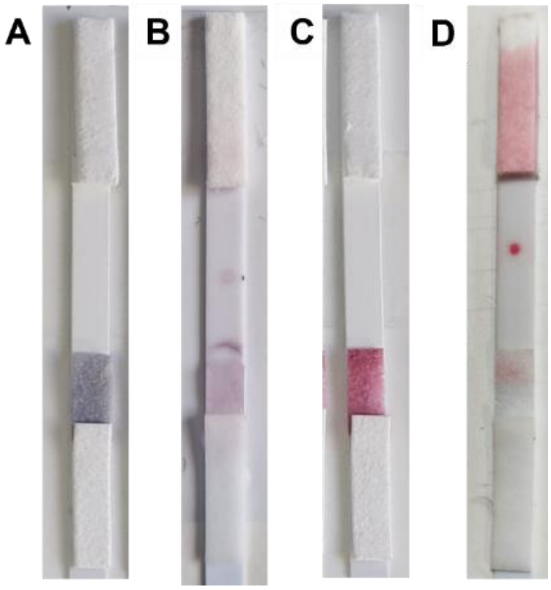

Figure 78. A) LFD assembled with the conjugated pad prepared in ethanol; B) performance of the LFD in A) treated with water (control solution); C) LFD assembled with the conjugated pad prepared in water; B) performance of the LFD in C) treated with water (control solution).

Regarding the optimization of the conjugate, I finely tuned the concentrations of folic acid and the solution to be deposited on the pad. Indeed, in a competitive LFA the concentration of the detection bioreceptor must be carefully adjusted to avoid the oversaturation of the signal in the absence of the target, which would produce a low-sensitivity assay. As shown in fig.79A, I conjugated AuNPs with two folic acid concentrations (100 µM and 75 µM). I functionalized the conjugate pads and let them dry under vacuum. After assembling the test strip, I treated the devices with water (namely

Ctrl in the picture) and a solution of 250 µM MTX (namely MTX in the picture), which should provide a signal intensity decrease due to the competition of the drug with folic acid in the conjugate. As illustrated in fig.79A, when 100 µM folic acid was tested, the competition process was hampered, resulting in the same intensity of the red spot compared to that of the control. On the contrary, a clear and distinguishable weakening of the signal occurred when 75 µM folic acid was used, hence, it was set as the optimized concentration.

Concerning the optimization of the signal intensity, which is dictated by the AuNPs, I tested different concentrations of the conjugate (see fig.79B). Specifically, after the steps of incubation and centrifugation, I prepared three dilutions of the as-prepared solution (1.2, 1, and 0.8 nM) that I deposited on the conjugate pad. I performed the assay flowing water and I compared the intensity of the spot. The signal produced by the lowest concentration provided a too-weak readout that did not allow to appreciate the signal-lowering when increasing MTX amounts were tested, hence, it was excluded. Regarding the two other conditions, I found no difference in the achieved spot, most probably due to the saturation of the signal; hence, to save reagents, I selected 1 nM as the best conjugate concentration.

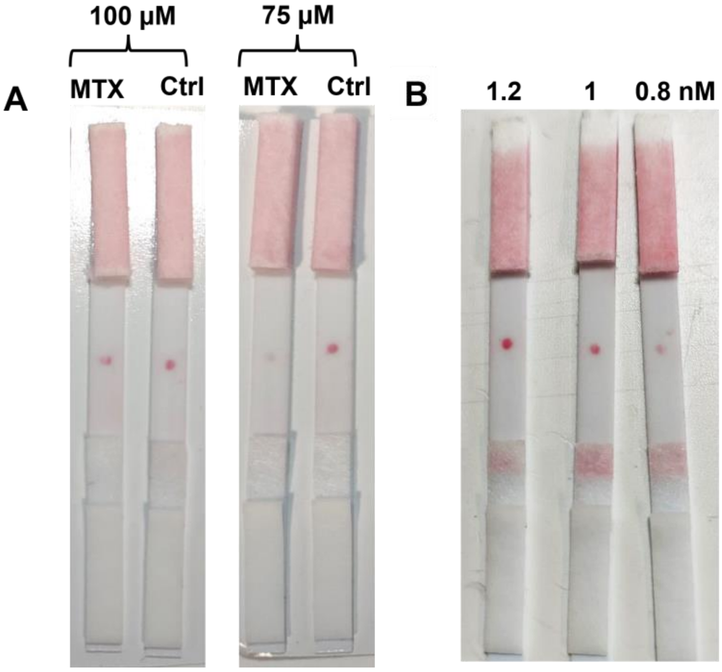

Figure 79. A) Comparison of the LFA performance with water (ctrl) and a 250 µM solution of MTX (MTX), when 100 and 75 µM folic acid were used for the preparation of the conjugate; B) performance of the assay with different conjugate concentrations (reported in the upper part of the image).

I further optimized the conjugate functionalizing the pad with a buffering agent. Indeed, the conjugate pad buffer should maximize the particles' stability and completely release them upon re-wetting by the sample[23]. When I tested conjugate pads with no buffering agents, the nitrocellulose membrane resulted very dirty (see fig.80A). Therefore, I treated the pad with a proper buffer before folic acid-AuNPs deposition. I opted for a 10 mM borate buffer to lower the ionic strength of the solution, which naturally increases during the drying process, improving the overall stability of the colloidal suspension of NPs. Then, I solved a solution of sucrose, BSA, and tween in the buffer, to promote the re-solubilization of the conjugate upon wetting and reducing the aspecific bonds across the membrane. I first functionalized the pads with the buffering solution and then, after a drying process, I deposited the conjugate on them. The performance of the LFA with the as-prepared conjugate pads is illustrated in fig.80B. The running membrane appeared remarkably cleaner compared to non-buffered conditions(fig.80A). BSA and Tween facilitated the flow of the label molecules along the membrane, improving the overall performance of the LFD. Furthermore, by adding these agents to the conjugate pad, the treatment of the sample pad was not required, reducing the number of steps needed for the fabrication of the device.

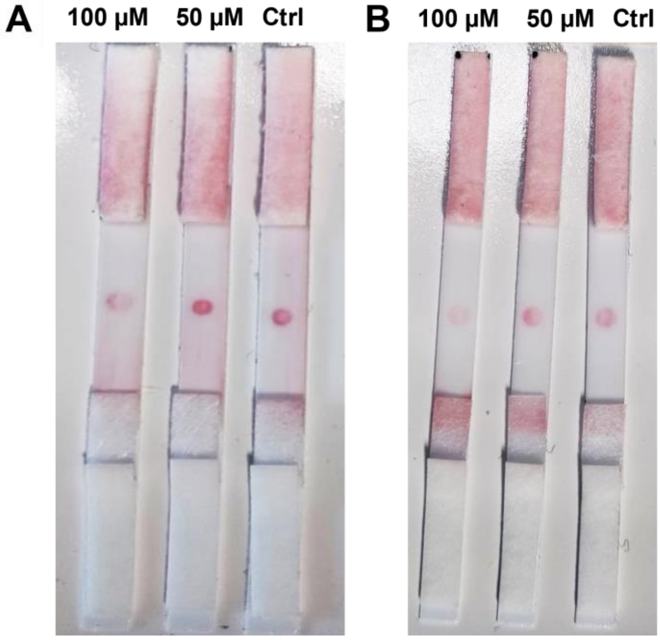

Figure 80. Comparison of the performance of the LFA with non-buffered conjugate pads (A) and pads treated with sucrose, BSA, and Tween in borate buffer (B). MTX concentrations tested are reported in the upper part of the images (100-50-0 µM).

5.4.4 Optimization of the capture probe

Regarding the capture probe, I tested how the solvent used for diluting the stock solution of the enzyme (1 mg/mL) and its concentration affected the signal readout. As illustrated in fig.81, I solved hDHFR in water (A) and in 100 mM phosphate buffer saline (PBS) (B), reaching a final concentration of 0.5 mg/mL. I compared the performance of the devices prepared with the two t-lines, fluxing water. The experimental result indicated that PBS allowed for a more intense and brighter spot compared to water, likely due to a better immobilization or a promoted interaction of the enzyme with the conjugate during the flow.

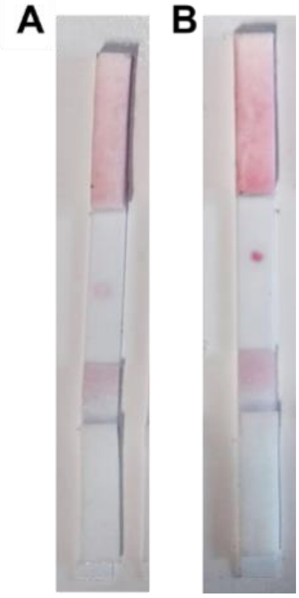

Figure 81. Comparison of the performance of the LFDs realized with the capture probe solved in water (A) and PBS (B).

To further optimize the capture probe, I tested different enzyme concentrations, preparing serial dilutions in PBS. I compared the intensity of the signal in the control conditions (with water). Specifically, I prepared three different t-lines: 1 mg/mL (stock solution), 0.5 mg/mL, and 0.25 mg/mL. As illustrated in fig.82, the lower concentration provided a too-weak signal and, according to the considerations I made previously for the conjugate solution, I excluded this condition. On the contrary, both the other tested concentrations showed a clear and well-defined signal, with no differences in intensity. For instance, I selected 0.5 mg/mL intending to save reagents and decrease the overall cost of the device.

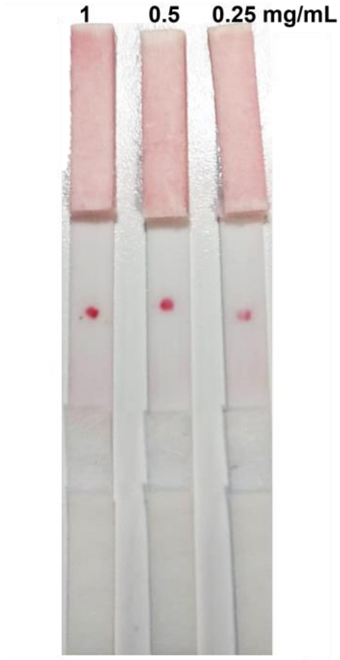

Figure 82. Comparison of the performance of the devices treated with different concentrations of the capture probe (reported in the upper part of the image).

5.4.5 Optimization of the assay performance

Finally, to further improve the sensitivity of the test, I introduced a blocking agent into the conjugate. In competitive assays, by reducing the concentration of the competitive molecule (i.e. folic acid), the detection limit decreases. The use of blocking agents like BSA or polyethylene glycol, promotes the stabilization of the conjugate covering the NP surface (protein-corona formation) and enabling to decrease the concentration of folic acid[223]. With this aim, I incubated AuNPs with a decreased concentration of folic acid (50 µM) and then I added 0.06% of BSA in the conjugate. As illustrated in fig.83, I compared the performance of the devices, treated with and without BSA (with 75 µM of folic acid in the conjugate), when a control solution and 100 µM MTX were tested. As it is depicted in the figure, a further improvement of the sensitivity was achieved since the signal produced with 100 µM MTX showed a clear intensity decrease when BSA blocking was performed.

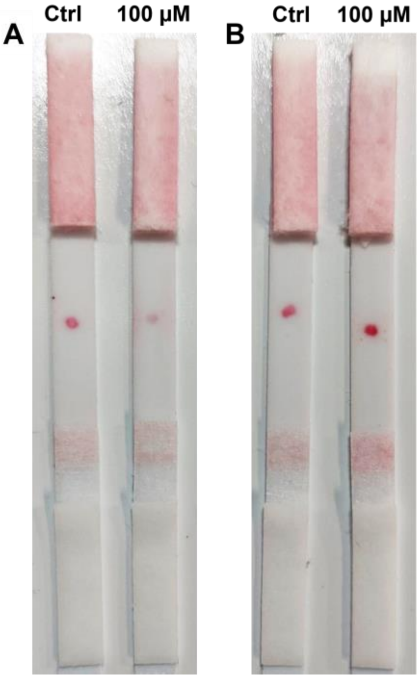

Figure 83. Devices tested with water (ctrl) and 100 µM solution of MTX with (A) and without (B) the blocking of the conjugate with BSA.

5.4.6 Analytical performance

Finally, after all the assay optimizations, I tested the analytical performance of the proposed device for the detection of MTX, aiming to establish the visual LoD (defined as the capacity of the human eye to distinguish the decrease in the signal intensity). I tested the LFDs with decreasing MTX concentrations (250, 100, 50, 0 µM). As it is shown in fig.84, the signal produced followed a linear trend with an intensity increase as the MTX concentrations decreased, confirming the competition between the target molecule and the folic acid.

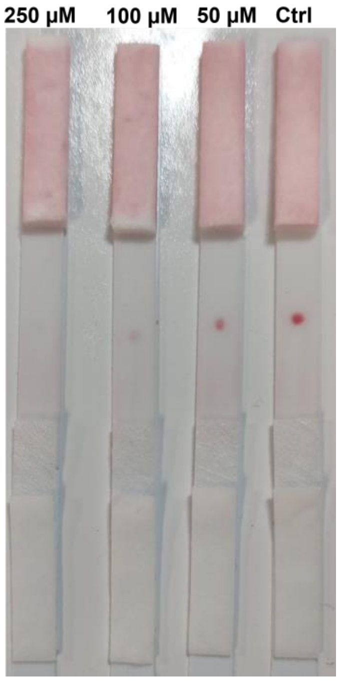

Figure 84. Proposed LFDs treated with decreasing MTX concentrations (reported in the upper part of the image).

Although this result paves the way for the on-site and rapid detection of MTX contamination, experiments are still ongoing to further improve the LoD and the device’s overall efficiency.

5.5 Materials and methods

5.5.1 Chemicals

The chemicals employed for this project were of high technical grade and used without further purification. All solutions and buffers were prepared using ultrapure deionized water (MilliQ). Hydrogen tetrachloroaurate ($HAuCl_4$) and hydroxylamine sulfate were purchased from Alfa Aesar. Trisodium citrate, methotrexate, dihydrofolate reductase human, folic acid, sodium tetraborate decahydrate, boric acid, ethanol, phosphate buffered saline tablet, bovine serum albumin, Tween-20, were purchased from Merck (Sigma-Aldrich).

Sample pad (grade 319, composition Cotton Fibers), conjugate pad (grade 8980, composition Chopped Glass w/Binder), and absorbent pad (grade 440, composition Cotton/Glass Blend) were purchased from Ahlstrom-Munksjö. Running pad Unisart® nitrocellulose membrane (CN95) was purchased from Sartorius.

5.5.2 Instrumentation

Dynamic Light Scattering (DLS) Malvern Panalytical, Transmission Electron Microscope JOEL JEM 1400, NanoDrop® (wavelength Accuracy ± 1 nm, absorbance accuracy 3 % at 0.74 Abs@350nm) Thermo Fisher, Ocean Optics Spectrophotometer with OCE-HDX-XR detector.

5.5.3 Synthesis of 35 nm AuNPs

The synthesis of colloidal 35nm AuNPs relies on the seeded growth of 15nm AuNPs (synthesized following the protocol described in chapter 2, "Materials and methods", paragraph "Synthesis of 15 nm AuNPs). All the glassware and the magnetic stir-bar were washed with aqua regia ($HCl:HNO_3$ 3:1). In a round-bottom flask, under vigorous stirring and at room temperature, 1 mL of seeds were diluted into 120 mL of MilliQ water. Then 0.4 mL of 0.1 M hydroxylamine sulfate solution was introduced into the solution, followed by the addition of 10 mL of 2 mM aqueous solution of $HAuCl_4$ drop by drop. Finally, 2.65 mL of 0.1 M trisodium citrate solution was added, acting as stabilizing agent. The last step concerned the concentration of AuNPs and the removal of unreactive reagents obtained by centrifugation in a 50 mL polycarbonate tube at 3800 rcf, for 25 minutes. The pellet was collected and stored at 4°C, until use.

5.5.4 Characterization of 35 nm AuNPs

The prepared AuNPs were characterized using UV-vis spectroscopy, TEM, and DLS. Particularly, 600 µL of the synthesized AuNPs diluted to a concentration of about 2 nM in water were spectrophotometrically read through a disposable polystyrene cuvette. For the TEM analysis, 3 µL of 2 nM MGNPs suspension were placed on oxygen plasma cleaned grid. Finally, the DLS reading was obtained placing 600 µL of 2 nM AuNPs suspension in a disposable polystyrene cuvette and performing 3 measurements consisting of 11 runs (see fig. 77).

5.5.5 Lateral flow device assembly

The LF device was composed of the sample pad (15 mm × 4 mm), the conjugate pad (9 mm × 4 mm), the strip of nitrocellulose (25 mm × 4 mm), and the absorbent pad (18 mm × 4 mm). Regarding the functionalization of the different components of the LFD, the sample pad and absorbed pad were not treated. On the contrary, a solution of 10 % sucrose, 0.1 % BSA, and 0.5 % Tween in borate buffer 100 mM were deposited on the conjugate pads and they were put under vacuum for two hours. Comparative experiments with no-treated conjugate pads were performed avoiding this step of functionalization. Meanwhile, the conjugate solution was prepared: the folic acid powder was dissolved in a 1 M solution of NaOH and further dilutions were made in a 100 mM of Na_2HPO_4 solution. Then, in a 4 mL glass vial, under gently stirring, 1 mL of 75 µM (60 µM, or 100 µM for optimization assays) folic acid was introduced, followed by the addition of 60 µL of 5 nM AuNPs 35 nm Ø, dropwise. Experiments to prove the aggregation of the AuNPs were performed by solving folic acid in ethanol. The as-prepared solution was incubated for one hour. Then 0.06 % BSA was introduced in the vial, and the conjugate solution (with 60 µM folic acid) was left for thirty minutes under stirring. Experiments without BSA blocking were performed avoiding this blocking step. To remove the excess of folic acid and to concentrate the conjugate, the prepared solution was centrifugated at 8000 rcf, for 10 minutes at 4 °C. Afterwards, I recorded the absorbance of the pellet, and I diluted it to 1 nM (or 0.8, or 1.2 nM for optimization assays) in MilliQ water before functionalizing the buffered conjugate pads with 17 µL of the as-prepared solution. I put the pads under vacuum for three hours to allow the complete dry. Meanwhile, the running pads were functionalized with the capture probe: the stock solution of the enzyme hDHFR (1 mg/mL) was diluted 1:2 (or 1:4 for optimizations assays) in 10 mM solution of PBS, and 0.6 µL of it was deposited on the pad, in the middle of the strip. The running pad was dried overnight at room temperature to ensure the stable immobilization of the capture bioreceptor. The pads, separately functionalized, were assembled on a laminated card, with a partial overlap of 2 mm, and, hence, the final dimension of the device was 60 mm × 4 mm.

5.5.6 Assay procedure

For the performance of the device, I placed on the sample pad three subsequent drops of 25 µL of MTX, previously solved in a 1 M solution of NaOH and diluted at the desired concentration in MilliQ water. Negative controls were obtained by treating the device with MilliQ water. The first two depositions of the sample (50 µL) were added successively, while a delay of about one minute was required for the last 25 µL to avoid overflow. The sample with conjugate solution took about 5 minutes to reach the end of the strip, leaving the membrane clean. The control signal was immediately visualized by a vivid red dot in the t-line, due to AuNPs stopping there. On the contrary, when MTX solutions were tested, the intensity of the signal became dimmer.

5.6 Conclusions

In conclusion, I developed a POC device in an LF configuration to detect MTX contaminations on working surfaces, aiming to improve healthcare workers' safety. The sensing strategy avoided the use of anti-MTX antibodies which present high costs and are not easily available. On the contrary, I exploited the pharmacological interaction between the drug and the target enzyme, namely DHFR. The detection mechanism relied on the competition between MTX and its analog folic acid for the DHFR, which I used as the capture probe and I immobilized in the test zone. The visual readout was provided by spherical 35 nm AuNPs that I functionalized with folic acid in the conjugate pad. The DHFR probe selectively recognized folic acid, allowing the accumulation of AuNPs on the test line, and resulting in a red dot. In case MTX was present in the sample, it bound the enzyme leaving fewer sites available for the interaction with folic acid-AuNPs, thus resulting in a visible intensity decrease. The signal completely disappeared when very high MTX concentrations were tested.

The assay for the detection of MTX was finely optimized with respect to the conjugate concentration and the solvent used. It was found that ethanol induced the aggregation of AuNPs, while a lower amount of folic acid in the conjugate enabled a higher sensitivity due to the lower saturation of the signal. Moreover, the functionalization of the conjugate pads with buffering agents promoted the even flow of the label molecules, allowing for a more defined colored spot. Some optimizations concerning the capture molecule were performed in terms of concentration of the enzyme and diluting solvent, finding that 0.5 mg/mL of DHFR solved in PBS provided the best-defined spot. In conclusion, I further improved the sensitivity of the assay by introducing BSA as the blocking agent of the conjugate, obtaining an improved visual LoD with respect to the non-treated conjugate solution.

After all the optimizations, the analytical performance of the device was evaluated to determine the sensitivity of the assay. I tested decreasing MTX concentrations, and I found that the signal started to weaken down to a concentration of 100 µM. Although this result is above the clinically relevant value detected in environmental samples, it represents a starting point for on-site, rapid, and instrument-free MTX assessment. The experiments to further increase the sensitivity of the assay are still ongoing.

CONCLUSIONS AND OUTLOOKS

In this thesis, I presented the design, development, and validation of several POCTs for the early diagnosis of prognostic biomarkers and the on-site and instrument-free detection of anticancer drug contaminations in healthcare facilities. POC devices represent a technological advancement over traditional analytical techniques, enabling real-time and near-patient/on-site results, which can improve healthcare management or provide timely information about workers' exposure to toxic agents.

Nowadays diabetes is one of the most widespread pathologies in the world and patient self-management is the most useful tool to control glycemia and improve therapeutic success. Glucose level is generally measured through electrochemical blood sensors, which require a finger prick, involving physical discomfort and the possibility of bloodborne viral pathogens transmission. Non-invasive sampling techniques and continuous monitoring are highly required. With this aim, I developed a salivary glucose platform that provided a 15-minute colorimetric result exploiting the sensitive plasmonic properties of a particular nanoscale architecture of AuNPs. The integration of AuNPs in the sensing strategy enabled to boost the assay performance, improving the LoD to the glucose salivary concentrations, which are > one order of magnitude lower than those in the blood, whilst providing a naked-eye result. The detection mechanism relied on the glucose-dependent reshaping of multibranched AuNPs (MGNPs), characterized by several small tips. Hydrogen peroxide, produced by glucose oxidation, in presence of a halogen, could chemically etch the gold atoms on the NP surface and promoted their further rearrangement on the surface concavities. This chemical process was followed by a morphological change into a spherical shape with a consequent plasmonic shift and a visual color change from blue to pink, with a negligible optical density loss. This strategy proved reliability and high sensitivity when applied in the saliva medium thanks to the biomolecular corona formation. The assay was tuned to give a predictive ON-OFF signal only in the case of concentrations above the established non-physiological level corresponding to 4 mg/dL. The sensing strategy was successfully transferred on solid support after the immobilization of all the reagents on the substrate. The as-prepared device showed stability and reproducibility for up to six months, paving the way for the realization of a home-testing dipstick prototype. The calculated LoD was down to 1.4 mg/dL and the performance of the device was validated on real clinical samples of diabetic patients, confirming great reliability and real applicability. By implementing the colorimetric read-out with an automatized reading through machine learning algorithms it would be possible to correlate the color change with the glucose concentration, achieving a semiquantitative analysis and facilitating the interpretation of the test result by the users.

The sensing platform described above can be easily applied for the detection of several other analytes that, as for the glucose, can be oxidized by the specific enzyme enabling the reshaping of MGNPs. Moreover, the simultaneous detection of different prognostic biomarkers in one single analysis appears very promising not only to save reagents, money, and time but also to improve the clinical value of the test. With this aim, exploiting the interesting features of microfluidics, I developed a paper-based point-of-care testing for the simultaneous detection of three prognostic salivary biomarkers, based on the reshaping of plasmonic MGNPs. The proposed device, from a single drop of saliva, enabled to assess if the concentration of targets exceeds the pathological threshold. The three proposed analytes were glucose, cholesterol, and lactate, which are model biomarkers of clinical relevance involved in some metabolic processes of our bodies. The design of the device was realized with AutoCAD and included a main central area for the sample deposition and three microfluidic channels to split the sample, enabling the analysis of the three targets independently. The pattern was transferred on a paper sheet through a CO_2 laser cutter, which allowed, in a single step and without additional solvents, to realize 12 devices in less than 1 minute. The reshaping process was finely tuned in each branch to give an ON/OFF signal appreciable by the naked-eye. Further analysis of the colored spot obtained by acquiring smartphone images and recording red coordinate variations in the RGB space, allowed to better appreciate the color change. A higher pathological threshold of clinical importance was assessed for glucose and lactate assay, characterized by faster reshaping kinetics. The strategy showed excellent selectivity toward each analyte and multiplexing ability, with negligible interference by other salivary species. I finally realized a PVC mask in which I embedded the paper-based device, which provided the system robustness and handling to be used by non-skilled operators at home. The developed multiplexed device could be further improved implementing the number of targets to be investigated and, consequently, designing additional microfluidic branches. By increasing the number of the detection analytes, the users will receive more comprehensive and complete information about their health status.

POCT can be also a promising tool in working places where anticancer drugs are handled. These antiblastic agents present severe side effects, and it has been reported that, despite the use of protective equipment, there is a high risk for the staff to be exposed to these substances during their preparation and administration, leading to potential toxic effects. Trace amounts of the drugs have been found in the staff's urine samples and by monitoring the environmental contamination. However, the reference analytical techniques rely on costly and complex instrumentation and time-consuming procedures, which are not compatible with continuous drug monitoring. Therefore, I developed POC devices in an LF configuration for the assessment of the contamination by two widely employed cytotoxic drugs.

First, I focused on doxorubicin, which belongs to the anthracycline family and is used against a huge range of tumors, but it is also characterized by a variety of side effects like nausea, vomiting, myelosuppression, and severe cardiotoxicity. The sensing strategy that I proposed relied on an LF device with some remarkable innovations. For the visual readout of the signal, I exploited the intrinsic fluorescence of the molecule, without resorting to conventional label molecules like plasmonic NPs. Doxorubicin, indeed, when excited by UV light, emits an orange-red fluorescence that can be visualized by the naked-eye stopping. An additional novelty concerned the recognition mechanism since the use of an antibody, like in conventional LFD, was hampered by the lack of anti-doxorubicin antibodies or by their high costs. Hence, I exploited the pharmacological intercalation of the drug in dsDNA, used as the capture biomolecule in the LFD device. If present in the sample, doxorubicin flowed through the running pad, intercalated with the nucleotide probe deposited in the test region, remained captured, and was visualized as a fluorescent dot. The dsDNA was successfully immobilized by exploiting an electrostatic interaction between the negatively charged phosphate groups of the dsDNA and a positively charged membrane used as the running pad and further promoted using a short 3’overhang sequence as the capture probe. This is a novel strategy since nucleic acid-based LFAs normally rely on aptamer or single-strand DNA for hybridization-based platforms. After optimizing the running pad, the capture probe, and the running buffer, the analytical performance of the novel LFD was tested providing a visual LoD down to 4 ng; further image analyses of the colored spot, achieved by collecting green coordinates, revealed that the measured LoD was 1.5 ng. This sensitivity was comparable and even superior to other laboratory-based techniques. In conclusion, I adapted the platform to real urine, after diluting the sample 1:10 aiming to reduce the interference of urinary salts, whilst avoiding complex pretreatment procedures to maintain the POC concept of the device. The achieved visual LoD of 80 ng fell within the clinically relevant values, demonstrating great feasibility for the on-site, simple, and fast detection of healthcare workers’ exposure to doxorubicin. Additional insights into the complexity of the urine sample would be necessary to reduce the matrix effect and increase the sensitivity of the assay aiming to enhance the clinical value of the sensor.

The second LFA that I developed was designed for the detection of methotrexate (MTX). MTX is an unreactive analog of folic acid, inhibiting the enzyme dihydrofolate reductase (DHFR), involved in the DNA precursors’ synthesis. MTX’s main side effects are myelosuppression and pancytopenia, and strict control of environmental contamination is crucial. As for doxorubicin, anti-MTX antibodies are unfavorable both for their high costs and for their limited availability, and, hence, a novel approach was introduced. The proposed strategy relied on the pharmacological competition between folic acid and MTX for the same binding enzyme, immobilized as the capture probe in the test line, namely DHFR. 35 nm AuNPs were exploited as label molecules for their remarkable plasmonic properties, and they were conjugated with folic acid in the conjugate pad, finely optimizing the solution conditions before the immobilization. The sample containing MTX was deposited on the sample pad and exploiting the capillary forces, flowed through the running pad, binding the capture enzyme and hampering the conjugate to accumulate in the test zone. The signal intensity decreased in an MTX concentration-dependent manner. The visual LoD was improved by introducing a BSA blocking of the conjugate, and, after all the optimizations related to the enzyme and the buffering conditions, the sensitivity was ca. 100 µM. Although this result is far from the clinically relevant concentration range, it is a preliminary achievement and experiments are still ongoing. Furthermore, similarly to the doxorubicin sensor, it would be interesting to apply the proposed LFD to real urine samples aiming to realize a valuable tool for monitoring the healthcare workers’ exposure to MTX in non-invasive fluids.

Our interest in providing POC devices for real applications both for healthcare diagnostics and for monitoring workers’ exposure to toxic drugs is driving collaborations with industrial partners, such as INAIL, highly interested in investigating novel technologies for diagnostic solutions.

BIBLIOGRAPHY

1. Pepe, M.S.; Etzioni, R.; Feng, Z.; Potter, J.D.; Lou, M.; Thornquist, M.; Winget, M.; Yasui, Y.; Ntroduction, I. Phases of Biomarker Development for Early Detection of Cancer OF. **2001**, *93*, 1054–1061.

2. Nestor, P.J.; Scheltens, P.; Hodges, J.R. Advances in the early detection of Alzheimer ' s disease. **2004**, 34–41, doi:10.1038/nm1433.

3. Herman, W.H.; Ye, W.; Griffin, S.J.; Simmons, R.K.; Davies, M.J.; Khunti, K.; Rutten, G.E.H.M.; Sandbaek, A.; Lauritzen, T.; Borch-Johnsen, K.; et al. Early detection and treatment of type 2 diabetes reduce cardiovascular morbidity and mortality: A simulation of the results of the Anglo-Danish-Dutch study of intensive treatment in people with screen-detected diabetes in primary care (ADDITION-Europe). *Diabetes Care* **2015**, *38*, 1449–1455, doi:10.2337/dc14-2459.

4. St-Louis, P. Status of point-of-care testing: Promise, realities, and possibilities. *Clin. Biochem.* **2000**, *33*, 427–440, doi:10.1016/S0009-9120(00)00138-7.

5. Jung, W.; Han, J.; Choi, J.W.; Ahn, C.H. Point-of-care testing (POCT) diagnostic systems using microfluidic lab-on-a-chip technologies. *Microelectron. Eng.* **2015**, *132*, 46–57, doi:10.1016/j.mee.2014.09.024.

6. Gubala, V.; Harris, L.F.; Ricco, A.J.; Tan, M.X.; Williams, D.E. Point of care diagnostics: Status and future. *Anal. Chem.* **2012**, *84*, 487–515, doi:10.1021/ac2030199.

7. Yang, S.; Lv, S.; Zhang, W.; Cui, Y. A Review of Opportunities and Challenges. **2022**.

8. Shahrivar, K.; Del Giudice, F. Controlled viscoelastic particle encapsulation in microfluidic devices. *Soft Matter* **2021**, *17*, 8068–8077, doi:10.1039/d1sm00941a.

9. Carrell, C.; Kava, A.; Nguyen, M.; Menger, R.; Munshi, Z.; Call, Z.; Nussbaum, M.; Henry, C. Microelectronic Engineering Beyond the lateral fl ow assay : A review of paper-based micro fl uidics. **2019**, *206*, 45–54, doi:10.1016/j.mee.2018.12.002.

10. San Park, T., Baynes, C., Cho, S. I., & Yoon, J. Y. (2014). Paper microfluidics for red wine tasting. Rsc Advances, 4(46), 24356-24362..

11. Shangguan, J.; Liu, Y.; Pan, J.; Xu, B. Lab on a Chip. **2017**, 120–127, doi:10.1039/c6lc01250g.

12. Renault, C.; Koehne, J.; Ricco, A.J.; Crooks, R.M. Three-Dimensional Wax Patterning of Paper Fluidic Devices. **2014**.

13. Yamada, K.; Henares, T.G.; Suzuki, K.; Citterio, D. Paper-based inkjet-printed microfluidic analytical devices. *Angew. Chemie - Int. Ed.* **2015**, *54*, 5294–5310, doi:10.1002/anie.201411508.

14. Pandey, C.M.; Augustine, S.; Kumar, S.; Kumar, S.; Nara, S.; Srivastava, S.; Malhotra, B.D. Microfluidics Based Point-of-Care Diagnostics. *Biotechnol. J.* **2018**, *13*, 1–11, doi:10.1002/biot.201700047.

15. Nie, J.; Liang, Y.; Zhang, Y.; Le, S. One-step patterning of hollow microstructures in paper by laser cutting to create micro fl uidic analytical devices †. **2013**, 671–676, doi:10.1039/c2an36219h.

16. Pollock, N.R.; Rolland, J.P.; Kumar, S.; Beattie, P.D.; Jain, S.; Noubary, F.; Wong, V.L.; Pohlmann, R.A.; Ryan, U.S.; Whitesides, G.M. A paper-based multiplexed transaminase test for low-cost, point-of-care liver function testing. *Sci. Transl. Med.* **2012**, *4*, doi:10.1126/scitranslmed.3003981.

17. Li, F.; Wang, X.; Liu, J.; Hu, Y.; He, J. Double-layered microfluidic paper-based device with multiple colorimetric indicators for multiplexed detection of biomolecules. *Sensors Actuators,*

B Chem. **2019**, *288*, 266–273, doi:10.1016/j.snb.2019.02.116.

18. Parolo, C., & Merkoçi, A. (2013). based nanobiosensors for diagnostics. Chemical Society Reviews, 42(2), 450-457.

19. Grubb, A. O., & Glad, U. C. (1979). U.S. Patent No. 4,168,146. Washington, DC: U.S. Patent and Trademark Office.

20. Brangel, P.; Sobarzo, A.; Parolo, C.; Miller, B.S.; Howes, P.D.; Gelkop, S.; Lutwama, J.J.; Dye, J.M.; Mckendry, R.A.; Lobel, L.; et al. A Serological Point-of-Care Test for the Virus in Human Survivors. **2018**, doi:10.1021/acsnano.7b07021.

21. Anfossi, L.; Baggiani, C.; Giovannoli, C.; Arco, G.D. Lateral-flow immunoassays for mycotoxins and phycotoxins : a review. **2013**, 467–480, doi:10.1007/s00216-012-6033-4.

22. Luo, K.; Kim, H.; Oh, M.; Kim, Y. Paper-based lateral flow strip assay for the detection of foodborne pathogens : principles , applications , technological challenges and opportunities. *Crit. Rev. Food Sci. Nutr.* **2018**, *0*, 1–14, doi:10.1080/10408398.2018.1516623.

23. Parolo, C.; Sena-Torralba, A.; Bergua, J.F.; Calucho, E.; Fuentes-Chust, C.; Hu, L.; Rivas, L.; Álvarez-Diduk, R.; Nguyen, E.P.; Cinti, S.; et al. Tutorial: design and fabrication of nanoparticle-based lateral-flow immunoassays. *Nat. Protoc.* **2020**, *15*, 3788–3816, doi:10.1038/s41596-020-0357-x.

24. Xiao, Z.; Yang, Y.; Zhang, X.; Guo, W. Controlling capillary flow rate on lateral flow test substrates by tape. *Micromachines* **2021**, *12*, 1–11, doi:10.3390/mi12050562.

25. Koczula, K.M.; Gallotta, A. Lateral flow assays. **2016**, 111–120, doi:10.1042/EBC20150012.

26. Ferrigno, P.K. Non-antibody protein-based biosensors Affimer binders and peptide aptamers in biosensing. **2016**, 19–25, doi:10.1042/EBC20150003.

27. Wang, Y.; Wang, L.; Xue, J.; Dong, J.; Cai, J.; Hua, X.; Wang, M.; Zhang, C.; Liu, F. Signal-amplified lateral flow test strip for visual detection of Cu2+. *PLoS One* **2017**, *12*, 1–13, doi:10.1371/journal.pone.0169345.

28. Javadi-zarnaghi, A.J.F. Development of a colorimetric nucleic acid-based lateral flow assay with non-biotinylated capture DNA. *Appl. Biol. Chem.* **2017**, *60*, 637–645, doi:10.1007/s13765-017-0321-9.

29. Park, J.S.; Kim, S.; Han, J.; Kim, J.H.; Park, K.S. Sensors and Actuators : B . Chemical Equipment-free , salt-mediated immobilization of nucleic acids for nucleic acid lateral flow assays. *Sensors Actuators B. Chem.* **2022**, *351*, 130975, doi:10.1016/j.snb.2021.130975.

30. Wang, L.; Ma, W.; Chen, W.; Liu, L.; Ma, W.; Zhu, Y.; Xu, L.; Kuang, H.; Xu, C. An aptamer-based chromatographic strip assay for sensitive toxin semi-quantitative detection. *Biosens. Bioelectron.* **2011**, *26*, 3059–3062, doi:10.1016/j.bios.2010.11.040.

31. Huang, H.; Zhu, P.; Zhou, C.; He, S.; Yan, X. The development of loop-mediated isothermal amplification combined with lateral flow dipstick for detection of Karlodinium veneficum. **2017**, *62*, 20–29, doi:10.1016/j.hal.2016.11.022.

32. Tokel, O.; Inci, F.; Demirci, U. Advances in Plasmonic Technologies for Point of Care Applications. **2014**.

33. Roduner, E. Size matters : why nanomaterials are different. **2006**, 583–592, doi:10.1039/b502142c.

34. Chen, G.; Roy, I.; Yang, C.; Prasad, P.N. Nanochemistry and Nanomedicine for Nanoparticle-based Diagnostics and Therapy. **2016**, doi:10.1021/acs.chemrev.5b00148.

35. Zhang, Z.; Wang, H.; Chen, Z.; Wang, X.; Choo, J. Biosensors and Bioelectronics Plasmonic colorimetric sensors based on etching and growth of noble metal nanoparticles : Strategies and applications. *Biosens. Bioelectron.* **2018**, *114*, 52–65, doi:10.1016/j.bios.2018.05.015.

36. Rao, H.; Xue, X.; Wang, H.; Xue, Z. Gold nanorod etching-based multicolorimetric sensors: strategies and applications. *J. Mater. Chem. C* **2019**, *7*, 4610–4621, doi:10.1039/C9TC00757A.

37. Chakraborty, I.; Feliu, N.; Roy, S.; Dawson, K.A.; Parak, W.J. Protein-Mediated Shape-Control of Silver Nanoparticles Protein-Mediated Shape-Control of Silver Nanoparticles. **2018**, doi:10.1021/acs.bioconjchem.8b00034.

38. Online, V.A. A plasmonic blood glucose monitor based on enzymatic etching of gold nanorods †. **2013**, 1856–1858, doi:10.1039/c3cc38476d.

39. Kermanshahian, K.; Yadegar, A.; Ghourchian, H. Gold nanorods etching as a powerful signaling process for plasmonic multicolorimetric chemo- / biosensors : Strategies and applications. *Coord. Chem. Rev.* **2021**, *442*, 213934, doi:10.1016/j.ccr.2021.213934.

40. Liu, X.; Atwater, M.; Wang, J.; Huo, Q. Extinction coefficient of gold nanoparticles with different sizes and different capping ligands. **2007**, *58*, 3–7, doi:10.1016/j.colsurfb.2006.08.005.

41. Syedmoradi, L.; Daneshpour, M.; Alvandipour, M.; Gomez, F.A.; Hajghassem, H.; Omidfar, K. Biosensors and Bioelectronics Point of care testing : The impact of nanotechnology. **2017**, *87*, 373–387, doi:10.1016/j.bios.2016.08.084.

42. Shariati, S., & Khayatian, G. (2020). Microfluidic paper-based analytical device using gold nanoparticles modified with N, N′-bis (2-hydroxyethyl) dithiooxamide for detection of Hg (ii) in air, fish and water samples. New Journal of Chemistry, 44(43), 18662-18667.

43. Sajid, M.; Daud, M. Designs , formats and applications of lateral flow assay : A literature review. *J. Saudi Chem. Soc.* **2015**, *19*, 689–705, doi:10.1016/j.jscs.2014.09.001.

44. Wen, T.; Huang, C.; Shi, F.; Zeng, X.; Lu, T.; Ding, S.; Jiao, Y. Development of a lateral fl ow immunoassay strip for rapid detection of IgG antibody against. **2020**, 5345–5352, doi:10.1039/d0an00629g.

45. Pedone, D.; Moglianetti, M.; Lettieri, M.; Marrazza, G.; Pompa, P.P. Platinum Nanozyme-Enabled Colorimetric Determination of Total Antioxidant Level in Saliva. *Anal. Chem.* **2020**, *92*, 8660–8664, doi:10.1021/acs.analchem.0c01824.

46. Lei, J.; Ju, H. Chem Soc Rev Signal amplification using functional nanomaterials for biosensing. **2012**, 2122–2134, doi:10.1039/c1cs15274b.

47. Alharbi, K.K.; Al-sheikh, Y.A. Role and implications of nanodiagnostics in the changing trends of clinical diagnosis. *Saudi J. Biol. Sci.* **2014**, *21*, 109–117, doi:10.1016/j.sjbs.2013.11.001.

48. Kievit, F.M.; Zhang, M. Surface Engineering of Iron Oxide Nanoparticles for Targeted Cancer Therapy. **2011**, *44*, 853–862.

49. Ray, P.; Ph, D.; Manach, Y. Le; Riou, B.; Ph, D.; Houle, T.T.; Ph, D. Statistical Evaluation of a Biomarker. **2010**, 1023–1040.

50. Heikenfeld, J.; Jajack, A.; Feldman, B.; Granger, S.W.; Gaitonde, S.; Begtrup, G.; Katchman, B.A. Accessing analytes in biofluids for peripheral biochemical monitoring. *Nat. Biotechnol.* **2019**, *37*, 407–419, doi:10.1038/s41587-019-0040-3.

51. Boselli, L.; Pomili, T.; Donati, P.; Pompa, P.P. Nanosensors for visual detection of glucose in biofluids: Are we ready for instrument-free home-testing? *Materials (Basel).* **2021**, *14*, doi:10.3390/ma14081978.

52. Zhang, X.; Sucre-rosales, E.; Byram, A.; Hernandez, F.E.; Chen, G. Ultrasensitive Visual Detection of Glucose in Urine Based on the Iodide-Promoted Etching of Gold Bipyramids. **2020**, doi:10.1021/acsami.0c16369.

53. Clinica, B.; Cattolica, U.; Otorinolaringoiatria, I.; Cagliari, U. Potential applications of human saliva as diagnostic fluid. **2011**, 347–357.

54. Press, D. Glucose estimation in the salivary secretion of diabetes mellitus patients. **2012**, 149–

154.

55. Cui, Y.; Zhang, H.; Zhu, J.; Liao, Z.; Wang, S.; Liu, W. Correlations of Salivary and Blood Glucose Levels among Six Saliva Collection Methods. *Int. J. Environ. Res. Public Health* **2022**, *19*, 1–15, doi:10.3390/ijerph19074122.

56. Castro, L.F. De; Freitas, S.V. De; Duarte, L.C.; Souza, J.A.C. De; Paixão, T.R.L.C. Salivary diagnostics on paper microfluidic devices and their use as wearable sensors for glucose monitoring. **2019**, 4919–4928.

57. Ngamchuea, K.; Chaisiwamongkhol, K.; Batchelor-mcauley, C.; Compton, R.G. salivary biomarkers – a tutorial review. **2018**, 81–99, doi:10.1039/c7an01571b.

58. Trial, C. Defining the Relationship Between Plasma Glucose and HbA 1c. **2002**, *25*.

59. Soh, J.H.; Lin, Y.; Rana, S.; Ying, J.Y.; Stevens, M.M. Colorimetric Detection of Small Molecules in Complex Matrixes via Target-Mediated Growth of Aptamer-Functionalized Gold Nanoparticles. **2015**, doi:10.1021/acs.analchem.5b00875.

60. Marler-Hausen, T.; Holt, C.; Headley, C.; Sessink, P. Use of a closed-system drug transfer device reduces contamination with doxorubicin during bolus injection. *Br. J. Nurs.* **2020**, *29*, S15–S21, doi:10.12968/bjon.2020.29.10.S15.

61. Nussbaumer, S.; Bonnabry, P.; Veuthey, J.; Fleury-souverain, S. Talanta Analysis of anticancer drugs : A review. *Talanta* **2011**, *85*, 2265–2289, doi:10.1016/j.talanta.2011.08.034.

62. Smith, J.P.; Sammons, D.L.; Pretty, J.R.; Kurtz, K.S.; Robertson, S.A.; DeBord, D.G.; Connor, T.H.; Snawder, J.E. Detection of 5-fluorouracil surface contamination in near real time. *J. Oncol. Pharm. Pract.* **2016**, *22*, 396–408, doi:10.1177/1078155215585187.

63. Deshpande, A. D., Harris-Hayes, M., & Schootman, M. (2008). Epidemiology of diabetes and diabetes-related complications. Physical therapy, 88(11), 1254-1264.

64. American Diabetes Association. (2008). Standards of medical care in diabetes 2008. Diabetes care, 31, 12-54.

65. Yoo, E.; Lee, S. Glucose Biosensors: An Overview of Use in Clinical Practice. **2010**, 4558–4576, doi:10.3390/s100504558.

66. Thompson, N.D.; Perz, J.F. Eliminating the Blood: Ongoing Outbreaks of Hepatitis B Virus Infection and the Need for Innovative Glucose Monitoring Technologies. **2009**, *3*, 283–288.

67. Minimed, M.; City, R. Continuous Glucose Monitoring. **2005**, *28*.

68. Yadav, J.; Rani, A.; Singh, V.; Mohan, B. Biomedical Signal Processing and Control Prospects and limitations of non-invasive blood glucose monitoring using near-infrared spectroscopy. *Biomed. Signal Process. Control* **2015**, *18*, 214–227, doi:10.1016/j.bspc.2015.01.005.

69. Saasa, V.; Malwela, T.; Beukes, M.; Mokgotho, M.; Liu, C.; Mwakikunga, B. Sensing Technologies for Detection of Acetone in Human Breath for Diabetes Diagnosis and Monitoring. **2018**, 1–17, doi:10.3390/diagnostics8020012.

70. Lim, S.H.; Wei, J.; Lin, J.; Li, Q.; KuaYou, J. A glucose biosensor based on electrodeposition of palladium nanoparticles and glucose oxidase onto Nafion-solubilized carbon nanotube electrode. *Biosens. Bioelectron.* **2005**, *20*, 2341–2346, doi:10.1016/j.bios.2004.08.005.

71. Acetone, B. Review of Non-Invasive Glucose Sensing Techniques : **2020**.

72. Tae, S.G.; Su, M. As featured in : **2021**, doi:10.1039/d0nr06348g.

73. Gupta, S.; Nayak, M.T.; Jd, S.; Dawar, G.; Sinha, N.; Rallan, N.S. Correlation of salivary glucose level with blood glucose level in diabetes mellitus. **2017**, doi:10.4103/jomfp.JOMFP.

74. Elkington, D.; Belcher, W.J.; Dastoor, P.C.; Zhou, X.J. Detection of saliva-range glucose concentrations using organic thin-film transistors. **2015**, *043303*, doi:10.1063/1.4892012.

75. Song, Y.; Wei, W.; Qu, X. Colorimetric Biosensing Using Smart Materials., doi:10.1002/adma.201101853.

76. Links, D.A. Colorimetric assay for parallel detection of Cd 2+ , Ni 2+ and Co 2+ using peptide-modified gold nanoparticles †‡. **2012**, 601–607, doi:10.1039/c1an15909g.

77. Valentini, P.; Pompa, P.P. Gold nanoparticles for naked-eye DNA detection: Smart designs for sensitive assays. *RSC Adv.* **2013**, *3*, 19181–19190, doi:10.1039/c3ra43729a.

78. Bekdemir, A.; Chen, Q.; Bhatia, S.N.; Stevens, M.M. monitoring. **2020**, *14*, 883–890, doi:10.1038/s41565-019-0527-6.Renal.

79. Wu, B.; Hou, S.; Yin, F.; Li, J.; Zhao, Z. Amperometric glucose biosensor based on layer-by-layer assembly of multilayer films composed of chitosan , gold nanoparticles and glucose oxidase modified Pt electrode. **2007**, *22*, 838–844, doi:10.1016/j.bios.2006.03.009.

80. Cao, L.; Wang, P.; Chen, L.; Wu, Y.; Di, J. A photoelectrochemical glucose sensor based on gold nanoparticles as a mimic enzyme of glucose. **2019**, 15307–15313, doi:10.1039/c9ra02088h.

81. Saha, K., Agasti, S. S., Kim, C., Li, X., & Rotello, V. M. (2012). Gold nanoparticles in chemical and biological sensing. Chemical reviews, 112(5), 2739-2779.

82. Jv, Y.; Li, B.; Cao, R. Positively-charged gold nanoparticles as peroxidiase mimic and their application in hydrogen peroxide and glucose detection w. **2010**, 0–2, doi:10.1039/c0cc02698k.

83. Holzinger, M.; Goff, A. Le; Cosnier, S. Nanomaterials for biosensing applications : a review. **2014**, *2*, 1–10, doi:10.3389/fchem.2014.00063.

84. Detection, C.; Brain, R.; Gold, U. Colorimetric Detection of Glucose in Rat Brain Using Gold. **2010**, 4800–4804, doi:10.1002/anie.201001057.

85. Xiong, Y.; Zhang, Y.; Rong, P.; Yang, J.; Wang, W.; Liu, D. detection based on glucose oxidase-catalyzed. **2015**, *20*, 15584–15588, doi:10.1039/c5nr03758a.

86. Shape-altering, B.; Nanostars, G. Plasmonic Detection of Glucose in Serum Based on. **2019**.

87. Donati, P.; Moglianetti, M.; Veronesi, M.; Prato, M.; Tatulli, G.; Bandiera, T.; Pompa, P.P. Nanocatalyst/Nanoplasmon-Enabled Detection of Organic Mercury: A One-Minute Visual Test. *Angew. Chemie - Int. Ed.* **2019**, *201905669*, 10285–10289, doi:10.1002/anie.201905669.

88. Monopoli, M.P.; Åberg, C.; Salvati, A.; Dawson, K.A. identity of nanosized materials. *Nat. Nanotechnol.* **2012**, *7*, 779–786, doi:10.1038/nnano.2012.207.

89. Boselli, L.; Dawson, K.A. Nanoscale Horizons. **2017**, *2*, doi:10.1039/c6nh00219f.

90. Rodríguez-lorenzo, L.; Rica, R. De; Álvarez-puebla, R.A.; Liz-marzán, L.M.; Stevens, M.M. Plasmonic nanosensors with inverse sensitivity by means of enzyme-guided crystal growth. **2012**, 10–13, doi:10.1038/nmat3337.

91. Parak, W.J. Protein-Mediated Shape Control of Silver Nanoparticles. **2018**, doi:10.1021/acs.bioconjchem.8b00034.

92. Donati, P.; Pomili, T.; Boselli, L.; Pompa, P.P. Colorimetric Nanoplasmonics to Spot Hyperglycemia From Saliva. *Front. Bioeng. Biotechnol.* **2020**, *8*, 1–9, doi:10.3389/fbioe.2020.601216.

93. Zhang, Z.; Chen, Z.; Wang, S.; Cheng, F.; Chen, L. Iodine-Mediated Etching of Gold Nanorods for Plasmonic ELISA Based on Colorimetric Detection of Alkaline Phosphatase. *ACS Appl. Mater. Interfaces* **2015**, *7*, 27639–27645, doi:10.1021/acsami.5b07344.

94. Zhu, Q.; Wu, J.; Zhao, J.; Ni, W. Role of bromide in hydrogen peroxide oxidation of ctab-stabilized gold nanorods in aqueous solutions. *Langmuir* **2015**, *31*, 4072–4077, doi:10.1021/acs.langmuir.5b00137.

95. Cheng, X.; Huang, Y.; Yuan, C.; Dai, K.; Jiang, H.; Ma, J. Colorimetric detection of A-glucosidase activity based on the etching of gold nanorods and its application to screen anti-diabetic drugs. *Sensors Actuators, B Chem.* **2019**, *282*, 838–843, doi:10.1016/j.snb.2018.11.097.

96. Yuan, H.; Janssen, K.P.F.; Franklin, T.; Lu, G.; Su, L.; Gu, X.; Uji-I, H.; Roeffaers, M.B.J.; Hofkens, J. Reshaping anisotropic gold nanoparticles through oxidative etching: The role of the surfactant and nanoparticle surface curvature. *RSC Adv.* **2015**, *5*, 6829–6833, doi:10.1039/c4ra14237c.

97. Pastoriza-santos, I.; Rodrı, L.; Mazzucco, S.; Ste, O.; Kociak, M.; Liz-marza, L.M.; Garcı, F.J. Zeptomol Detection Through Controlled Ultrasensitive Surface-Enhanced Raman Scattering. **2009**, 4616–4618.

98. Xiong, Y.; Xia, Y. Shape-controlled synthesis of metal nanostructures: The case of palladium. *Adv. Mater.* **2007**, *19*, 3385–3391, doi:10.1002/adma.200701301.

99. Turkevich, J. Colloidal Gold . Part I. **1985**, 86–91.

100. Maiorano, G.; Rizzello, L.; Malvindi, A.; Shankar, S.; Martiradonna, L.; Falqui, A.; Paolo, P. Nanoscale Monodispersed and size-controlled multibranched gold nanoparticles with nanoscale tuning of surface morphology †. **2011**, 2227–2232, doi:10.1039/c1nr10107b.

101. Pompa, P.P.; Vecchio, G.; Galeone, A.; Brunetti, V.; Maiorano, G.; Sabella, S.; Cingolani, R. Nanoscale Physical assessment of toxicology at nanoscale : nano dose-metrics and toxicity factor. **2011**, 2889–2897, doi:10.1039/c1nr10233h.

102. Abikshyeet, P.; Ramesh, V.; Oza, N. Glucose estimation in the salivary secretion of diabetes mellitus patients. *Diabetes, Metab. Syndr. Obes. Targets Ther.* **2012**, *5*, 149–154, doi:10.2147/dmso.s32112.

103. Gabriel, E. F., Garcia, P. T., Cardoso, T. M., Lopes, F. M., Martins, F. T., & Coltro, W. K. (2016). Highly sensitive colorimetric detection of glucose and uric acid in biological fluids using chitosan-modified paper microfluidic devices. Analyst, 141(15), 4749-4756.

104. Price, C.P. Clinical review Point of care testing. **2001**, 1285–1288.

105. Vashist, S.K.; Luppa, P.B.; Yeo, L.Y.; Ozcan, A.; Luong, J.H.T. Emerging Technologies for Testing. *Trends Biotechnol.* **2015**, *33*, 692–705, doi:10.1016/j.tibtech.2015.09.001.

106. Cate, D.M.; Adkins, J.A.; Mettakoonpitak, J.; Henry, C.S. Recent Developments in Paper-Based Micro fl uidic Devices. **2015**.

107. Martinez, A.W.; Phillips, S.T.; Whitesides, G.M.; Carrilho, E. Diagnostics for the developing world: Microfluidic paper-based analytical devices. *Anal. Chem.* **2010**, *82*, 3–10, doi:10.1021/ac9013989.

108. Ren, K.; Zhou, J.; Wu, H. Materials for microfluidic chip fabrication. *Acc. Chem. Res.* **2013**, *46*, 2396–2406, doi:10.1021/ar300314s.

109. Yetisen, A.K.; Akram, M.S.; Lowe, C.R. Paper-based microfluidic point-of-care diagnostic devices. *Lab Chip* **2013**, *13*, 2210–2251, doi:10.1039/c3lc50169h.

110. Yamada, K.; Henares, T.G.; Suzuki, K.; Citterio, D. Paper-Based Inkjet-Printed Microfluidic Analytical Devices Angewandte. **2015**, 5294–5310, doi:10.1002/anie.201411508.

111. Martinez, A.W.; Phillips, S.T.; Butte, M.J.; Whitesides, G.M. Patterned paper as a platform for inexpensive, low-volume, portable bioassays. *Angew. Chemie - Int. Ed.* **2007**, *46*, 1318–1320, doi:10.1002/anie.200603817.

112. Bordbar, M.M.; Sheini, A.; Hashemi, P.; Hajian, A.; Bagheri, H. Disposable paper-based biosensors for the point-of-care detection of hazardous contaminations—a review. *Biosensors* **2021**, *11*, 1–51, doi:10.3390/bios11090316.

113. Nie, J.; Zhang, Y.; Lin, L.; Zhou, C.; Li, S.; Zhang, L.; Li, J. Low-Cost Fabrication of Paper-Based Micro fl uidic Devices by One- Step Plotting. **2012**.

114. Lu, Y.; Shi, W.; Qin, J.; Lin, B. Fabrication and characterization of paper-based microfluidics prepared in nitrocellulose membrane by Wax printing. *Anal. Chem.* **2010**, *82*, 329–335, doi:10.1021/ac9020193.

115. Colozza, N.; Caratelli, V.; Moscone, D. Origami Paper-Based Electrochemical (Bio) Sensors : State of the Art and Perspective. **2021**, 1–29.

116. Spicar-Mihalic, P.; Toley, B.; Houghtaling, J.; Liang, T.; Yager, P.; Fu, E. CO2 laser cutting and ablative etching for the fabrication of paper-based devices. *J. Micromechanics Microengineering* **2013**, *23*, doi:10.1088/0960-1317/23/6/067003.

117. Ge, L.; Yan, J.; Song, X.; Yan, M.; Ge, S.; Yu, J. Three-dimensional paper-based electrochemiluminescence immunodevice for multiplexed measurement of biomarkers and point-of-care testing. *Biomaterials* **2012**, *33*, 1024–1031, doi:10.1016/j.biomaterials.2011.10.065.

118. Zhang, Y.; Zuo, P.; Ye, B.C. A low-cost and simple paper-based microfluidic device for simultaneous multiplex determination of different types of chemical contaminants in food. *Biosens. Bioelectron.* **2015**, *68*, 14–19, doi:10.1016/j.bios.2014.12.042.

119. Lopez-Ruiz, N.; Curto, V.F.; Erenas, M.M.; Benito-Lopez, F.; Diamond, D.; Palma, A.J.; Capitan-Vallvey, L.F. Smartphone-based simultaneous pH and nitrite colorimetric determination for paper microfluidic devices. *Anal. Chem.* **2014**, *86*, 9554–9562, doi:10.1021/ac5019205.

120. De Souza, F.R.; Alves, G.L.; Coltro, W.K.T. Capillary-driven toner-based microfluidic devices for clinical diagnostics with colorimetric detection. *Anal. Chem.* **2012**, *84*, 9002–9007, doi:10.1021/ac302506k.

121. Jang, H.; Park, J.H.; Oh, J.; Kim, K.; Kim, M.G. Advanced Colorimetric Paper Sensors Using Color Focusing Effect Based on Asymmetric Flow of Fluid. *ACS Sensors* **2019**, *4*, 1103–1108, doi:10.1021/acssensors.9b00390.

122. Yetisen, A.K.; Jiang, N.; Tamayol, A.; Ruiz-esparza, G.U.; Zhang, Y.S.; Medina-pando, S.; Gupta, A.; Wolffsohn, J.S. Lab on a Chip electrolyte analysis †‡. **2017**, 1137–1148, doi:10.1039/c6lc01450j.

123. Ratchathani, U.; Ratchathani, U.; Ratchathani, U. Use of a Smartphone as a Colorimetric Analyzer in Paper-based. **2018**, *34*, 75–81.

124. Hossain, S.M.Z.; Brennan, J.D. β -Galactosidase-Based Colorimetric Paper Sensor for Determination. **2011**, 8772–8778.

125. Kumar, S.; Pandey, C.M.; Hatamie, A.; Simchi, A.; Willander, M.; Malhotra, B.D. Nanomaterial-Modified Conducting Paper: Fabrication, Properties, and Emerging Biomedical Applications. *Glob. Challenges* **2019**, *3*, 1900041, doi:10.1002/gch2.201900041.

126. Bendicho, C.; Lavilla, I.; Pena-pereira, F.; Calle, I. De; Romero, V. Nanomaterial-Integrated Cellulose Platforms for Optical Sensing of Trace Metals and Anionic Species in the Environment. **2021**.

127. Chen, G.; Chen, W.; Yen, Y.; Wang, C.; Chang, H.; Chen, C. Detection of mercury (II) ions using colorimetric gold nanoparticles on paper-based analytical devices. **2014**.

128. Marques, A.C.; Martins, R.; Fortunato, E. Paper Micro fl uidics and Tailored Gold Nanoparticles for Nonenzymatic, Colorimetric Multiplex Biomarker Detectioń. **2021**, doi:10.1021/acsami.0c19089.

129. Valentini, P.; Galimberti, A.; Mezzasalma, V.; De Mattia, F.; Casiraghi, M.; Labra, M.; Pompa, P.P. DNA Barcoding Meets Nanotechnology: Development of a Universal Colorimetric Test for Food Authentication. *Angew. Chemie - Int. Ed.* **2017**, *56*, 8094–8098, doi:10.1002/anie.201702120.

130. Sun, J.; Xianyu, Y.; Jiang, X. Point-of-care biochemical assays using gold nanoparticle-implemented microfluidics. *Chem. Soc. Rev.* **2014**, *43*, 6239–6253, doi:10.1039/c4cs00125g.

131. Wilson, R. The use of gold nanoparticles in diagnostics and detection. *Chem. Soc. Rev.* **2008**, *37*, 2028–2045, doi:10.1039/b712179m.

132. Pedone, D.; Moglianetti, M.; De Luca, E.; Bardi, G.; Pompa, P.P. Platinum nanoparticles in nanobiomedicine. *Chem. Soc. Rev.* **2017**, *46*, 4951–4975, doi:10.1039/c7cs00152e.

133. Das, B.; Franco, J. Lou; Logan, N.; Balasubramanian, P.; Kim, M. Il; Cao, C. *Nanozymes in Point-of-Care Diagnosis: An Emerging Futuristic Approach for Biosensing*; Springer Singapore, 2021; Vol. 13; ISBN 4082002100717.

134. Jiang, D.; Ni, D.; Rosenkrans, Z.T.; Huang, P.; Yan, X.; Cai, W. Nanozyme: New horizons for responsive biomedical applications. *Chem. Soc. Rev.* **2019**, *48*, 3683–3704, doi:10.1039/c8cs00718g.

135. Lin, Y.; Ren, J.; Qu, X. Nano-gold as artificial enzymes: Hidden talents. *Adv. Mater.* **2014**, *26*, 4200–4217, doi:10.1002/adma.201400238.

136. Donati, P.; Moglianetti, M.; Veronesi, M.; Prato, M.; Tatulli, G.; Bandiera, T.; Pompa, P.P. Nanocatalyst/Nanoplasmon-Enabled Detection of Organic Mercury: A One-Minute Visual Test. *Angew. Chemie* **2019**, *131*, 10391–10395, doi:10.1002/ange.201905669.

137. Song, W.; Zhao, B.; Wang, C.; Ozaki, Y.; Lu, X. Functional nanomaterials with unique enzyme-like characteristics for sensing applications. *J. Mater. Chem. B* **2019**, *7*, 850–875, doi:10.1039/c8tb02878h.

138. Kim, J.; Campbell, A.S.; de Ávila, B.E.F.; Wang, J. Wearable biosensors for healthcare monitoring. *Nat. Biotechnol.* **2019**, *37*, 389–406, doi:10.1038/s41587-019-0045-y.

139. Vashist, S.K. Non-invasive glucose monitoring technology in diabetes management: A review. *Anal. Chim. Acta* **2012**, *750*, 16–27, doi:10.1016/j.aca.2012.03.043.

140. Khan, R.; Khurshid, Z.; Yahya Ibrahim Asiri, F. Advancing Point-of-Care (PoC) Testing Using Human Saliva as Liquid Biopsy. *Diagnostics* **2017**, *7*, 39, doi:10.3390/diagnostics7030039.

141. Pomili, T.; Donati, P.; Pompa, P.P. Paper-based multiplexed colorimetric device for the simultaneous detection of salivary biomarkers. *Biosensors* **2021**, *11*, 1–11, doi:10.3390/bios11110443.

142. Weverling-Rijnsburger, A.W.E.; Blauw, G.J.; Lagaay, A.M.; Knook, D.L.; Meinders, A.E.; Westendorp, R.G.J. Total cholesterol and risk of mortality in the oldest old. *Lancet* **1997**, *350*, 1119–1123, doi:10.1016/S0140-6736(97)04430-9.

143. Li, L.; Dutkiewicz, E.P.; Huang, Y.; Zhou, H.; Hsu, C. ScienceDirect Analytical methods for cholesterol quantification. **2018**, *7*, doi:10.1016/j.jfda.2018.09.001.

144. Plüddemann, A.; Thompson, M.; Price, C.P. Clinical Intelligence Point-of-care testing for the analysis of lipid panels : primary care diagnostic technology update. **2012**, 2011–2013, doi:10.3399/bjgp12X630241.British.

145. Singh, S.; Ramesh, V.; Oza, N.; Balamurali, P.D. Evaluation of serum and salivary lipid pro fi le : A correlative study. **2014**, *18*, 5–7, doi:10.4103/0973-029X.131881.

146. Yang, X.; Fu, T.; Kota, P.K.; Tjia, M.; Nguyen, C.M.; Chiao, J.C. Lactate sensors on flexible substrates. *Biosensors* **2016**, *6*, doi:10.3390/bios6030048.

147. Farrel, P.A.; Wilmor, J.H.; Coyl, E.F.; Billin, J.E.; Costil, D.L. Plasma lactate accumulation and distance running performance. *Med. Sci. Sports Exerc.* **1993**, *25*, 1091–1097, doi:10.1249/00005768-199310000-00002.

148. Calabria, D.; Caliceti, C.; Zangheri, M.; Mirasoli, M.; Simoni, P.; Roda, A. Smartphone–based enzymatic biosensor for oral fluid L-lactate detection in one minute using confined multilayer paper reflectometry. *Biosens. Bioelectron.* **2017**, *94*, 124–130, doi:10.1016/j.bios.2017.02.053.

149. Billat, V.L.; Sirvent, P.; Py, G.; Koralsztein, J.-P.; Mercier, J. The Concept of Maximal Lactate

Steady State. *Sport. Med.* **2003**, *33*, 407–426, doi:10.2165/00007256-200333060-00003.

150. Puangbanlang, C.; Sirivibulkovit, K.; Nacapricha, D.; Sameenoi, Y. A paper-based device for simultaneous determination of antioxidant activity and total phenolic content in food samples. *Talanta* **2019**, *198*, 542–549, doi:10.1016/j.talanta.2019.02.048.

151. Rossini, E.L.; Milani, M.I.; Carrilho, E.; Pezza, L.; Pezza, H.R. Simultaneous determination of renal function biomarkers in urine using a validated paper-based microfluidic analytical device. *Anal. Chim. Acta* **2018**, *997*, 16–23, doi:10.1016/j.aca.2017.10.018.

152. Maiorano, G.; Rizzello, L.; Malvindi, M.A.; Shankar, S.S.; Martiradonna, L.; Falqui, A.; Cingolani, R.; Pompa, P.P. Monodispersed and size-controlled multibranched gold nanoparticles with nanoscale tuning of surface morphology. *Nanoscale* **2011**, *3*, 2227–2232, doi:10.1039/c1nr10107b.

153. Williamson, S.; Munro, C.; Pickler, R.; Grap, M.J.; Elswick, R.K. Comparison of Biomarkers in Blood and Saliva in Healthy Adults. *Nurs. Res. Pract.* **2012**, *2012*, 1–4, doi:10.1155/2012/246178.

154. Ates, H.C.; Roberts, J.A.; Lipman, J.; Cass, A.E.G.; Urban, G.A.; Dincer, C. On-Site Therapeutic Drug Monitoring. *Trends Biotechnol.* **2020**, *38*, 1262–1277, doi:10.1016/j.tibtech.2020.03.001.

155. Sessink, P.J.M.; Bos, R.P. Drugs Hazardous to Healthcare Workers Evaluation of Methods for Monitoring Occupational Exposure to Cytostatic Drugs. **1999**, *20*, 347–359.

156. Marler-hausen, T.; Holt, C.; Headley, C.; Sessink, P. Use of a closed-system drug transfer device reduces contamination with doxorubicin during bolus injection. **2020**, *29*.

157. Ndaw, S.; Denis, F.; Marsan, P.; Almeida, A.; Robert, A. Biological monitoring of occupational exposure to 5-fluorouracil : Urinary ␣ -fluoro- ⍰ -alanine assay by high performance liquid chromatography tandem mass spectrometry in health care personnel ℭ. *J. Chromatogr. B* **2010**, *878*, 2630–2634, doi:10.1016/j.jchromb.2010.02.011.

158. Turci, R.; Sottani, C.; Spagnoli, G.; Minoia, C. B iological and environmental monitoring of hospital personnel exposed to antineoplastic agents : a review of analytical methods. **2003**, *789*, 169–209.

159. Carvalho, C.; Santos, R.; Cardoso, S.; Correia, S.; Oliveira, P.; Santos, M.; Moreira, P. Doxorubicin: The Good, the Bad and the Ugly Effect. *Curr. Med. Chem.* **2009**, *16*, 3267–3285, doi:10.2174/092986709788803312.

160. Cardinale, D.; Iacopo, F.; Cipolla, C.M. Cardiotoxicity of Anthracyclines. **2020**, *7*, 3–5, doi:10.3389/fcvm.2020.00026.

161. Chen, T.; Shen, H.M.; Deng, Z.Y.; Yang, Z.Z.; Zhao, R.L.; Wang, L.; Feng, Z.P.; Liu, C.; Li, W.H.; Liu, Z.J. A herbal formula, SYKT, reverses doxorubicin-induced myelosuppression and cardiotoxicity by inhibiting ROS-mediated apoptosis. *Mol. Med. Rep.* **2017**, *15*, 2057–2066, doi:10.3892/mmr.2017.6272.

162. Solimando, D.A.; Wilson, J.P. Demonstration of skin fluorescence following exposure to doxorubicin. *Cancer Nurs.* 1983, *6*, 313–315.

163. Álvarez-Cedrón, L.; Sayalero, M.L.; Lanao, J.M. High-performance liquid chromatographic validated assay of doxorubicin in rat plasma and tissues. *J. Chromatogr. B Biomed. Sci. Appl.* **1999**, *721*, 271–278, doi:10.1016/S0378-4347(98)00475-7.

164. Chemother, C.; Baurain, R.; Campeneere, D.D.; Trouet, A. Ancer Hemotheraw and Harmacology ©. **1979**, *14*, 11–14.

165. Yang, M.; Yan, Y.; Liu, E.; Hu, X.; Hao, H.; Fan, J. Polyethyleneimine-functionalized carbon dots as a fluorescent probe for doxorubicin hydrochloride by an inner filter effect. *Opt. Mater. (Amst).* **2021**, *112*, 110743, doi:10.1016/j.optmat.2020.110743.

166. El-Maghrabey, M.; Kishikawa, N.; Kamimura, S.; Ohyama, K.; Kuroda, N. Design of a dual functionalized chemiluminescence ultrasensitive probe for quinones based on their redox cycle. Application to the determination of doxorubicin in lyophilized powder and human serum. *Sensors Actuators, B Chem.* **2021**, *329*, 129226, doi:10.1016/j.snb.2020.129226.

167. Semreen, M.H.; Alniss, H.Y.; Mousa, M.K.; El-Awady, R.; Khan, F.; Al-Rub, K.A. Quantitative determination of doxorubicin in the exosomes of A549/MCF-7 cancer cells and human plasma using ultra performance liquid chromatography-tandem mass spectrometry. *Saudi Pharm. J.* **2018**, *26*, 1027–1034, doi:10.1016/j.jsps.2018.05.011.

168. Ricciarello, R.; Pichini, S.; Pacifici, R.; Altieri, I.; Pellegrini, M.; Fattorossi, A.; Zuccaro, P. Simultaneous determination of epirubicin, doxorubicin and their principal metabolites in human plasma by high-performance liquid chromatography and electrochemical detection. *J. Chromatogr. B Biomed. Appl.* **1998**, *707*, 219–225, doi:10.1016/S0378-4347(97)00610-5.

169. Alarfaj, N.A.; El-Tohamy, M.F. New functionalized polymeric sensor based nio/mgo nanocomposite for potentiometric determination of doxorubicin hydrochloride in commercial injections and human plasma. *Polymers (Basel).* **2020**, *12*, 1–18, doi:10.3390/polym12123066.

170. Bobin-dubigeon, C.; Amiand, M.; Percheron, C.; Audeval, C.; Rochard, S.; Leynia, P.; Bard, J. A New , Validated Wipe-Sampling Procedure Coupled to LC – MS Analysis for the Simultaneous Determination of 5-Fluorouracil , Doxorubicin and Cyclophosphamide in Surface Contamination. **2013**, 433–439.

171. Bukar, N.; Toulouse, J.L.; Pelletier, J.N.; Masson, J. Naked-eye nanobiosensor for therapeutic drug monitoring of methotrexate. **2015**, doi:10.1039/c5an00996k.

172. Peeling, R.W.; Mabey, D. Point-of-care tests for diagnosing infections in the developing world. *Eur. Soc. Clin. Infect. Dis.* **2010**, *16*, 1062–1069, doi:10.1111/j.1469-0691.2010.03279.x.

173. Teymourian, H.; Parrilla, M.; Sempionatto, J.R.; Montiel, N.F.; Barfidokht, A.; Van Echelpoel, R.; De Wael, K.; Wang, J. Wearable Electrochemical Sensors for the Monitoring and Screening of Drugs. *ACS Sensors* **2020**, *5*, 2679–2700, doi:10.1021/acssensors.0c01318.

174. Karukstis, K.K.; Thompson, E.H.Z.; Whiles, J.A.; Rosenfeld, R.J. Deciphering the fluorescence signature of daunomycin and doxorubicin. *Biophys. Chem.* **1998**, *73*, 249–263, doi:10.1016/S0301-4622(98)00150-1.

175. Motlagh, N.S.H.; Parvin, P.; Ghasemi, F.; Atyabi, F. Fluorescence properties of several chemotherapy drugs: doxorubicin, paclitaxel and bleomycin. *Biomed. Opt. Express* **2016**, *7*, 2400, doi:10.1364/boe.7.002400.

176. Nguyen, T.N.; Nguyen, T.T.; Nghiem, T.H.L.; Nguyen, D.T.; Tran, T.T.H.; Vu, D.; Nguyen, T.B.N.; Nguyen, T.M.H.; Nguyen, V.T.; Nguyen, M.H. Optical properties of doxorubicin hydrochloride load and release on silica nanoparticle platform. *Molecules* **2021**, *26*, doi:10.3390/molecules26133968.

177. Van Raalte, J.; Rice, C.; Moss, C.E. Visible-light system for detecting doxorubicin contamination on skin and surfaces. *Am. J. Hosp. Pharm.* **1990**, *47*, 1067–1074, doi:10.1093/ajhp/47.5.1067.

178. Pomili, T.; Gatto, F.; Pompa, P.P. A Lateral Flow Device for Point-of-Care Detection of Doxorubicin. *Biosensors* **2022**, *12*, doi:10.3390/bios12100896.

179. Hassani Moghadam, F.; Taher, M.A.; Karimi-Maleh, H. Doxorubicin anticancer drug monitoring by ds-dna-based electrochemical biosensor in clinical samples. *Micromachines* **2021**, *12*, doi:10.3390/mi12070808.

180. Javani, A.; Javadi-Zarnaghi, F.; Rasaee, M.J. Development of a colorimetric nucleic acid-based lateral flow assay with non-biotinylated capture DNA. *Appl. Biol. Chem.* **2017**, *60*, 637–645, doi:10.1007/s13765-017-0321-9.

181. Liu, J.; Mazumdar, D.; Lu, Y. A simple and sensitive “dipstick” test in serum based on lateral

flow separation of aptamer-linked nanostructures. *Angew. Chemie - Int. Ed.* **2006**, *45*, 7955–7959, doi:10.1002/anie.200603106.

182. Minagawa, H.; Onodera, K.; Fujita, H.; Sakamoto, T.; Akitomi, J.; Kaneko, N.; Shiratori, I.; Kuwahara, M.; Horii, K.; Waga, I. Selection, Characterization and Application of Artificial DNA Aptamer Containing Appended Bases with Sub-nanomolar Affinity for a Salivary Biomarker. *Sci. Rep.* **2017**, *7*, 1–9, doi:10.1038/srep42716.

183. Fang, Z.; Huang, J.; Lie, P.; Xiao, Z.; Ouyang, C.; Wu, Q.; Wu, Y.; Liu, G.; Zeng, L. Lateral flow nucleic acid biosensor for Cu2+ detection in aqueous solution with high sensitivity and selectivity. *Chem. Commun.* **2010**, *46*, 9043–9045, doi:10.1039/c0cc02782k.

184. Jauset-Rubio, M.; Svobodová, M.; Mairal, T.; McNeil, C.; Keegan, N.; Saeed, A.; Abbas, M.N.; El-Shahawi, M.S.; Bashammakh, A.S.; Alyoubi, A.O.; et al. Ultrasensitive, rapid and inexpensive detection of DNA using paper based lateral flow assay. *Sci. Rep.* **2016**, *6*, 1–10, doi:10.1038/srep37732.

185. Ying, N.; Ju, C.; Li, Z.; Liu, W.; Wan, J. Visual detection of nucleic acids based on lateral flow biosensor and hybridization chain reaction amplification. *Talanta* **2017**, *164*, 432–438, doi:10.1016/j.talanta.2016.10.098.

186. Nimse, S.B.; Song, K.; Sonawane, M.D.; Sayyed, D.R.; Kim, T. Immobilization techniques for microarray: Challenges and applications. *Sensors (Switzerland)* **2014**, *14*, 22208–22229, doi:10.3390/s141222208.

187. Singh, V.; Zharnikov, M.; Gulino, A.; Gupta, T. DNA immobilization, delivery and cleavage on solid supports. *J. Mater. Chem.* **2011**, *21*, 10602–10618, doi:10.1039/c0jm04359a.

188. Aktas, G.B.; Ribera, A.; Skouridou, V.; Masip, L. DNA immobilization and detection using DNA binding proteins. *Anal. Bioanal. Chem.* **2021**, *413*, 1929–1939, doi:10.1007/s00216-021-03162-5.

189. Sawant, P.D.; Watson, G.S.; Nicolau, D.; Myhra, S.; Nicolau, D. V. Hierarchy of DNA immobilization and hybridization on poly-L-lysine using an atomic force microscopy study. *J. Nanosci. Nanotechnol.* **2005**, *5*, 951–957, doi:10.1166/jnn.2005.125.

190. Xu, C.; Cai, H.; Xu, Q.; He, P.; Fang, Y. Characterization of single-stranded DNA on chitosan-modified electrode and its application to the sequence-specific DNA detection. *Anal. Bioanal. Chem.* **2001**, *369*, 428–432, doi:10.1007/s002160000673.

191. James Cleaves, H.; Crapster-Pregont, E.; Jonsson, C.M.; Jonsson, C.L.; Sverjensky, D.A.; Hazen, R.A. The adsorption of short single-stranded DNA oligomers to mineral surfaces. *Chemosphere* **2011**, *83*, 1560–1567, doi:10.1016/j.chemosphere.2011.01.023.

192. Sastry, C.S.P.; Lingeswara Rao, J.S.V.M. Determination of doxorubicin hydrochloride by visible spectrophotometry. *Talanta* **1996**, *43*, 1827–1835, doi:10.1016/0039-9140(96)01932-7.

193. Pradhan, N.; Rajkhowa, H.; Giri, H.; Shrestha, B. Simultaneous spectrophotometric estimation of moxifloxacin hydrochloride and doxorubicin hydrochloride. *Int. J. Pharm. Pharm. Sci.* **2015**, *7*, 21–26.

194. Jouyban, A.; Samadi, A.; Jouyban-Gharamaleki, V.; Khoubnasabjafari, M. A microscale spectrophotometric method for quantification of doxorubicin in exhaled breath condensate. *Anal. Methods* **2019**, *11*, 648–653, doi:10.1039/c8ay02286k.

195. Sikora, T.; Morawska, K.; Lisowski, W.; Rytel, P.; Dylong, A. Application of Optical Methods for Determination of Concentration of Doxorubicin in Blood and Plasma. **2022**, 1–11.

196. Kauffman, M.; Kauffman, M.; Zhu, H.; Jia, Z.; Li, Y. Fluorescence-Based Assays for Measuring Doxorubicin in Biological Systems. *React. Oxyg. Species* **2016**, *2*, 432–439, doi:10.20455/ros.2016.873.

197. Tavallali, H.; Jahanbekam, A. Flow injection spectrophotometric determination of doxorubicin hydrochloride in urine samples. *Int. J. PharmTech Res.* **2010**, *2*, 1943–1947.

198. Maliszewska, O.; Plenis, A.; Olędzka, I.; Kowalski, P.; Miękus, N.; Bień, E.; Krawczyk, M.A.; Adamkiewicz-Drożynska, E.; Bączek, T. Optimization of LC method for the quantification of doxorubicin in plasma and urine samples in view of pharmacokinetic, biomedical and drug monitoring therapy studies. *J. Pharm. Biomed. Anal.* **2018**, *158*, 376–385, doi:10.1016/j.jpba.2018.06.031.

199. Charbaji, A.; Heidari-Bafroui, H.; Anagnostopoulos, C.; Faghri, M. A new paper-based microfluidic device for improved detection of nitrate in water. *Sensors (Switzerland)* **2021**, *21*, 1–15, doi:10.3390/s21010102.

200. Uhrovčík, J. Strategy for determination of LOD and LOQ values - Some basic aspects. *Talanta* **2014**, *119*, 178–180, doi:10.1016/j.talanta.2013.10.061.

201. Sarigul, N.; Korkmaz, F.; Kurultak, İ. A New Artificial Urine Protocol to Better Imitate Human Urine. *Sci. Rep.* **2019**, *9*, 1–11, doi:10.1038/s41598-019-56693-4.

202. Khan, Z.A.; Tripathi, R.; Mishra, B. Methotrexate : a detailed review on drug delivery and clinical aspects. **2012**, 151–169.

203. Ertino, J.R.B.; Öker, E.G.; Orlick, R.G.; Anerjee, D.B. Resistance Mechanisms to Methotrexate in Tumors. **1996**, 223–226, doi:10.1634/theoncologist.1-4-223.

204. Tian, H.; Cronstein, B.N. Understanding the Mechanisms of Action of Methotrexate. **2007**, *65*, 168–173.

205. Micha, R.; Imamura, F.; Ballmoos, M.W. Von Systematic Review and Meta-Analysis of Methotrexate Use and Risk. *AJC* **2011**, *108*, 1362–1370, doi:10.1016/j.amjcard.2011.06.054.

206. Rajnics, P.; Kellner, V.S.; Kellner, A.; Karadi, E.; Kollar, B.; Egyed, M. The Hematologic Toxicity of Methotrexate in Patients with Autoimmune iMedPub Journals The Hematologic Toxicity of Methotrexate in Patients with Autoimmune Disorders Keywords : **2017**, doi:10.21767/2576-3903.100010.

207. Widemann, B.C.; Adamson, C. P ediatric O ncology Understanding and Managing Methotrexate Nephrotoxicity. **2006**, 694–703, doi:10.1634/theoncologist.11-6-694.

208. Villa, A.; Tremolet, K.; Martinez, B.; Petit, M.; Dascon, X.; Stanek, J.; Ducint, D.; Titier-Debeaupuis, K.; Verdun-Esquer, C.; Molimard, M.; et al. Urine biomonitoring of occupational exposure to methotrexate using a highly sensitive UHPLC-MS/MS method in MRM3 mode. *J. Chromatogr. B Anal. Technol. Biomed. Life Sci.* **2022**, *1209*, 1–8, doi:10.1016/j.jchromb.2022.123411.

209. Nussbaumer, S.; Geiser, L.; Sadeghipour, F.; Hochstrasser, D. Wipe sampling procedure coupled to LC – MS / MS analysis for the simultaneous determination of 10 cytotoxic drugs on different surfaces. **2012**, 2499–2509, doi:10.1007/s00216-011-5157-2.

210. Li, Y.D.; Li, Y.; Liang, N.S.; Yang, F.; Kuang, Z.P. A reversed-phase high performance liquid chromatography method for quantification of methotrexate in cancer patients serum. *J. Chromatogr. B Anal. Technol. Biomed. Life Sci.* **2015**, *1002*, 107–112, doi:10.1016/j.jchromb.2015.08.017.

211. Uchiyama, M.; Matsumoto, T.; Matsumoto, T.; Jimi, S.; Takamatsu, Y.; Tamura, K.; Hara, S. Simple and sensitive HPLC method for the fluorometric determination of methotrexate and its major metabolites in human plasma by post-column photochemical reaction. *Biomed. Chromatogr.* **2012**, *26*, 76–80, doi:10.1002/bmc.1628.

212. Mathias, P.I.; Connor, T.H.; B'Hymer, C. A review of high performance liquid chromatographic-mass spectrometric urinary methods for anticancer drug exposure of health care workers. *J. Chromatogr. B Anal. Technol. Biomed. Life Sci.* **2017**, *1060*, 316–324, doi:10.1016/j.jchromb.2017.06.028.

213. Castro-Puyana, M.; Lammers, I.; Buijs, J.; Gooijer, C.; Ariese, F. Quenched phosphorescence as alternative detection mode in the chiral separation of methotrexate by electrokinetic chromatography. *Anal. Bioanal. Chem.* **2011**, *400*, 2913–2919, doi:10.1007/s00216-011-

4991-6.

214. Karami, F.; Ranjbar, S.; Ghasemi, Y.; Negahdaripour, M. Analytical methodologies for determination of methotrexate and its metabolites in pharmaceutical , biological and environmental samples. *J. Pharm. Anal.* **2019**, *9*, 373–391, doi:10.1016/j.jpha.2019.06.001.

215. Gurira, R.C.; Bowers, L.D. Electrochemistry of methotrexate. Part I. Characteristics of reduction. *J. Electroanal. Chem.* **1983**, *146*, 109–122, doi:10.1016/S0022-0728(83)80115-6.

216. Chen, Z.; Qian, S.; Chen, X.; Lin, Y. Protein-templated gold nanoclusters as fluorescence probes for the detection of methotrexate. **2012**, 4356–4361, doi:10.1039/c2an35786k.

217. Yockell-Lelièvre, H.; Bukar, N.; Toulouse, J.L.; Pelletier, J.N.; Masson, J.F. Naked-eye nanobiosensor for therapeutic drug monitoring of methotrexate. *Analyst* **2016**, *141*, 697–703, doi:10.1039/c5an00996k.

218. Kim, D.S.; Kim, Y.T.; Hong, S.B.; Kim, J.; Heo, N.S.; Lee, M.; Lee, S.J.; Kim, B. Il; Kim, I.S.; Huh, Y.S.; et al. Development of Lateral Flow Assay Based on Size-Controlled Gold Nanoparticles for., doi:10.3390/s16122154.

219. Hwan, D.; Ki, S.; Kyoung, Y.; Woo, B.; Dong, S.; Kim, S.; Shin, Y.; Kim, M. Biosensors and Bioelectronics Short communication A dual gold nanoparticle conjugate-based lateral flow assay (LFA) method for the analysis of troponin I. *Biosens. Bioelectron.* **2010**, *25*, 1999–2002, doi:10.1016/j.bios.2010.01.019.

220. Lou, S.; Ye, J.; Li, K.; Wu, A. PAPER A gold nanoparticle-based immunochromatographic assay : The influence of nanoparticulate size. **2012**, 1174–1181, doi:10.1039/c2an15844b.

221. Khlebtsov, B.N.; Tumskiy, R.S.; Burov, A.M.; Pylaev, T.E.; Khlebtsov, N.G. Quantifying the Numbers of Gold Nanoparticles in the Test Zone of Lateral Flow Immunoassay Strips. **2019**, doi:10.1021/acsanm.9b00956.

222. Khlebtsov, B.N.; Bratashov, D.N.; Byzova, N.A.; Dzantiev, B.B.; Khlebtsov, N.G. SERS-based lateral flow immunoassay of troponin I by using gap- enhanced Raman tags. **2019**, *12*, 413–420.

223. Byzova, N.A.; Safenkova, I. V.; Slutskaya, E.S.; Zherdev, A. V.; Dzantiev, B.B. Less is More: A Comparison of Antibody-Gold Nanoparticle Conjugates of Different Ratios. *Bioconjug. Chem.* **2017**, *28*, 2737–2746, doi:10.1021/acs.bioconjchem.7b00489.

LIST OF ACRONYMS

AgNPs silver nanoparticles

AuNPs gold nanoparticles

AuNRs gold nanorods

Br^- bromide ions

CGM continuous in-vivo monitoring

ChOx cholesterol oxidase

Cl^- chloride ions

CO_2 carbon dioxide

DLS dynamic light scattering

DNA deoxyribonucleic acid

dsDNA double-strand DNA

FAD flavin adenine dinucleotide

GDH glucose dehydrogenase

GOx glucose oxidase

hDHFR human dihydrofolate reductase

H_2O_2 hydrogen peroxide

HPLC high-performance liquid chromatography

I^- Iodide ions

IgG immunoglobulin G

ISF interstitial fluids

LC liquid chromatography

LFA lateral-flow assay

LFD lateral flow device

LoD limit of detection

LOx lactate oxidase

LSPR localized surface plasmon resonance

MGNPs multibranched gold nanoparticles

MS mass spectrometry

MTX methotrexate

NALFAs nucleic acid-based lateral flow assays

NIR near-infrared

NPs nanoparticles

Nylon+ positively charged nylon membrane

OD optical density

µPADs microfluidic paper-based devices

PDMS polydimethylsiloxane

PDVF polyvinylidene fluoride

POC point-of-care

POCT point-of-care testing

PVC polyvinyl chloride

RNA ribonucleic acid

SiO$_2$ NPs silica nanoparticles

ssDNA single-strand DNA

TDM therapeutic drug monitoring

TEM transmission electron microscopy

t-line test line

UV ultraviolet

LIST OF FIGURES

CHAPTER 1

Figure 1. Central laboratory testing (A) is based on instrumental techniques which enable accurate and sensitive analyses but require trained personnel and a long turnaround time; POC devices (B) can be performed by the patient at home, without complicated instrumentation, and provide rapid test results.

Figure 2. Operation principle of a CO_2 laser cutting technique and flow of red ink inside the hydrophobic boundaries[15].

Figure 3. Photograph of the paper-based µPADs for the multiplexed detection of biomolecules[17].

Figure 4. Schematic illustration of the main components of an LF device.

Figure 5. Comparison of the two main types of LFAs

Figure 6. Schematic illustration of salt-mediated immobilization of nucleic acids onto nitrocellulose membrane[29].

Figure 7. Nanomaterials size.

Figure 8. Size and shape-associated colors of three different Au nanomaterials.

Figure 9. Plasmonic colorimetric detection strategies.

Figure 10. A) Schematic illustration of the aggregation-based mechanism for the detection of mercury; B) Photograph of the proposed µPADs tested with increasing Hg (II) concentrations [42].

Figure 11. Different glucose bioresources and related physiological concentrations[51].

Figure 12. Schematic illustration of the etching mechanism involved in the detection of glucose in urine[52].

Figure 13. Saliva compositions and properties[56].

Figure 14. Schematic illustration of salivary 17β-estradiol detection[59].

Figure 15. Images of the LFD developed for 5-fluorouracil detection tested without the drug (A) and with 50 ng/cm^2 (B)[62].

CHAPTER 2

Figure 16. Glucose sensing strategies: A) Electrochemical sensor; B) Continuous blood glucose monitoring in interstitial fluid; C) µPAD[72].

Figure 17. Scheme of the action mechanism of the glucose biosensor based on Au nanostars shape alteration; the insert picture shows the colorimetric response to different concentrations of glucose in diluted serum a) blank serum, b) Au nanostars in serum, c) 0 mmol/L glucose, d) 0.001 mmol/L glucose, e) 0.002 mmol/L glucose[86].

Figure 18. NPs-corona complex in biological systems[88].

Figure 19. Controlled growth of Ag nanoclusters using BSA and lysozyme[91].

Figure 20. A) Reaction mechanism of the plasmonic glucose sensor; B) the UV-vis spectra change of AuNRs in the oxidation etching process[38]

Figure 21. Proposed mechanism of glucose sensing.

Figure 22. Assay prototype for home-testing of salivary glucose.

Figure 23. Synthesis of 15 nm AuNPs following Turkevich's method[99].

Figure 24. 15 nm AuNPs characterization including A) UV-vis absorption spectrum; B) DLS measurement; C) TEM size distribution analysis; D) TEM micrograph.

Figure 25. 60 nm MGNPs characterization including A) UV-vis absorption spectrum; B) DLS measurement; C) TEM size distribution analysis; D) TEM micrograph.

Figure 26. Proposed mechanism of MGNPs reshaping in water solution.

Figure 27. A) LSPR evolution over time shift as a function of the pH; B) Stability of the MGNPs at pH 5.

Figure 28. LSPR evolution of the reshaping in presence of different halogens.

Figure 29. A) LSPR evolution over time of the reshaping process in presence of increasing H_20_2 concentrations; B) λ evolution over time of the reshaping process in presence of increasing H_20_2 concentrations in the range of interest; C) absorption spectra related to MGNPs before reshaping (T0) and after the reaction with increasing H_20_2 concentrations (reaction time: 90min).

Figure 30. Absorption spectra related to the MGNP reshaping process under the optimized conditions.

Figure 31. A) LSPR Red-shift related to the protein corona; B) MGNPs stability in saliva and in presence of GOx; C) MGNPs stability in acetate buffer and in presence of GOx; D) MGNPs stability in saliva after 1 hour of incubation with GOx.

Figure 32. A) LSPR λ_{max} evolution over time of MGNPs reshaping in water (blue curves) and saliva; MGNPs absorption spectra when the assay is performed in glucose-supplemented saliva B) and physiological saliva C); TEM micrograph of MGNPs after the assay with physiological saliva (ctrl) D)

and glucose supplemented saliva (sample) E); F) Statistical TEM analyses measuring tips and core dimensions of the ctrl and sample.

Figure 33. A) Mechanism involved in MGNPs transfer on a solid support; B) UV-vis spectra of the remaining MGNPs suspensions after their immobilization on different substrates.

Figure 34. A) Colorimetric assay applied on healthy saliva (Ctrl), saliva supplemented with 1.5 mg/dL (S1) and 3 mg/dL (S2) glucose; B) Validation of the device prototype on different saliva samples including the controls: in absence of GOx (Ctrl1), with denatured GOx (Ctrl2), and with GOx (Ctrl3), and three supplemented samples: S1 (+1.5 mg/dL), S2 (+3 mg/dL) and S3 (+5 mg/dL).

Figure 35. A) Reflectance spectra of the nylon membranes treated with native saliva (Ctrl) and supplemented saliva (S2) (picture in insert shows the colorimetric assay performed on the dipstick prototype); B) HR-SEM micrographs of ctrl (blue) and S2 (red).

Figure 36. Stability test of the home-testing device prototype over time (t= 0, 1,2,3, and 6 months).

Figure 37. A) Validation of the RGB-based readout obtained by testing six saliva samples normalized with glucose spikes to reach 2.5, 4, and 6 mg/dL (representative image of the color change in the insert) and calculating ΔRGB with a smartphone app after 15 minutes of the assay. The statistical significance was determined using a one-way ANOVA and Tukey’s multiple comparison test (****P < 0.0001); B) Results of the proposed assay performed on 20 donors compared with the commercially available glucose assay kit (green: healthy patients, orange: diabetic group).

Figure 38. Analytical plot for LOD calculation.

CHAPTER 3

Figure 39. Schematic illustration of a POCT system characterized by the rapid signal read-out (sample-to-answer property)[5].

Figure 40. i-STAT from Abbott.

Figure 41. A) Schematic illustration of the µPAD for the analysis of electrolytes in tear fluids; B) Sample collection and assay procedure; C) Schematization of the portable device; D) Capturing of the smartphone image; E) Interlayer groove used to place the µPAD; F) Smartphone application to measure the fluorescence[122].

Figure 42. A) Colorimetric µPAD for the detection of heavy metals based on organic probes[124]; B) Sensing strategy of Hg (II) detection based on AuNPs[127].

Figure 43. Schematic illustrations of the target biomarkers of the proposed µPAD.

Figure 44. A) TEM micrographs of the MGNPs involved in the multiplexed detection of glucose, cholesterol, and lactate before (blue) and after (red) the reshaping process; B) Schematic illustration of the mechanism involved in the reshaping; C) evolution spectra over time of the reshaping process.

Figure 45. Schematic illustration of the proposed µPAD for the simultaneous detection of glucose, cholesterol, and lactate in saliva and the detection strategy involving the target-induced reshaping of MGNPs.

Figure 46. Glucose-induced reshaping process.

Figure 47. A paper sheet after the CO_2 laser cutting treatment.

Figure 48. Evolution over time of the flow of saliva mixed with a red dye on the µPAD.

Figure 49. Optimization of pH used for enzyme solution in glucose assay.

Figure 50. Optimization of the buffer used for NaI solution in lactate assay.

Figure 51. Optimization of enzyme units for cholesterol assay.

Figure 52. Analytical performance of the device obtained by plotting ΔR values of the implemented saliva (red bars) with that of native saliva (blue bars). Points represent the analyses performed on 10 saliva samples.

Figure 53. Evolution over time of the ΔR of native saliva (black lines), saliva spiked with the first analyte threshold (red lines), saliva spiked with the second analyte threshold (blue lines). The color band represents the standard deviation of measures performed on 10 different samples.

Figure 54. Images of the devices treated with native saliva (A); lactate spiked saliva (B); glucose spiked saliva (C); cholesterol spiked saliva (D).

Figure 55. Images of the devices treated with native saliva (A); saliva implemented with glucose (B); saliva implemented with glucose and cholesterol (C); saliva implemented with glucose, cholesterol, and lactate (D).

Figure 56. Graphs showing ΔR values of controls (red graph), control + interferent (pink graph), saliva supplemented with glucose (A), lactate (B), and cholesterol (C) (blue graphs), supplemented saliva + interferent (light blue graphs). Error bars represent the uncertainty from three independent measurements.

Figure 57. A) Image of the device prototype with the µPAD embedded in the patterned PVC film and a sealing film; the device prototype treated with saliva supplemented with the tree analytes at the beginning (B) and the end of the test (C).

CHAPTER 4

Figure 58. Schematic explanation of how TMD works[154].

Figure 59. Doxorubicin's adverse effects[160].

Figure 60. A) Peak intensity in terms of concentration of doxorubicin and corresponding UV-vis spectra of the drug; B) fluorescent peak as a function of the drug concentration[175].

Figure 61. Schematic illustration of the LF device for the detection of doxorubicin contamination on surfaces and urine. The device is composed of a nylon+ membrane as the running pad and a blend of cotton and glass fibers as the absorbent pad, laminated on a backing card. In the test zone, there is a spot of dsDNA, used as the capture bioreceptor. The test sample is deposited on the lateral side of the running pad, and it flows through the membrane exploiting the capillary forces. If doxorubicin is present in the sample, it intercalated with the dsDNA, conferring an intense, naked-eye fluorescence to the test region upon irradiation by a UV lamp. In the case of a non-contaminated sample, no fluorescence is visualized.

Figure 62. Performance of the device when the dsDNA probe is immobilized on different running pads: nylon+ (A), nitrocellulose western blotting membrane (B), nitrocellulose membrane CN95 (C), and Whatman qualitative filter paper grade 1 (D).

Figure 63. Detection of doxorubicin using an LF device with a capture probe composed of chitosan and DNA (A), poly-L-lysine and DNA (B), and DNA alone (C). Devices on the left were treated with a sample containing doxorubicin, and the ones on the right with the solvent alone.

Figure 64. A) Comparison of the performance of two devices treated with a short dsDNA oligonucleotide with 3’overhangs (left) and DNA calf thymus (right); devices treated with a short dsDNA oligonucleotide with 3’overhangs (B) and DNA calf thymus (C) when decreasing concentrations of doxorubicin were tested (10, 5, 1, 0.5, 0 µM).

Figure 65. Evaluation of the drying time. The test was performed after drying the probe for 5 minutes (A), 10 minutes (B), 30 minutes (C), and 60 minutes (D).

Figure 66. Comparison of the performance of the device after immobilizing increasing probe concentrations: from left to right, 1, 20, 100, and 200 µM.

Figure 67. Performance of the device after including sample pads of cotton fibers (left) and glass fibers (right) in the design.

Figure 68. A) Device tested with a water solution of doxorubicin with two subsequent additions of water. B) Devices tested with doxorubicin diluted in BSA, triton, SDS, Tris buffer, and tween, with no further additions of solvents.

Figure 69. A) Performance of the device tested with decreasing doxorubicin amounts (reported in the upper part of the image); B) Dependence of the optical response on doxorubicin amounts (points represent the ΔG values of 9 independent experiments).

Figure 70. Interference study of urinary components on the detection of doxorubicin: no interferents (1), sodium and magnesium sulfates (2), sodium and potassium chlorides (3), ammonia (4), sodium phosphate and phosphoric acid (5), sodium hydroxide (6), sodium citrate (7), urea and uric acid (8), creatinine (9), and hippuric acid (10).

Figure 71. Performance of the device with real urine sample after sample dilution: no dilution (1), 1:1 (2), 1:2 (3), 1:5 (4), 1:10 (5), 1:25 (6), 1:50 (7).

Figure 72. Analytical performance of the LF device with real urine samples spiked with decreasing doxorubicin amounts (reported in the upper part of the photograph).

CHAPTER 5

Figure 73. A) Comparison of the chemical structure of MTX and Folic Acid; B) Action mechanism of MTX.

Figure 74. MTX detection mechanism based con BSA-Au nanoclusters[216]

Figure 75. The naked-eye nanobiosensor for MTX detection[217].

Figure 76. Schematic illustration of the proposed LF device for MTX detection.

Figure 77. 35 nm AuNPs characterization including A) UV-vis absorption spectrum, B) DLS measurement, C) TEM size distribution analysis D) TEM micrograph.

Figure 78. A) LFD assembled with the conjugated pad prepared in ethanol; B) performance of the LFD in A) treated with water (control solution); C) LFD assembled with the conjugated pad prepared in water; B) performance of the LFD in C) treated with water (control solution).

Figure 79. A) Comparison of the LFA performance with water (ctrl) and a 250 µM solution of MTX (MTX), when 100 and 75 µM folic acid were used for the preparation of the conjugate; B) performance of the assay with different conjugate solution concentrations (reported in the upper part of the image).

Figure 80. Comparison of the performance of the LFA with non-buffered conjugate pads (A) and pads treated with sucrose, BSA, and Tween in borate buffer (B). MTX concentrations tested are reported in the upper part of the images (100-50-0 µM).

Figure 81. Comparison of the performance of the LFDs realized with the capture probe solved in water (A) and PBS (B).

Figure 82. Comparison of the performance of the devices treated with different concentrations of the capture probe (reported in the upper part of the image).

Figure 83. Devices tested with water (ctrl) and 100 µM solution of MTX with (A) and without (B) the blocking of the conjugate with BSA.

Figure 84. Proposed LFDs treated with decreasing MTX concentrations (reported in the upper part of the image).

LIST OF TABLES

CHAPTER 4

Table 1. Comparison of UV-vis instrumental techniques and my POCT for the detection of doxorubicin.

PHD PORTFOLIO

Oral communications:

- Pomili, T.; Donati, P.; Pompa, P.P.; “Paper-based multiplexing colorimetric device for the simultaneous detection of salivary biomarkers” Merck Young Chemists’ Symposium 2021, Rimini, November 22-24, 2021 (oral contribution)

- Pomili, T.; Donati, P.; Pompa, P.P.; “Paper-based multiplexing colorimetric device for the simultaneous detection of salivary biomarkers” 3NANO-2022, Nano Science/Technology/Biotechnology, Roma September 20-23, 2022 (oral contribution)

Scientific Publications:

- Paolo Donati†, Tania Pomili†, Luca Boselli* and Pier P. Pompa*, Colorimetric Nanoplasmonics to Spot Hyperglycemia From Saliva. *Front. Bioeng. Biotechnol. 8:601216,* **2020**, doi: 10.3389/fbioe.2020.601216

- Boselli, L.; Pomili, T.; Donati, P.; Pompa, P.P., Nanosensors for Visual Detection of Glucose in Biofluids: Are We Ready for Instrument-Free Home-Testing? *Materials* **2021***,* 14, 1978, https://doi.org/10.3390/ma14081978

- Pomili T, Donati P, Pompa PP, Paper-Based Multiplexed Colorimetric Device for the Simultaneous Detection of Salivary Biomarkers. *Biosensors (Basel). 10;11(11):443.* **2021**, doi: 10.3390/bios11110443

- Pomili T; Gatto, F.; Pompa, P.P. A Lateral Flow Device for Point-of-Care Detection of Doxorubicin. Biosensors **2022**, 12, 896. https://doi.org/10.3390/bios12100896

- Mastronardi, V., Kim, J., Veronesi, M., Pomili, T., Berti, F., Udayan, G., ... & Moglianetti, M., Green chemistry and first-principles theory enhance catalysis: synthesis and 6-fold catalytic activity increase of sub-5 nm Pd and Pt@ Pd nanocubes. *Nanoscale, 14(28), 10155-10168.* **2022**. doi: 10.1039/D2NR02278H

Manuscript under preparation:

- Pomili, T., Mastronardi, V., Pompa, P.P. An innovative lateral flow device for methotrexate detection

ACKNOWLEDGEMENTS

The work in IIT has given me the opportunity to collaborate with many incredible people who constantly help and encouraged me during these years. It has been a great fortune to meet such special people who gave me the opportunity to grow both as a scientist and as woman.

I would like to sincerely thank my tutor, Dr Pier Paolo Pompa, for giving me the opportunity to work in his research group and for guiding me in this impervious but rewarding road to the PhD. Thank you for believing in my work and for your support.

I would like to extend my special thanks to my Unige tutor, Prof. Annalisa Relini for her endless support and feedback, her kindness and constant availability to answer all my needs.

I am thankful to Prof. Barbara Roda (Alma Mater Studiorum, Università di Bologna) and Prof. Piera Di Martino (Università degli Studi di Chieti) who invested their valuable time and effort in regarding my thesis. I really appreciate your comments and advice.

I owe a deep sense of gratitude to the coordinator of my doctoral course, Prof. Renata Riva for her great willingness and her management skills over these years.

I would also like to thank all my colleagues for their mental support, friendship and the continuous brainstorming which help me finding solutions and facing every challenge in the best possible way.

I finally thank my family and Sergio because you are the reason for my own existence. You always believe in me more than I do myself. I don’t have enough words to express my deep sense of gratitude. Thank you for everything.

I once again thank each and every one of you, from the bottom of my heart. Wherever I go, I will take you with me.

Tania Pomili